ADVANCED TECHNIQUES FOR RESERVOIR ENGINEERING AND SIMULATION

by

Raul Velasco Guachalla

A dissertation submitted to the faculty of
The University of Utah
in partial fulfillment of the requirements for the degree of

Doctor of Philosophy

Department of Chemical Engineering

The University of Utah

May 2016

The University of Utah Graduate School

STATEMENT OF THESIS APPROVAL

The thesis of **Raul Velasco Guachalla**

has been approved by the following supervisory committee members:

Milind Deo	, Chair	**10/26/2015** Date Approved
John David McLennan	, Member	**10/26/2015**
Philip J. Smith	, Member	**11/23/2015**
Anil Vasudeo Virkar	, Member	**10/26/2015** Date Approved
Rasoul B. Sorkhabi	, Member	**10/26/2015** Date Approved

and by **Milind Deo**, Chair/Dean of

the Department/College/School of **Chemical Engineering**

and by David B. Kieda, Dean of The Graduate School.

ABSTRACT

The outstanding surge in hydrocarbon production from unconventional reservoirs is unprecedented. Profitable oil prices and new technologies have untapped massive oil and gas resources in recent years. However, the correct exploitation of these resources has been dampened by the lack of understanding of these systems. Research efforts to understand and properly assess unconventional resources have exploded in the literature. In this research work, a series of advancements in reservoir production analysis, simulation modeling, and simulation development are made.

A semi-analytical method based on conventional material balance was developed to approximate reservoir pressure distributions and permeability. One of the strengths of this method is that it only requires limited information to be viable. Reservoirs with dry gas and/or high gas oil ratios are handled with an additional average pressure correction factor that takes gas compressibility into account. Hence, this method can be used for any type of fluid and fluid flow as long as the correct material balance formulation and surrogate curves are employed. Verification of the method is made through comparison with synthetic data and a field case study.

Furthermore, a standardized simplification workflow for hydraulically stimulated reservoirs was introduced. The aim of this workflow is to guide the engineer when developing a simplified reservoir simulation model with multiple wells and fractures. Simplified models have been around for a long time in the literature, however, their

applicability to field-scale projects is very limited. Models that result from the application of this workflow are shown to retain the low simulation run-times characteristic of popular single-fracture models. In addition, fluid rate results from the proposed workflow models are in good agreement with results from full-scale simulation models. This is not the case for the single-fracture model which loses accuracy as the complexity of the project grows.

Lastly, a new discrete fracture model formulation is implemented in a control-volume finite element simulator. This new fracture model provides fractures with their own control volumes and gives them freedom to be placed anywhere in the matrix domain. Verification of this implementation is made through comparison with analytical expressions and other well-established simulators.

To my family.

TABLE OF CONTENTS

LIST OF TABLES

LIST OF FIGURES

NOMENCLATURE

Symbol		
α	Diffusivity	$foot^2/sec$
β_c	Transmissibility Conversion Factor	-
Φ	Phase Potential	psi
ϕ	Porosity	-
ΔP	Pressure Difference	psi
Δt	Time Difference	day
Δx	Length Difference	foot
μ_g	Gas Viscosity	cp
μ_o	Oil Viscosity	cp
μ_w	Water Viscosity	cp
μ_t	Total Viscosity	cp
Ω	Domain	-
A	Flow Area	$foot^2$
B_g	Gas Formation Volume Factor	RB/SCF
BHP	Bottom Hole Pressure	psi
B_o	Oil Formation Volume Factor	RB/STB
B_w	Water Formation Volume Factor	RB/STB
C_f	Formation Compressibility	1/psi

c_g	Gas Compressibility	1/psi
c_o	Oil Compressibility	1/psi
c_r	Rock Compressibility	1/psi
c_t	Total Compressibility	1/psi
c_w	Water Compressibility	1/psi
FBHP	Flowing Bottom Hole Pressure	psi
C_{fdf}	Dimensionless Fracture Conductivity	-
GOR	Gas Oil Ratio	SCF/STB
GOIP	Gas Originally In-Place	MMSCF
Gp	Cumulative Gas Produced	SCF
h	Formation Thickness	foot
k	Absolute Permeability	mD
k	Multiplying Factor	-
k_f	Fracture Permeability	mD
k_m	Reservoir Absolute Permeability	mD
K_{rg}	Gas Relative Permeability	-
K_{ro}	Oil Relative Permeability	-
k_{rog}	Oil Relative Permeability in Gas-Oil System	-
k_{row}	Oil Relative Permeability in Water-Oil System	-
k_{rw}	Water Relative Permeability	-
k_x	Reservoir Absolute Permeability in the X-direction	mD
k_{xy}	Matrix Horizontal Permeability	mD
k_y	Matrix Permeability in the Y-direction	mD
k_z	Matrix Permeability in the Z-direction	mD

L	Reservoir Extent	ft
l_x, l_y, l_z	Spacings of Fractures Planes	-
N	Number of Fracture Normal Sets	-
Np	Cumulative Oil Produced	STB
n_f	Number of fractures	-
n_w	Number of wells	-
OOIP	Oil Originally In-Place	MSTB
P	Pressure	psi
p	Phase	-
P_b	Bubble Point Pressure	psi
P_{bp}	Bubble Point Pressure	psi
P_f	Pressure at Fracture	psi
P_i	Initial Reservoir Pressure	psi
$\overline{P}$	Average Reservoir Pressure	psi
P_{wf}	Flowing Bottom Hole pressure	psi
q_g	Gas Rate	SCF/day
q_o	Oil Rate	STB/day
q_w	Water Rate	STB/day
r_e	Distance of Reservoir External Boundary	foot
R_p	Produced Gas Oil Ratio	SCF/STB
R_{pc}	Cumulative Gas Oil ratio	SCF/STB
R_s	Solution Gas Oil Ratio	SCF/STB
R_{sb}	Gas Oil Ratio at Bubble Point Pressure	SCF/STB
R_{si}	Initial Solution Gas Ratio	SCF/STB

r_w	Wellbore Radius	foot
S	Symmetric Factor	-
S^*	Effective Saturation	-
S_g	Gas Saturation	-
S_{gc}	Critical Gas Saturation	-
S_{org}	Residual Oil Saturation in Gas-Oil System	-
S_{orw}	Residual Oil Saturation in Water-Oil System	-
S_w	Water Saturation	-
S_{wc}	Irreducible Water Saturation	-
S_{wc}	Connate Water Saturation	-
t	Time	day
T	Reservoir Temperature	^OF
T	Transmissibility	STB/day-psi
V	Volume	$foot^3$
w	Width	foot
We	Cumulative Water Injected	STB
Wp	Cumulative Water Produced	STB
X	Reservoir Dimension in X-direction	foot
X_f	Fracture Half-length	foot
Y	Reservoir Dimension in Y-direction	foot
Ymodel,i	Modeled Value	Unit of Output
Yobs,i	Observed Data	Unit of Output
Yobs,max	The Maximum Value of Observed data	Unit of Output
Yobs,min	The Minimum Value of Observed data	Unit of Output

Subscripts

b	Bubble point
bp	Bubble point
CD	Conductivity
cv	Control Volume
e	Number of elements
f	Formation, fracture
frac	Fracture
g	Gas
i	Initial
j	Number count
l	Fluid phase
m	Matrix
max	Maximum
min	Minimum
o	Oil
obs	Observed
r	Rock
R	Reservoir
t	Total
w	Water, well
x	X direction
y	Y direction

z	Z direction

Abbreviations

BHP	Bottom Hole Pressure
FBHP	Flowing Bottom Hole Pressure
GOR	Gas Oil Ratio
GOIP	Gas Originally In-Place
OOIP	Oil Originally In-Place
LGR	Local Grid Refinement
MB	Material Balance
MBPP	Material Balance Pressure Profiles
NRMSE	Normalized Root Mean Square Error
NTG	Net to Gross Ratio
PVT	Pressure Volume Temperature
IMPES	Implicit Pressure Explicit Saturation
FEM	Finite Element Method
DFM	Discrete Fracture Model
RMSE	Root Mean Square Error

ACKNOWLEDGEMENTS

I would like to thank my advisor, Dr. Milind Deo, for his incredible support, guidance, and encouragement during my graduate program at the Chemical Engineering Department. I am very grateful to have had the chance to grow intellectually and personally under his wing. I am also thankful for the advice and support from the members of my supervisory committee: Drs. John McLennan, Anil Virkar, Philip Smith, and Rasoul Sorkhabi. I thank all the faculty and staff at the Chemical Engineering Department for sharing their knowledge during classes and being resourceful whenever I needed help. I am grateful to the Energy and Geosceince Institute for honoring me with a fellowship and many other awards and programs that supported me financially. I thank all my colleagues and classmates including Palash, Mustafa, Manas, Jing, Hyukmin, and Justin for making this a welcoming and great workplace. I am fortunate to have great friends outside of my work circle that made Salt Lake City truly a special place, in particular, Yulia for her support during the writing of this work. Finally, I thank my parents, Vania and Raul for their encouragement, unconditional support, and motivation, and my siblings Ximena and Ricardo for always being there for me.

CHAPTER 1

INTRODUCTION

1.1 Unconventional Hydrocarbon Production

North American unconventional oil and gas resources have proven to be an important energy asset. So much so that the United States is projected to become the single largest oil producer in the world due to unprecedented development from unconventional reservoirs.[1]

The U.S. Energy Information Administration (EIA) has noted that the definition of "unconventional" oil and gas resources is nebulous and depends on varying technologies and economies. In other words, conventional resources are the hydrocarbon fluids that are easy and cheap to extract and exploit, whereas unconventional resources consist of a large and wider variety of sources that includes oil sands, extra heavy oil, gas to liquids, and other liquids that require extra technology to produce. By this definition, as oil prices rise and technological advances are made, unconventional resources can migrate into the conventional category. In the following sections, the term "unconventional" will refer to low permeability formations in the range of micro- to nanodarcies, also known as tight formations. Some of the most important unconventional reservoirs are the Bakken and the Eagle Ford shown in **Figure 1.1**.

Since hydrocarbon flow can be very low in tight and ultra-tight formations, advanced

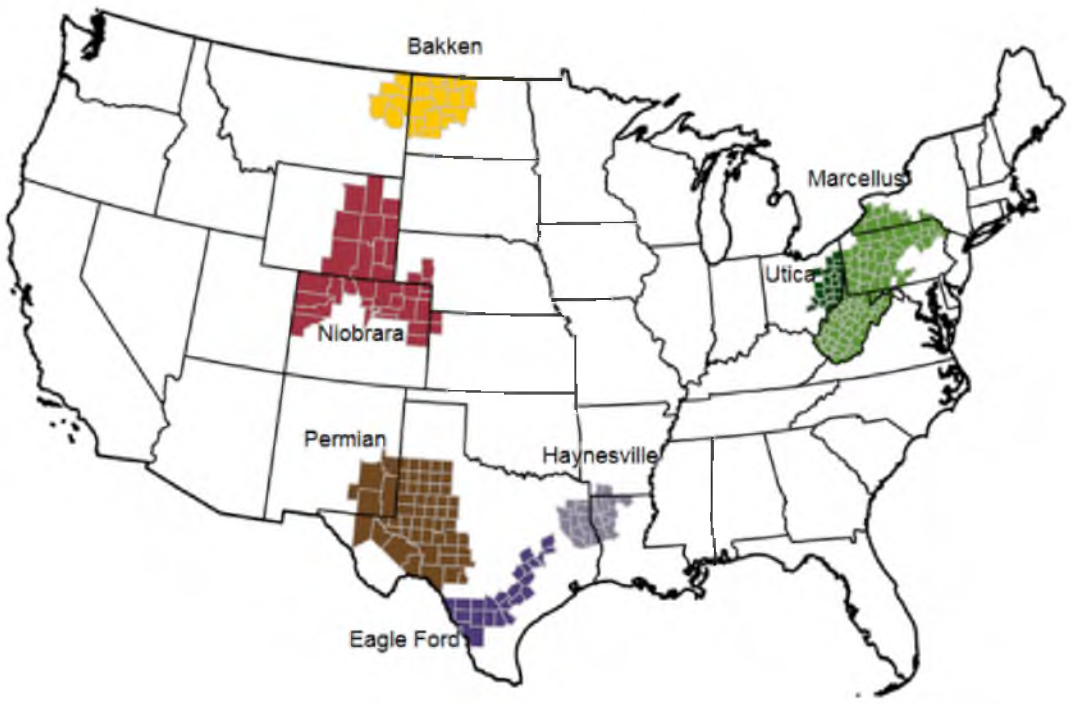

Figure 1.1 Map of U.S. most prominent unconventional plays (Source: EIA)

technologies are essential for economic exploitation, such as horizontal drilling and hydraulic fracturing. Even though these technologies add an extra price tag to oil companies, increasing oil prices made it profitable for plays like the Monterey/Santos in southern California, the Bakken and the Eagle Ford to be recently developed as reported by the EIA in July 2011.[2]

Oil and gas production from unconventional reservoirs in the United States is indisputably the main driver for American hydrocarbon production surge. Oil production from tight formations more than tripled in three years, increasing from about 250 Million Stock Tank Barrels (MSTB) per day at the beginning of 2009 to nearly 900 MSTB per day by 2011. About 84 percent of all tight oil production in November 2011 came from the Bakken formation in North Dakota and Montana, and the Eagle Ford shale in South Texas.

All seven regions: Eagle Ford, Bakken, Niobrara, Permian, Haynesville, Utica, and the Marcellus accounted for 95% of domestic oil production growth and all of domestic natural gas production growth from 2011 to 2013.[3] **Figure 1.2** shows the increase of oil and gas production from the most important shale plays in the United States.

Despite current crude oil price decline resulting in changes to oil production, rates are is still expected to rise for the next 30 years.[3] Hence, unconventional reservoirs are proving to be a very important energy asset for the future.

1.2 Research Motivation

Even though hydrocarbon production from shale plays has been critical to overall North American hydrocarbon production, ultimate recoveries remain very low. In addition, these resources cannot be properly assessed due to limited information about the reservoir and specifically the lack of knowledge of key parameters such as permeability. Sometimes, this

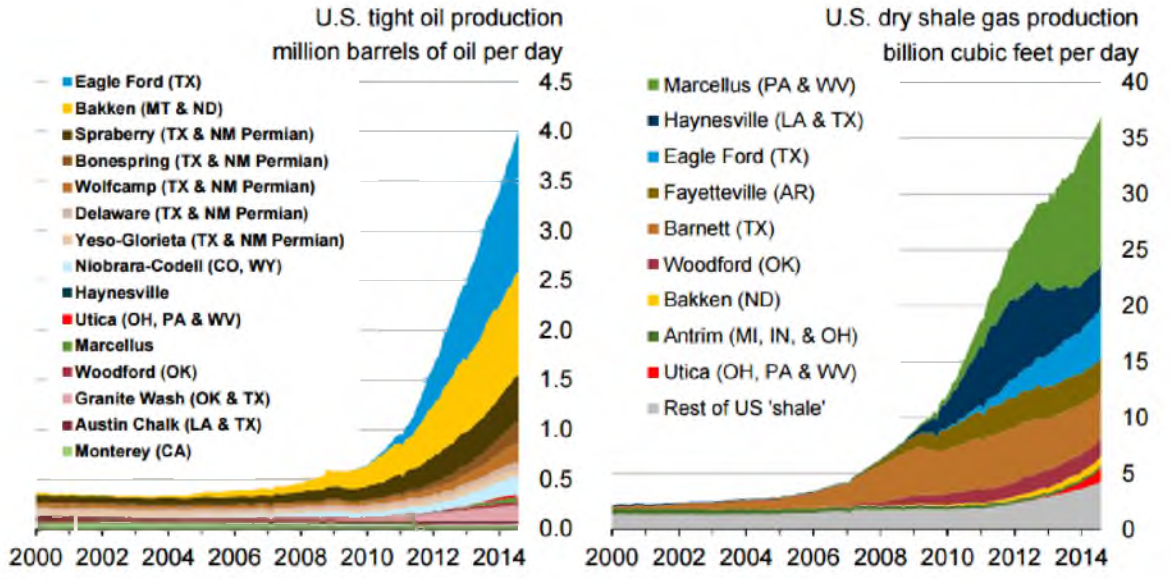

Figure 1.2 U.S. tight oil (left) and dry shale gas (right) production (Source: EIA)

information can be very expensive or impractical to obtain in these tight formations. This is why developing cheap and fast analytical tools to quickly assess a reservoir's hydrocarbon potential is important.

The widespread use of computer simulation to characterize and predict hydrocarbon recovery has become standard in the industry. However, computer simulation is still handicapped by limitations of computer power that may result in weeks and even months of simulation run time. This is why model simplifications of highly complex systems are sometimes mandatory at the cost of accuracy. Unfortunately, a well-structured and thorough simulation simplification workflow does not exist.

Another important factor in reservoir simulation is the representation of hydraulic and natural fractures. Historically, there have been many attempts to represent fluid flow through fractures accurately without sacrificing computational time. The Discrete Fracture Network (DFN) technique is one of the most widely used methods used for representing fractures in simulation. However, like all other methods, DFN has some disadvantages that need to be accounted for.

This research work develops semi-analytical techniques to quickly determine reservoirs' potential without the necessity of expensive well pressure testing or well logging techniques. Another aim of this research work is to aid reservoir engineers history-match and predict hydrocarbon production by using simplified yet accurate models. Lastly, a modification of the DFN is suggested to better represent fluid flow through hydraulic and natural fractures

1.3 Objectives

In view of the aforementioned research topics and motivation, the following research objectives are presented:

- Develop an analytical technique to help quickly and easily identify essential reservoir and fluid properties.
    - This technique should be able to handle distinct flow patterns.
    - Different fluids such as oil, water, and gas should be incorporated into this method.
    - Provide potential reservoir characterization analytics.
- Present a comprehensive reservoir simulation workflow that simplifies a simulation model without sacrificing accuracy.
    - Show that some of the current widely used simplified models do not accurately represent reality.
    - Are there any physical phenomena that could be ignored during reservoir simulation?
    - Develop rules and methods to determine whether reservoir model simplification is achievable.
- Modify current Discrete Fracture Network (DFN) implementation in Control Volume Finite Element Method (CVFM) simulators in order to better represent fluid flow in fractures.
    - Add fracture control volumes to a current DFN implementation.
    - Keep or improve current DFN meshing techniques to avoid troublesome explicit fracture meshing procedures.

The stated research objectives are addressed in the following chapters. Background information is first presented and proposed methods and procedures are explained in detail. Application of such methods are shown in the form of examples. These examples use reservoir and production information from simulation, field case studies or referenced work. Finally, validation and/or derivation of the proposed methods are presented in corresponding chapters.

Discussion and conclusions highlight the suggested methods' strengths and describe weaknesses. Additionally, important observations and possible improvements are made in respect to the objectives of this research work.

CHAPTER 2

MATERIAL BALANCE APPLIED TO TIGHT FORMATIONS

The black oil material balance is a simple method used to estimate original hydrocarbon in place in conventional reservoirs. It has served as a basic fast tool used to assess the production potential of a reservoir and as a way to either support or question numerical simulation results. Because typical application of material balance principle is in conventional boundary-dominated reservoirs, low and ultra-low permeability reservoirs (which have seen significant activity in the last few years) have not benefited from the cheap analytical power offered by this method. Hence, a new material balance formulation is required for analyzing these systems.

In this study, the conventional material balance is used in a semi-analytical method to construct transient-flow pressure profiles and estimate important reservoir parameters such as permeability. Since the conventional material balance method only requires pressure-volume-temperature data (PVT) and production information, it serves as an essential tool for systems where information is limited. This method is used with a high degree of accuracy for single-phase flow systems and gives reasonable results for two and three-phase systems. Validation is made through comparison with output from numerical simulation. Examples of oil, dry gas, and a field data case are discussed after establishing the method steps.

2.1 Background

Production of fluids from tight formations (shales) has completely changed the energy equation for the United States. Liquid production from the Bakken (North Dakota), Eagle Ford (Texas), and plays in the Permian Basin (Texas) accounted for over a third of the total U.S. oil output in 2014. The development has been very rapid, and the recoveries – particularly of liquids is low. It is recognized that the matrix permeability is extremely important in initial rates and in ultimate oil recovery. Obtaining good diagnostic information about how the recovery process is unfolding is critical to the success of the production method. In this section, a semi-analytical conventional material balance method is developed for application in tight formations often referred to as shales.

Material balance is one of the oldest methods developed to assess the hydrocarbon potential of a reservoir. This formulation was developed by Schilthuis (1936)[4] and has since been one of the main analysis tools for engineers, especially with the introduction of the straight line equation.[5] Although this is arguably the era of the numerical simulation, material balance remains an accurate and effective way of determining a reservoir's potential early into production.[6]

Important work to extend the conventional material balance formulation and apply it to unconventional reservoirs has been done in recent years. In 1994, Walsh et al.[7] introduced a general material balance equation that accounts for condensates and it is only recently that commercial numerical simulators are incorporating this concept. A material balance model was presented by Penuela et al. (2001)[8] to address naturally fractured reservoirs using a dual-system approach for initially under-saturated reservoirs. Under the same concept, Niz et al. (2004)[9] extended this approach for reservoirs with an initial gas

cap. Finally, Sandoval et al. (2009)[10] included condensates into their framework by incorporating a volatilized oil component in gas. There are other important advancements in the material balance theory that include the dynamic material balance and 'flowing' oil and gas material balance among others.[11-15]

Even though significant work has been put into expanding the material balance formulation to unconventional reservoirs, conventional material balance cannot be used for transient systems. This is because material balance is a zero-dimensional approach which assumes that the reservoir behaves like a single tank where all properties are exactly the same throughout the system. This is generally true for homogeneous formations with high permeabilities (typically conventional reservoirs). However, pressure propagation in tight reservoirs is very slow; taking months and even years before the pressure front propagating from the well reaches reservoir boundaries. This means that tight reservoirs remain in the transient flow stage for most of their productive lives[15] making the material balance technique inapplicable.

A novel technique is proposed to help determine a reservoir's potential by using conventional material balance and surrogate pressure profiles. This semi-analytical method fundamentally relies on the material balance formulation (assuming the reservoir behaves like a tank) and combines it with surrogate pressure profiles to obtain pressure behavior at any time during a well's transient-flow life. This is accomplished in three main steps:

1. Construct an average pressure profile for the system by using conventional material balance.
2. Determine a pressure profile based on the average pressure curve.
3. Compare pressure profiles to equations from the literature and back-calculate

important reservoir properties.

Pressure profiles for radial single-phase transient flow systems are represented by the exponential integral[16] while linear single-phase flow systems are described analytically by the error function[17]. These expressions are solutions to differential equations coupled with Darcy's law and are broadly used in well testing techniques[18]. Two and three-phase transient flow systems are typically solved by numerical simulation. In this work, equations such as the error function are used to calculate reservoir parameters when compared to material balance pressure profiles. It is important to highlight that the application of this method is not limited by the type of fluid flow (radial or linear) as long as an appropriate pressure equation is used. Also, dry gas material balance can be applied after a modification is introduced into the method to account for compressibility.

Since this method is based on the material balance formulation, it shares the same assumptions. There are also other assumptions that depend on the reservoir geometry and rock/fracture properties as described in the upcoming sections. Numerical simulations as well as a real field case were used to test and validate this semi-analytical method.

2.2 General Procedure

Before the method is introduced, an important variable which makes this concept different from the conventional material balance is addressed. All material balance expressions contain a parameter known as "Oil Originally In Place" (OOIP) or "Gas Originally In Place" (GOIP). This parameter is typically the unknown during the application of conventional material balance. OOIP may also be calculated volumetrically if the reservoir's geometry is known. In the case of transient-flow, however, the extent of

the reservoir cannot be determined due to the infinite-reservoir behavior which is characteristic of this type of flow. Hence, rather than calculating OOIP volumetrically, the extent of the reservoir is simply treated as a variable. This variable is referred to as "Distance" in this work and is defined as a vector normal to the well or hydraulic fracture as shown in **Figure 2.1**.

The detailed method theory is provided in Appendix A. The general application of the method steps are as follows:

1. Set up the material balance equation such that "distance" is the dependent variable. In other words:

$$d = f(A_r, \bar{P}, Sw, Cw, Cf, Np, Gp, Wp, \dots) \qquad 2.1$$

   All the parameters are described in the Nomenclature Section.

2. Plot $\bar{P}$ versus distance using equation 2.1 and a production data point at time "*t*".
3. Extrapolate the average pressure curve ($\bar{P}$ vs distance) to the known bottom hole pressure at $\bar{P}$ *(0)*=*Pwf*. The use of a surrogate curve that matches the average pressure curve and interpolates to *Pwf* is highly recommended and used in future examples.
4. Determine a pressure profile expression from the average pressure curve by using a volumetric average pressure relation.
5. Back-calculate permeability using surrogate curve equation.
6. Determine another pressure profile and permeability by following the steps above using a different production data point. This effectively means that the time variable will be equal to effective production time.

This method can be used for any kind of fluid flow and fluid type. The level of accuracy

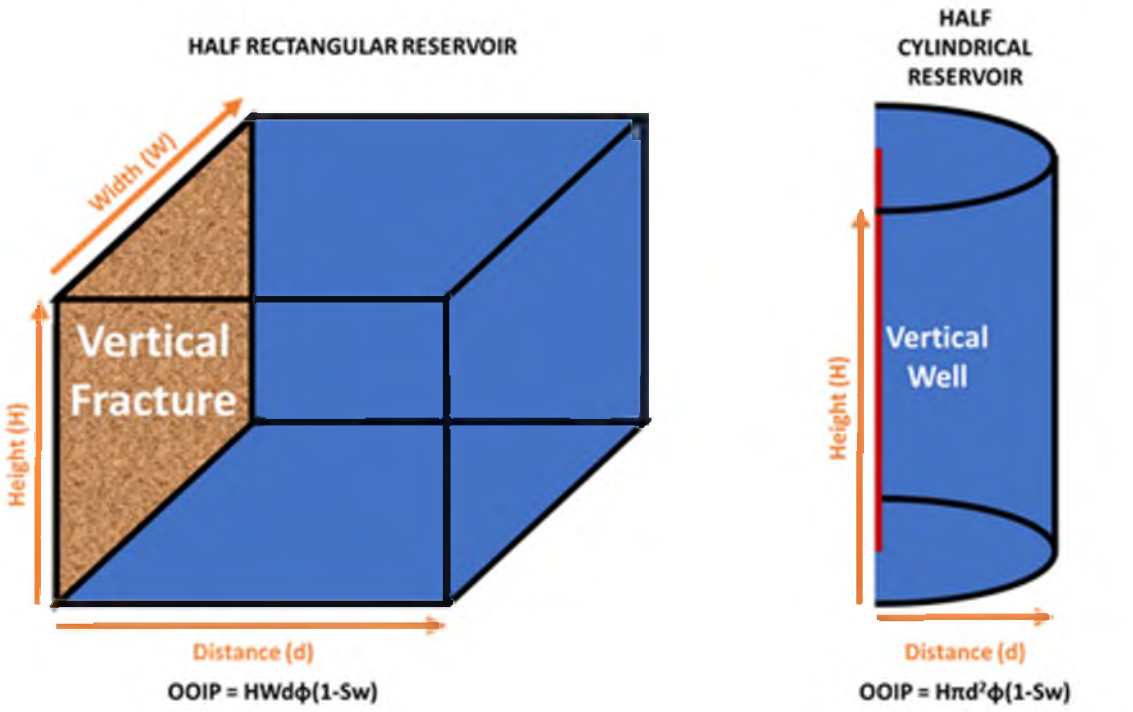

Figure 2.1 Original Oil In Place calculations for two systems showcasing the "Distance" variable

of pressure profiles calculated using this method will depend directly on the material balance equation being used and other factors which will be discussed in the upcoming sections.

2.2.1 Corrected Average Pressure

In some specific cases, the material balance may not be as accurate as desired and a modification to the method must be done. There are two main reasons why accuracy in this method may be affected:

- The near-fracture effect. Since interpolation to the known bottom-hole pressure takes place near the fracture or well, any phenomenon in this region is ignored (mostly gas coming out of solution). It was found that this has a

negligible effect depending on the Gas Oil Ratio (GOR).

- Material balance average pressure. Perhaps the most impactful on this method's accuracy is the difference between the calculated material balance average pressure (equilibrium average pressure) and average pressure during production. **Figure 2.2** shows average pressure decline in a reservoir where a well has been shut after one year of production. Average reservoir pressure continues to decline even after shutdown until it reaches an equilibrium point as determined by numerical simulation. Material Balance average pressure is the equilibrium average pressure at $t = \infty$, rather than at $t = 1$ year. The difference, ΔP, is a direct result of fluid compressibility, partial bubble point transition, and so forth. Average pressure difference is only substantial for cases of high GOR or dry gas reservoirs and may affect pressure profiles calculated by the material balance method.

In cases where the material balance may not be sufficiently accurate, the corrected average pressure method presented earlier is applied to obtain better results as shown in the upcoming examples.

To correct for the average pressure difference seen in **Figure 2.2**, the following relation is applied to gas reservoirs in conjunction with the method:

$$\int_0^L \frac{1}{B_g(P(x))}\partial x = \frac{L}{B_g(\bar{P})} \qquad 2.2$$

The development of this equation can be found in the upcoming sections in more rigorous forms. Equation 2.3 shows the oil equivalent of equation 2.2:

$$\int_0^L \frac{1}{B_o(P(x))}\partial x = \frac{L}{B_o(\bar{P})} \qquad 2.3$$

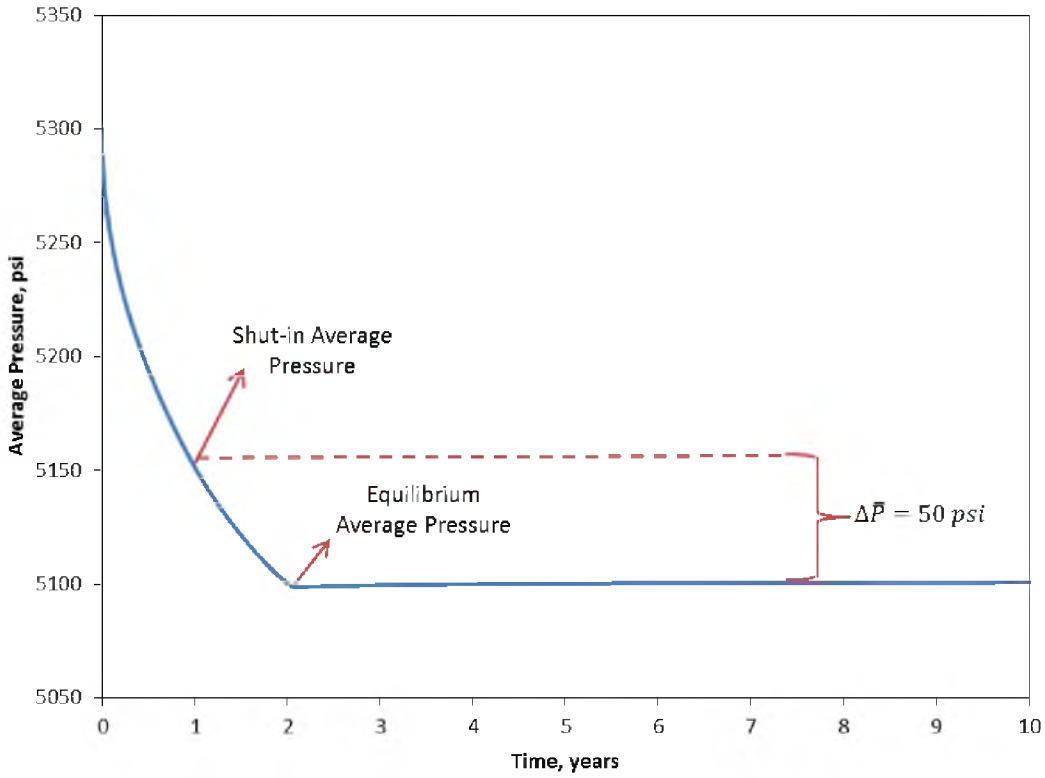

Figure 2.2 Difference between equilibrium average pressure (material balance pressure) and "real time" average pressure

Equation 2.3 can be rearranged in the following manner as shown in the corrected average pressure theory section:

$$\frac{wh}{5.61458}\int_0^L \frac{\phi(P(x))S_O(P(x))}{B_o(P(x))}\partial x = OOIP - N_p \qquad 2.4$$

The application of these equations to the material balance method will increase accuracy. However, some knowledge of relative permeability curves is needed when dealing with multiphase systems.

Example 1 shows the application of the material balance method to a multiphase case where no modification is needed. Example 2 shows a typical case where material balance alone may not meet accuracy requirements and the corrected average pressure modification

is introduced. Example 3 shows the application of the material balance with average pressure correction for a single-phase compressible fluid.

2.3 Case Examples

2.3.1 Example 1: Multiphase Linear Flow into a Vertical Fracture

Consider a single hydraulic vertical fracture draining from a low permeability matrix media with homogenous fluid saturations as depicted in **Figure 2.3**. This represents a portion of a multistage hydraulically fractured reservoir. The following assumptions are made with respect to the physical system.

- Infinite conductivity vertical fractures.
- Fractures can be adequately represented by a vertical plane.
- All fractures are identical and have similar production.

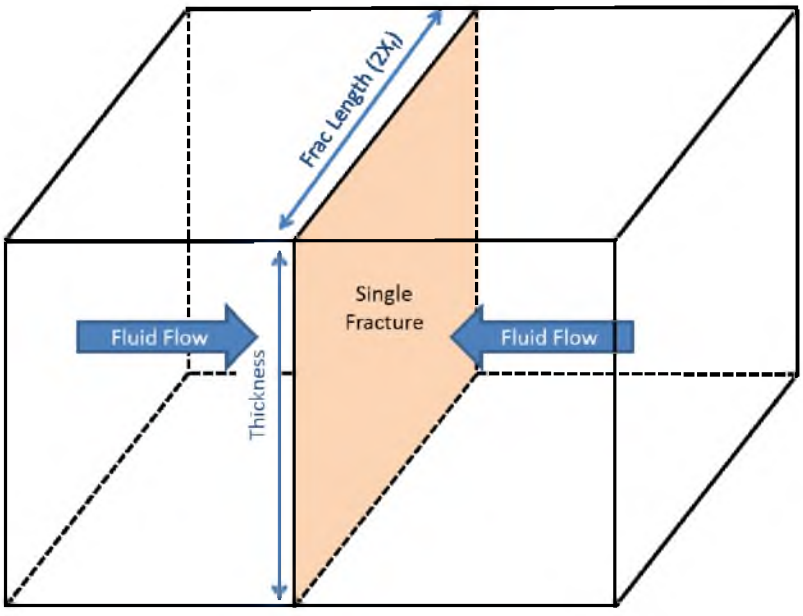

Figure 2.3 Linear flow into a vertical fracture

Using the production data and fluid information provided in **Table 2.1**, the method steps in the previous section are followed:

1. Setting up the conventional black oil material balance equation in the form of equation 2.1:

$$d = 5.61458\frac{B_{oi}(N_P(B_o + (R_P - R_s)B_g) - (W_e - W_p)B_w)}{2\phi wh\left((1 - S_{Wc})\left((B_o - B_{oi}) + (R_{si} - R_S)B_g\right) + (C_W S_{wc} + C_f)\Delta P B_{oi}\right)} \quad 2.5$$

Note that since there is no gas cap in the system then m = 0.

2. Using production data at an arbitrary time of 90 days, an average pressure plot was built as shown in bold in **Figure 2.4**.
3. A surrogate curve based on the single phase linear flow solution was used to match the average pressure curve and interpolate it to the known bottom-hole pressure of 500 psi. This curve is shown in **Figure 2.4** and was obtained by iterating through α in equation 2.6.

$$\bar{P}(x) = P_{wf} + (P_i - P_{wf})\left[\text{erf}\left(\frac{6.285311x}{\sqrt{\alpha t}}\right) + \frac{0.0897632}{x}\sqrt{\alpha t}\left(e^{-\frac{39.5051x^2}{\alpha t}} - 1\right)\right] \quad 2.6$$

4. Once a satisfying value for α was found, a pressure profile expression was determined by substitution and differentiation of equation 2.6 as shown by equation 2.7.

Table 2.1 Reservoir and operational parameters for simulations

	Oil Production STB		**Gas Production MSCF**		**GOR at P_b scf/stb**	**BHP psi**
	90 days	**1 year**	**90 days**	**1 year**		
Example 1	2147	4218	3050	5850	700	500
Example 2	2286	4540	8120	15300	1200	1000
Example 3	-	-	71782	231000	-	500

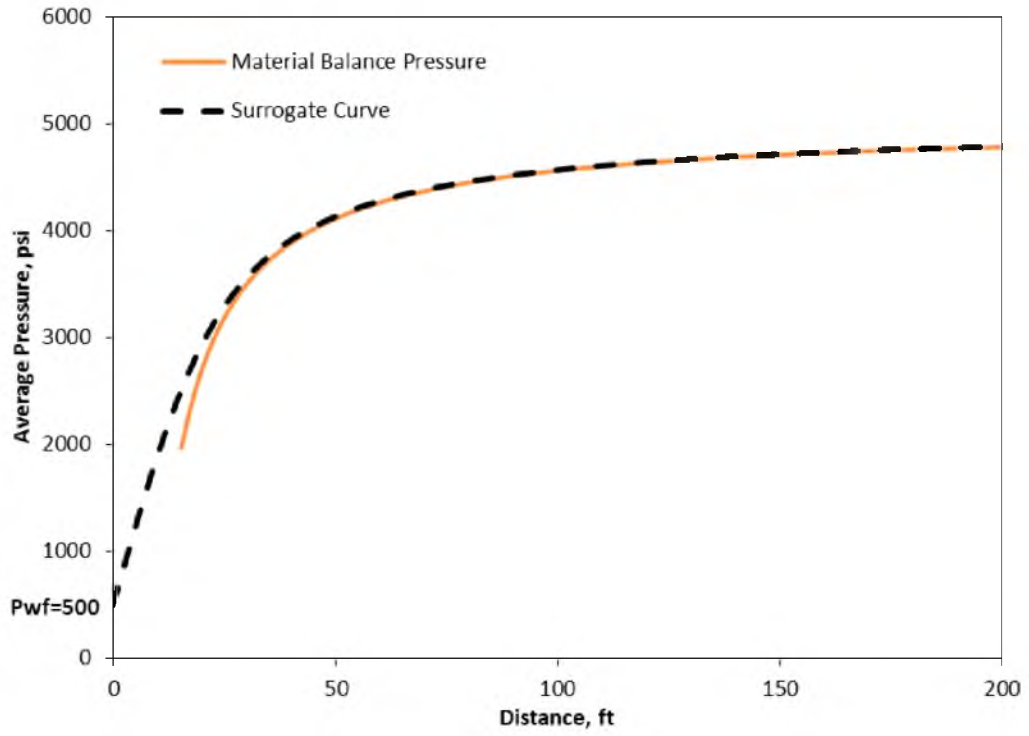

Figure 2.4 Average pressure profile matched by a surrogate curve

$$\bar{P} = \frac{\int_0^L P dV}{\int_0^L dV} = \frac{\int_0^L P(x)\, dx}{L} \qquad 2.7$$

The resulting expression is Miller's single phase linear flow solution as shown in equation 2.8.

$$P(x) = P_{wf} + (P_i - P_{wf})\,\mathrm{erf}\left(\frac{6.285311x}{\sqrt{\alpha t}}\right) \qquad 2.8$$

A set of pressure profiles at arbitrary production times of 90 days and 1 year were produced. Validation of these results was done through numerical simulation as shown in **Figure 2.5**.

5. Equation 2.8 represents Miller's single phase linear flow pressure behavior, where α is diffusivity as shown in equation 2.9.

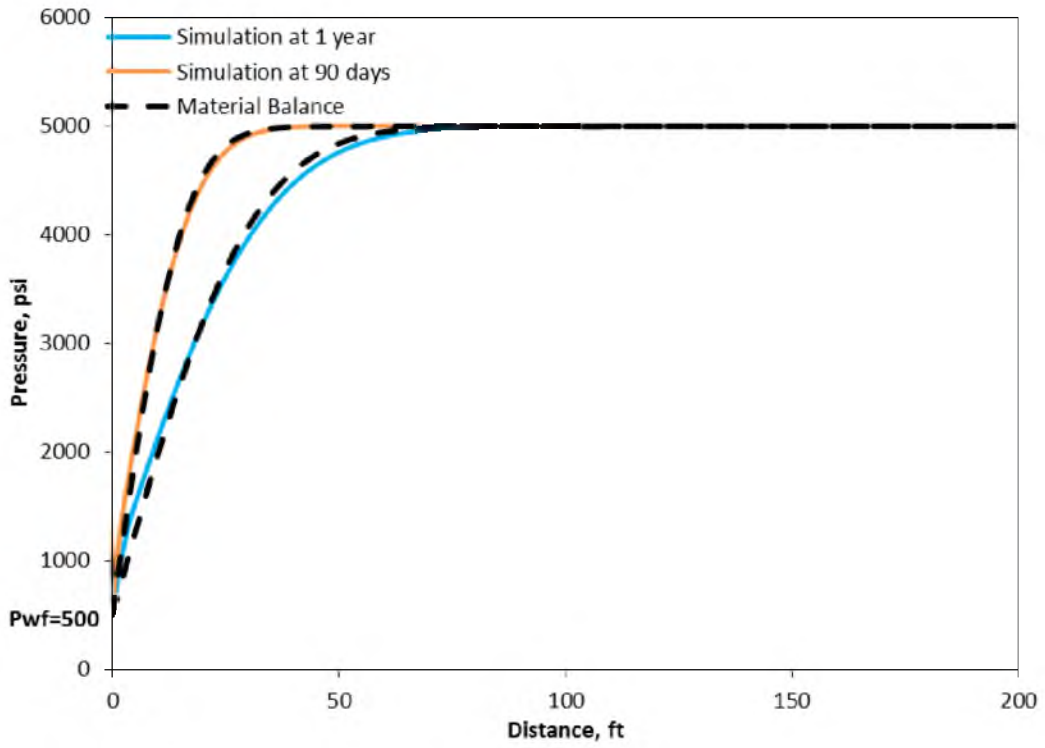

Figure 2.5 Calculated material balance pressure profiles versus simulation

$$\alpha = \frac{k}{\mu \phi c_t} \qquad 2.9$$

where $C_t = S_oC_o + S_gC_g + S_wC_w + C_f$, and can be estimated using weighted average values.

By simple substitution, permeability was calculated to be around 180 nD, a very good estimation when compared to the actual absolute permeability of 200 nD.

The agreement between the calculated MBPP's (Material Balance Pressure Profiles) and numerical simulation pressure profiles is remarkable as shown in **Figure 2.5**. The slight variation near the well is due to gas coming out of solution. In certain cases where GOR is not very high, gas contribution to this process can be safely ignored by simplifying equation 2.5 into equation 2.10.

$$d = 5.61458\frac{B_{oi}(N_P B_o - (W_e - W_p)B_w)}{2\phi wh\left((1 - S_{Wc})(B_o - B_{oi}) + \left(C_W S_{wc} + C_f\right)\Delta P B_{oi}\right)} \qquad 2.10$$

Equation 2.10 comes in handy for quick calculations where GOR is not considerably high. As GOR increases, the accuracy of MBPP's and permeability calculations may be reduced. However, even in cases where GOR is quite high, MBPP's are still a decent approximation to a full numerical simulation model. This is shown in Example 2.

It should be noted that a 'manual' interpolation from the average pressure curve to the known bottom-hole pressure is also acceptable. The advantage of having surrogate curves is their easy incorporation into the methodology. Also, surrogate curves are in many cases solutions to known fluid flow phenomena that contain important physical properties that can be back-calculated. In other words, parameters such as permeability or diffusivity are readily obtainable with this method. However, one should be cautious as most of these surrogate curves are based on one-phase flow. Other surrogate curves similar to Miller's expression can be found in the oil and gas literature and transport books such as Bird's Transport Phenomena (1960).[19]

2.3.2 Example 2: Multiphase Linear Flow into a Vertical Fracture and High GOR

In this case, the same steps as in Example 1 were followed using production data from **Table 2.1** to produce pressure profiles shown in **Figure 2.6**. As mentioned earlier, the match between calculated pressure profiles and output from numerical simulation is not as good as in Example 1. However, MBPP's are a very good approximations given that no knowledge about matrix permeability, relative permeabilities nor production rates are required for this method.

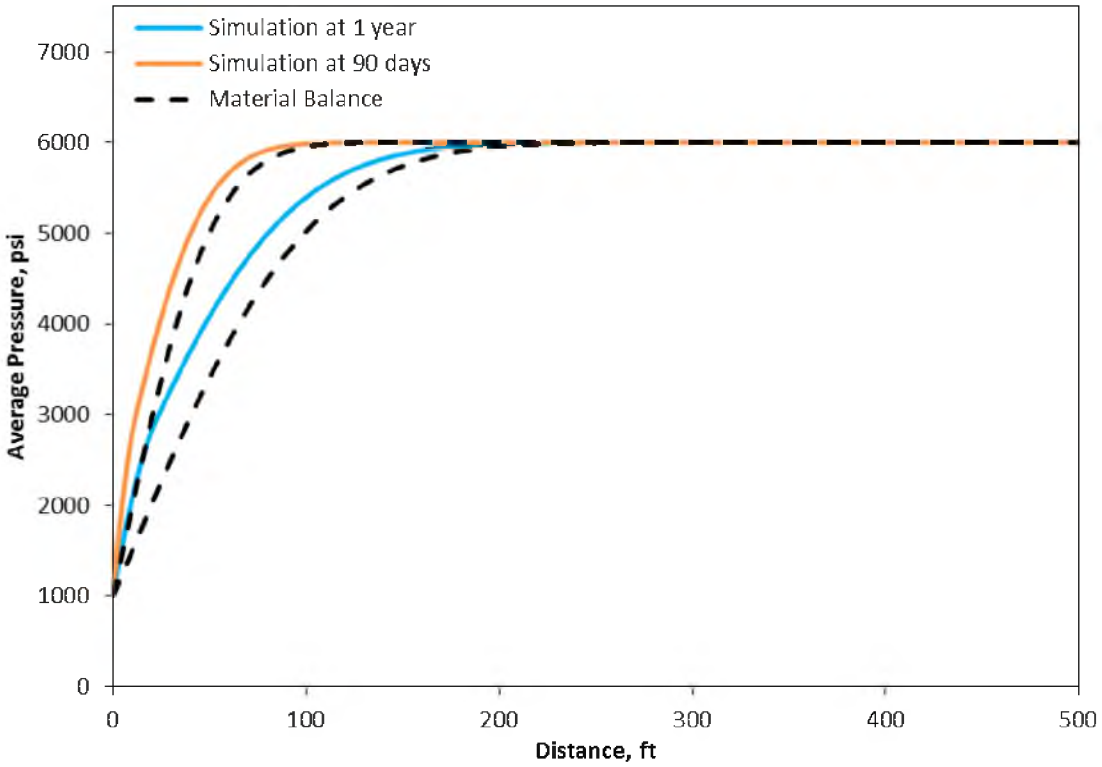

Figure 2.6 Calculated material balance pressure profiles versus simulation

2.3.3 Example 2 (Revisited): Multiphase Linear Flow into a Vertical Fracture and High GOR

The implementation of equation 2.4 to the material balance method for increased accuracy is shown in this section. In this procedure, a new term "L", defined as an arbitrarily large number, is introduced.

1. Using surrogate pressure equation 2.8 and an arbitrary value for α, $P(x)$ for $x \in [0,L]$ was plotted.

$$P(x) = P_{wf} + (P_i - P_{wf})\,\mathrm{erf}\left(\frac{6.285311x}{\sqrt{\alpha t}}\right) \qquad 2.8$$

2. The product in the left hand side of equation 2.4 was calculated numerically using a pressure profile as determined in step 1.

$$\frac{wh}{5.61458}\int_0^L \frac{\phi(P(x))S_O(P(x))}{B_o(P(x))}\partial x = OOIP - N_p \qquad 2.4$$

Porosity is a function of pressure, but it may be assumed constant and be taken out of the integral for most cases. Also, before gas comes out of solution oil within the reservoir, saturation profile is best represented by an error function. After gas comes out of solution, oil saturation profile can be approximated by a linear function. Hence, if instantaneous gas oil ratio remains constant, oil saturation may be estimated by:

$$S_o(x) = S_o{}^*(BHP) + (S_{oi} - PS_o(BHP))\,\mathrm{erf}\left(\frac{6.285311x}{\sqrt{\alpha t}}\right) \qquad 2.11$$

where So*(BHP) is defined as:

$$S_o{}^*(BHP) = \frac{S_o(BP) - S_{oi}\mathrm{erf}\left(\frac{6.285311x}{\sqrt{\alpha t}}\right)}{1 - \mathrm{erf}\left(\frac{6.285311x}{\sqrt{\alpha t}}\right)} \qquad 2.12$$

Oil saturation at the bubble point is:

$$S_o(BP) = 1 - \frac{Sw_i\left(1 - C_w(P_{bp} - P_i)\right)}{1 + C_f\left(P_{bp} - P_i\right)} \qquad 2.13$$

If instantaneous gas oil ratio shows signs of gas coming out of solution within the reservoir, a linear relationship describes oil saturation as shown in equation 2.14.

$$S_o(x) = S_o(BP) + \frac{\left(1 - Sw(BHP) - S_g(BHP) - S_o(BP)\right)(x_{bp} - x)}{x_{bp}} \qquad 2.14$$

In this case, gas and water saturations at the bottom-hole pressure can be calculated either analytically or iteratively by solving equations 2.15, 2.16, and 2.17 at the same time.

$$K_{ro} = (K_{ro})_{Swc}\left[\left(\frac{K_{row}}{(K_{ro})_{Swc}} + K_{rw}\right)\left(\frac{K_{rog}}{(K_{ro})_{Swc}} + K_{rg}\right) - (K_{rw} + K_{rg})\right] \quad 2.15$$

$$\frac{K_{rw}}{K_{ro}} = WOR\frac{\mu_w B_w}{\mu_o B_o} \quad 2.16$$

$$\frac{K_{rg}}{K_{ro}} = (GOR - R_s)\frac{\mu_g B_g}{\mu_o B_o} \quad 2.17$$

3. OOIP was volumetrically determined by assuming that "L" from step 1 defines the extent of the reservoir. This was then used to calculate the right hand side of equation 2.4.
4. A value of α was iteratively found in equation 2.8 so that the equality in equation 2.4 was satisfied.
5. Steps 1 through 4 were repeated for arbitrary production times of 90 days and 1 year. Resulting pressure profiles are shown in **Figure 2.7**.

It is clear from **Figure 2.7** that pressure profiles determined using corrected average pressures are more accurate than regular material balance pressure profiles. The trade off, however, is a more complex and involved method that requires some knowledge about relative permeability data. The choice of method is then left to judgement according to acceptable accuracy and available resources.

Equation 2.4 may only be satisfied with the correct pressure profile using oil production. The gas equivalent is shown in equation 2.18. Both equations can be used separately or in combination in a multiphase system.

$$\frac{wh}{5.61458}\int_0^L \left(\frac{\phi(P(x))S_o(P(x))R_s(P(x))}{B_o(P(x))} + \frac{\phi(P(x))S_g(P(x))}{B_g(P(x))}\right)\partial x = GOIP - G_p \quad 2.18$$

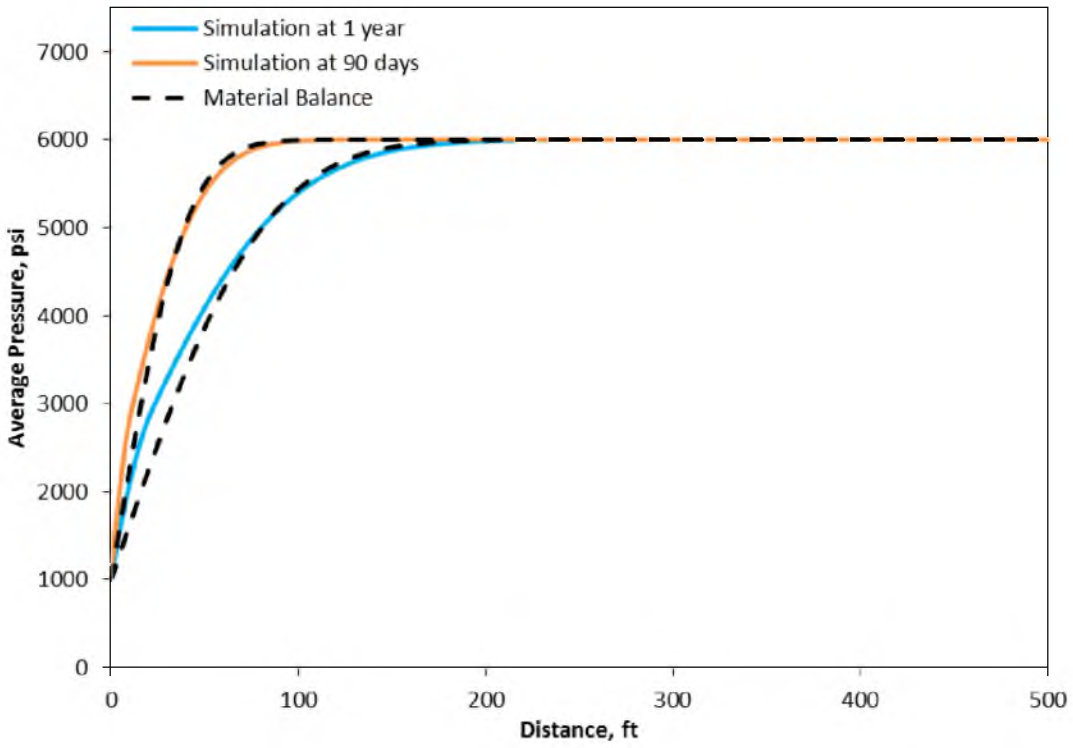

Figure 2.7 Pressure profiles determined using corrected average pressures

2.3.4 Example 3: Gas Linear Flow into a Fracture

This is a good example where application of the material balance method requires the corrected average pressure for substantially better accuracy. Fortunately, the procedure in this case is much simpler than Example 2 due to the fact that this is a single-phase system. The following steps summarize the application of the material balance method for dry gas systems.

1. The dry gas material balance equation was set in the form of equation 2.1.

$$d = 5.61458\frac{B_{gi}(G_pB_g + W_pB_w)}{2\phi wh\left((1-S_{Wc})(B_g - B_{gi}) + (C_WS_{wc} + C_f)\Delta PB_{gi}\right)} \qquad 2.19$$

2. Using an arbitrary production time of 90 days from **Table 2.1**, a plot $\bar{P}$ of vs d was built.

3. A surrogate curve based on the gas linear flow solution was used to match the average pressure curve and interpolate it to the known bottom-hole pressure of 500 psi. This curve was obtained by iterating through α in equation 2.20.

$$\bar{P}(x) = \frac{\int_0^L \sqrt{{P_{wf}}^2 + \left({P_i}^2 - {P_{wf}}^2\right) \operatorname{erf}\left(\frac{6.285311x}{\sqrt{\alpha t}}\right)}\, dx}{L} \qquad 2.20$$

4. Once a satisfying value for α was found, a pressure profile expression was determined by substitution and differentiation of equation 2.20 as shown by equation 2.7 in Example 1.

$$P(x) = \sqrt{{P_{wf}}^2 + \left({P_i}^2 - {P_{wf}}^2\right) \operatorname{erf}\left(\frac{6.285311x}{\sqrt{\alpha t}}\right)} \qquad 2.21$$

Equation 2.21 describes an estimate to compressible linear flow solution and was plotted for arbitrary production times of 90 days and 1 year for comparison with numerical simulation in **Figure 2.8**.

It is clear from **Figure 2.8** that MBPP's do not match numerical simulation and the usage of corrected average pressures may be required. For this purpose, steps similar to Example 2 were followed:

1. Using surrogate pressure equation 2.21 and an arbitrary value for α, $P(x)$ for $x \in [0,L]$ was plotted. Note that "L" is defined as an arbitrarily large number.

$$P(x) = \sqrt{{P_{wf}}^2 + \left({P_i}^2 - {P_{wf}}^2\right) \operatorname{erf}\left(\frac{6.285311x}{\sqrt{\alpha t}}\right)} \qquad 2.21$$

2. The product in the left hand side of equation 2.22 was calculated numerically using a pressure profile as determined in step 1.

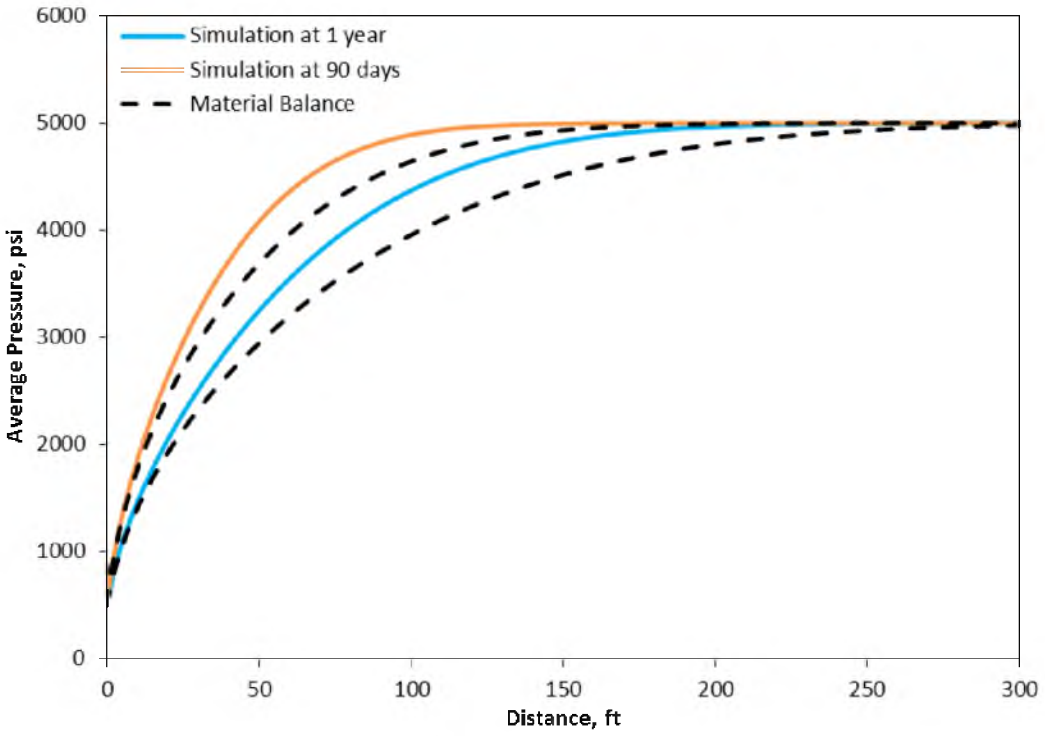

Figure 2.8 Pressure profiles determined using the material balance method

$$\frac{wh\phi}{5.61458}\int_0^L \frac{1}{B_g(P(x))}\partial x = GOIP - G_p \qquad 2.22$$

Note that equations 2.4 and 2.22 are similar in nature, except that equation 2.22 is easier to calculate as it applies to a single-phase system.

3. GOIP was volumetrically determined by assuming that "L" from step 1 defines the extent of the reservoir. This was then used to calculate the right hand side of equation 2.22.
4. A value of α was iteratively found in equation 2.21 so that the equality in equation 2.22 was satisfied.
5. Steps 1 through 4 were repeated for arbitrary production times of 90 days and 1 year. Resulting pressure profiles are shown in **Figure 2.9**.

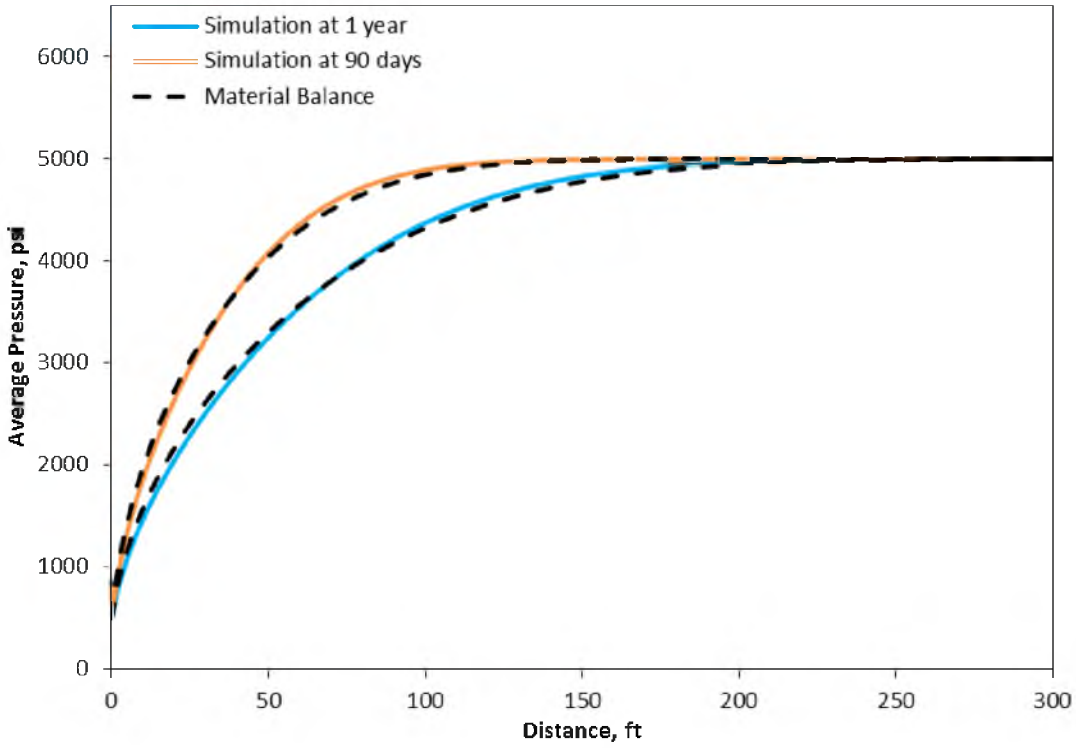

Figure 2.9 Pressure profiles determined using corrected average pressures

Inspection of **Figure 2.8** and **Figure 2.9** clearly show substantial improvement by using corrected average pressures in the material balance method. For single-phase cases, this implementation is simple and is highly recommended for compressible fluids.

2.3.5 Example 4: Permian Basin Field Case

This field case study consists of a multistage hydraulically fractured horizontal well with over 90 hydraulic fractures. The reservoir is composed of several layers with different petro-physical properties. However, the ranges for these properties are narrow and a weighted average was calculated for the whole system.

Artificial lift is introduced to help increase drawdown after 70 days of production. The

bottom-hole pressure takes about 100 days to stabilize. After this time, the bottom-hole pressure reaches a more stabilized value of about 500 psi as determined by empirical multi-phase flow correlations. Even though MBPP's may be determined with varying bottom-hole pressures, a constant value of 500 psi was used to keep the method simple.

Using a procedure identical to Example 1, permeability was calculated as a function of time. **Figure 2.10** shows normalized fluid production rates and calculated permeability for a production time of almost 2 years. "Material balance permeability" trends see an initial increase until it levels off at around 600 nanodarcies. This is expected given that bottom-hole pressure stabilizes during this time. The estimated permeability of 600 nD is consistent with the range of permeabilities measured for samples from this well.

Although permeability calculations by using material balance are possible, the analytical tools made available by this method may be of more interest. One important aspect of this plot happens at 600 days, where the permeability skyrockets. Looking at oil and gas rates there is no reason for the permeability to escalate, but a big surge in water production occurs at this time. Because the conventional material balance used in this particular case accounts for multiphase behavior, the spike in water production translates in higher observed permeability. Average reservoir pressure decline was also calculated by assuming a stimulated reservoir volume based on fracture dimensions as shown in **Figure 2.11**.

This field example demonstrates the applicability of the method developed in this research work. It should be noted that the production rates did not stabilize for some time and that the well was shut down from time to time. The bottom-hole pressure also varied over the production time studied. Despite these complications in data collection, material

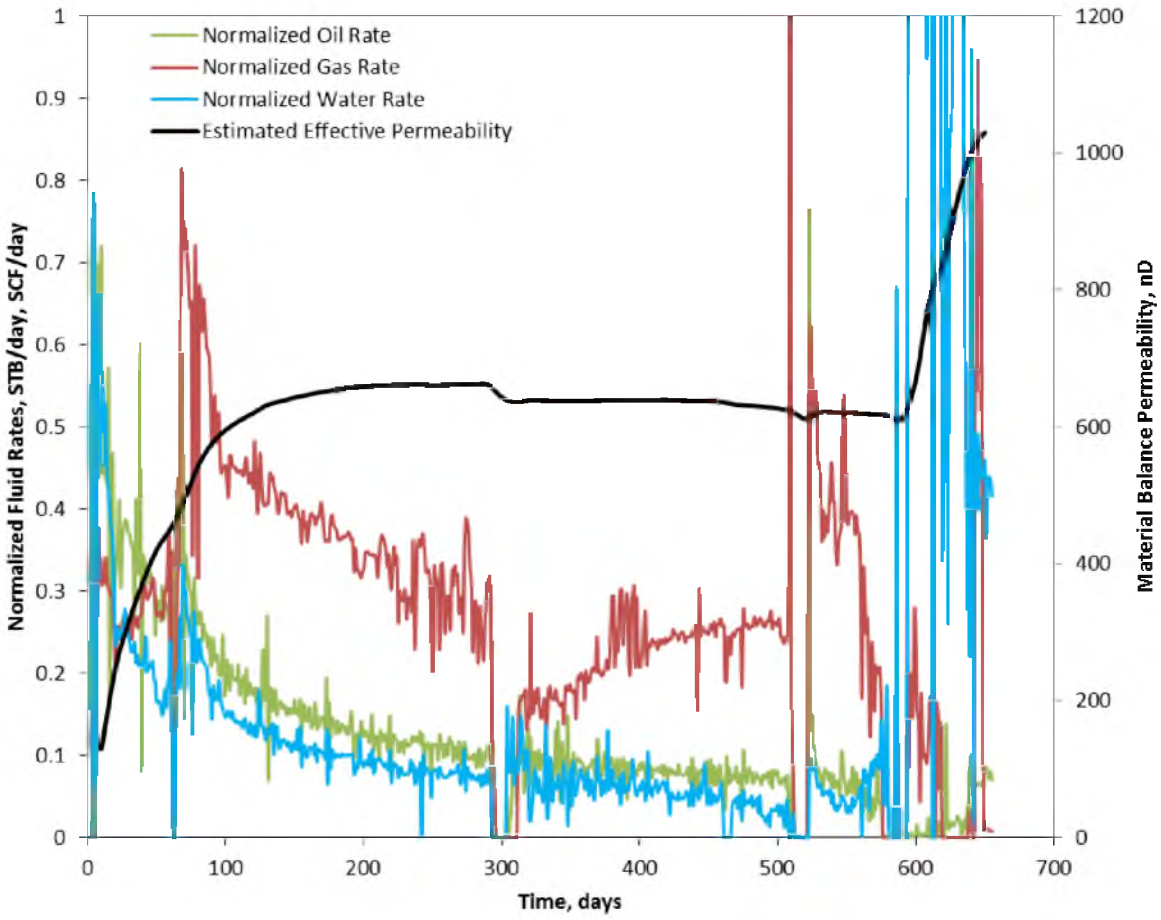

Figure 2.10 Transient material balance method application to a field case

balance permeability was calculated and analyzed. Not only does the method provide an estimate of permeability that is consistent with production and pressures, but it also helps analyze major disturbances (like the water surge as seen in **Figure 2.11**. Material balance permeability also seems to be sensitive to long shutdowns as seen at around 300 and 500 days of production. Other helpful production analytics can be implemented into this workflow thus making this a potential topic for future research work.

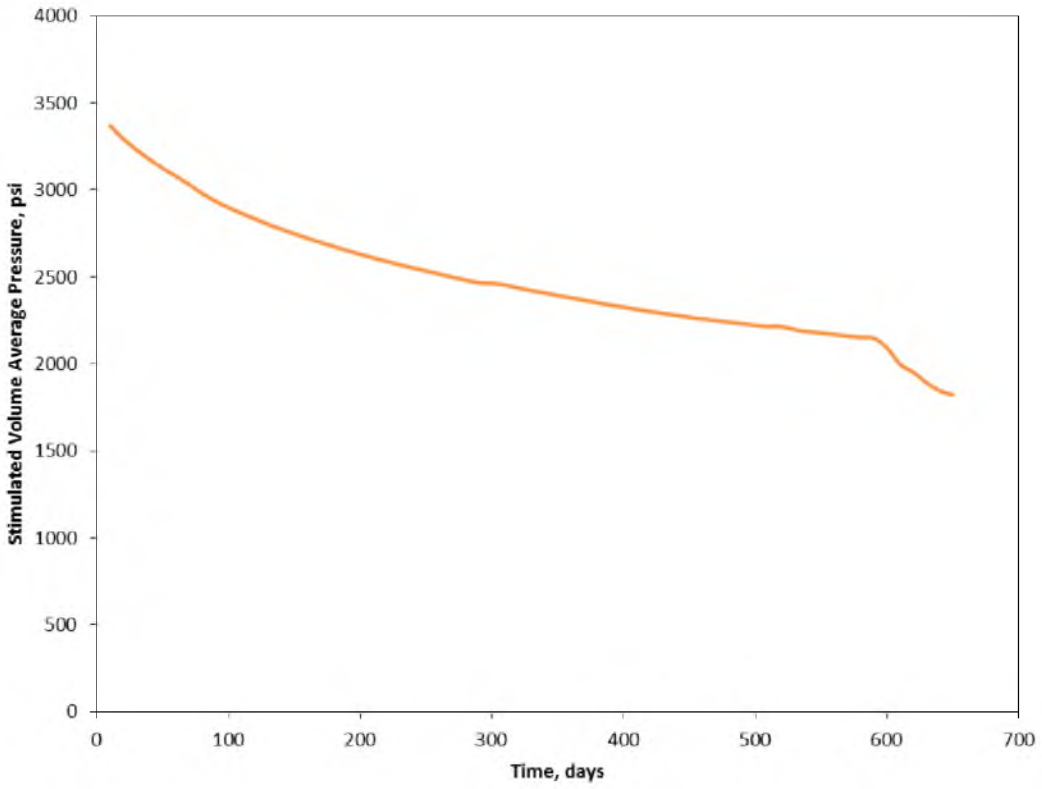

Figure 2.11 Field case calculated average pressure decline

2.4 Other Applications

As discussed earlier, surrogate curves used in this method are derived from one-phase equations developed by Miller (1962)[17] and presented by Katz et al. (1959).[16] Therefore, there are some physically important variables that can be extracted from these curves as is the case of permeability and diffusivity.

Even though calculated permeabilities using the material balance method were very good estimates, the actual power of the method lies in its potential use for analytics. This was shown in Example 4, where permeability was calculated using production data points for about 2 years. A material balance permeability versus time plot was used to quantify the impact of artificial lift on production and assess the impact of a production water surge.

As a rule of thumb, **Figure 2.12** shows the material balance permeability behavior of a true infinite reservoir. The flat portion represents the estimated permeability and any deviations could be a result of significant fracture interference, fracture closure or boundary dominated flow. Hence, this plot can be further studied and important reservoir behavior can be derived as a consequence.

Another important piece of information that can be derived from this method is pressure decline. **Figure 2.11** shows that reservoir average pressure decline computations are possible with this method. Pressure decline at particular points in the reservoir are also possible as shown in **Figure 2.13**. Comparison with pressure sensor information would provide decent insight into the system's behavior.

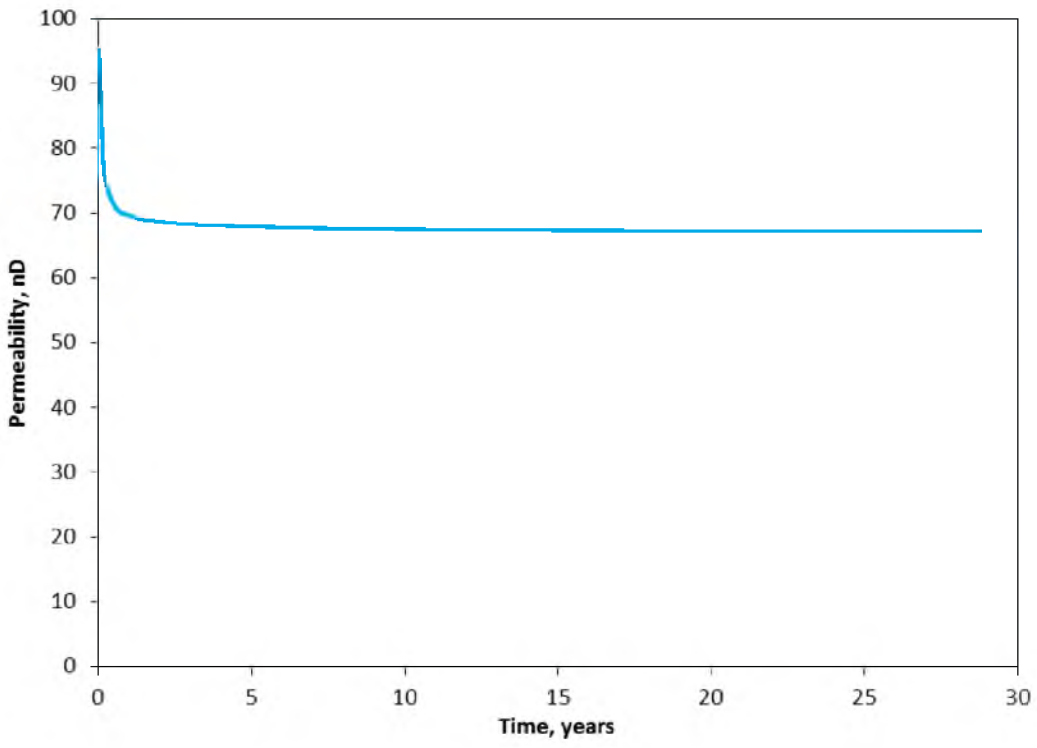

Figure 2.12 Calculated material balance permeability for an infinite reservoir

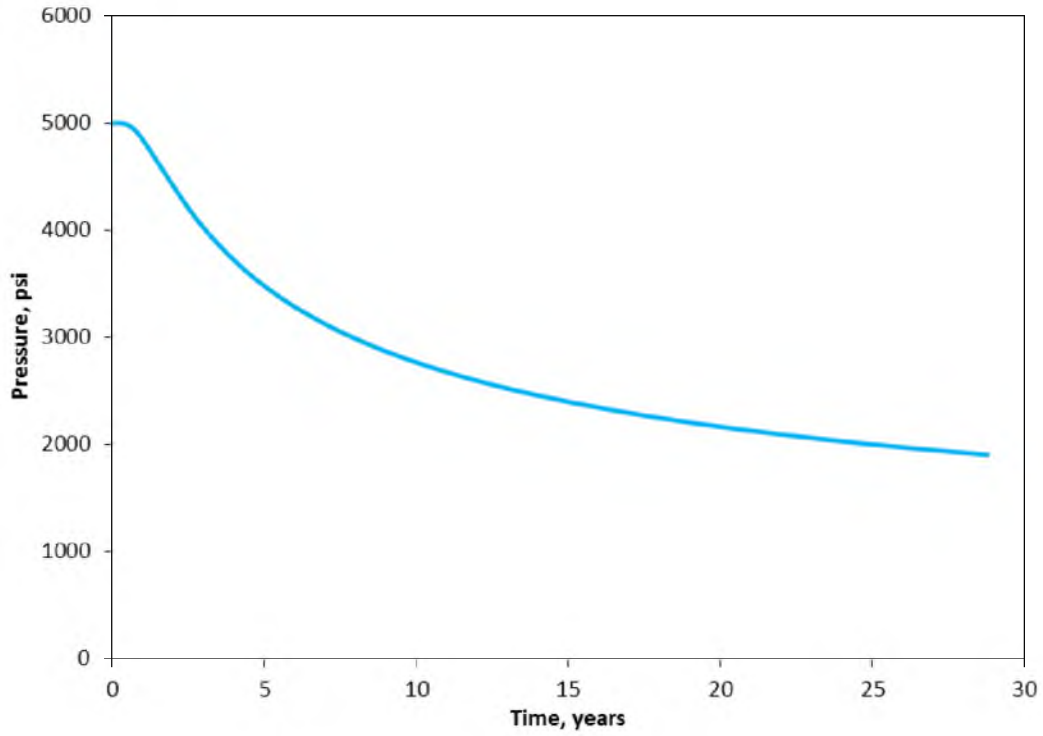

Figure 2.13 Pressure decline over time at a point 50 ft away from a draining fracture

As described in Example 2 (revisited), fluid saturation calculations are also possible after pressure profiles are established. Even though important assumptions regarding the system were made, this serves as an example of potential opportunities for analysis. **Figure 2.14** shows the oil saturation profile developed after an arbitrary production time. These are a few examples that serve as supplementary analytical tools for reservoir assessment. Analytical options using the transient material balance workflow are significant and easily available with minimum information about the reservoir.

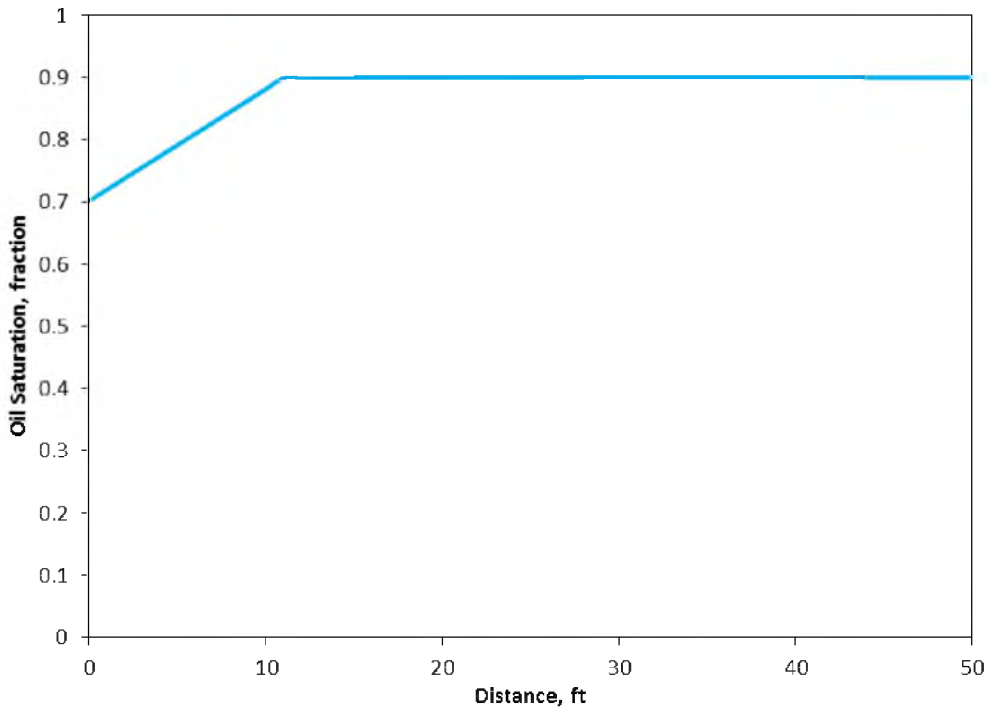

Figure 2.14 Calculated oil saturation profile

2.5 Key Findings

In this work, it was shown that pressure profiles for a transient-flow system can be determined using a method based on conventional material balance. The method's basic steps and theory were presented and its results were compared to numerical simulation and applied to an unconventional field case. Material Balance pressure profiles seem to be a decent approximation to single and multiphase systems. Important reservoir information such as permeability and average reservoir pressure decline can be extracted from the use of this method. When compressible fluids are flowing to the wellbore, a modified step was presented to improve accuracy. The applicability of the method was demonstrated by comparing results of several cases with results from a reservoir simulator. A field case from the Permian Basin further validated the method.

The material balance approach combined with pressure profile calculations uses cumulative fluid production data and fluid properties. In low-permeability shale reservoirs, early transient flow is expected to last for a long period of time, and this method allows for the extraction of important reservoir information. While weaknesses on this method have to do with the assumptions of the material balance formulation, it was shown that this workflow can be used as a reservoir assessment tool requiring only limited data.

2.6 Method Development

2.6.1 Material Balance Theory

In this section, a brief summary of the material balance theory is introduced. Consider a case where a single-phase incompressible fluid flows linearly into a fracture as shown in **Figure 2.3**. If the flow is transient, a pressure profile is developed during production and may be represented by equation 2.23 as described by Miller.

$$P(x) = P_{wf} + (P_i - P_{wf})\,\mathrm{erf}\left(\frac{6.285311x}{\sqrt{\frac{kt}{\mu\phi c_t}}}\right) \qquad 2.23$$

Assume that half of this system is represented by **Figure 2.1** and that the "distance" variable in this system is an arbitrary large number "L". Consider a second system identical to the first one, but its "distance" variable is "L*", where $L^* > L$.

Both systems are identical, except that the first system is smaller than the second. If both systems are flowing during the transient stage, then pressure fronts have not yet reached the boundaries of the system at L^* or L. A sample transient pressure profile developed in both systems is shown in **Figure 2.15**.

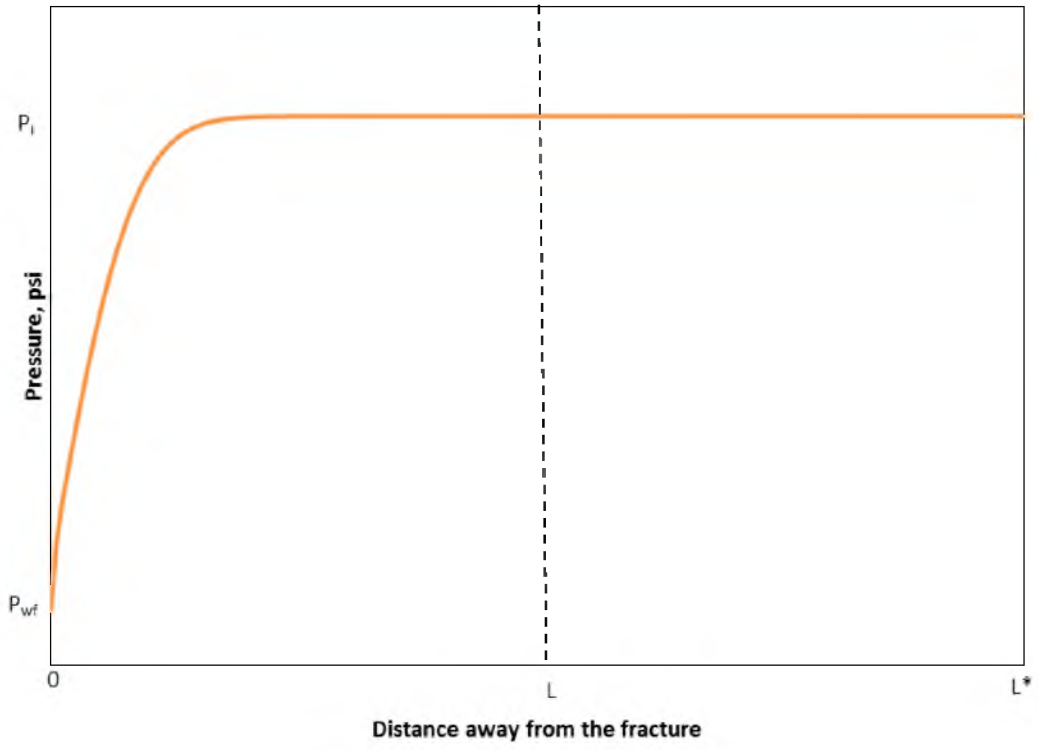

Figure 2.15 Typical error function pressure profile

It is clear from **Figure 2.15** that $P(L) = P(L^*) = Pi$, hence the pressure for any distance greater than L will be the initial pressure. It follows from this idea that any reservoir size larger than L will span identical pressure profiles.

The same concept can be applied to average pressure profiles. Through application of volumetric average pressure relation 2.7, equation 2.24 is obtained and an average pressure profile can be plotted as shown in **Figure 2.16**.

$$\bar{P} = \frac{\int_0^L P dV}{\int_0^L dV} = \frac{\int_0^L P(x)\, dx}{L} \qquad 2.7$$

$$\bar{P}(x) = P_{wf} + (P_i - P_{wf})\left[\text{erf}\left(\frac{6.285311x}{\sqrt{\frac{kt}{\mu\phi c}}}\right) + \frac{0.0897632}{x}\sqrt{\frac{kt}{\mu\phi c}}\left(e^{-\frac{39.5051x^2}{kt}} - 1\right)\right] \qquad 2.24$$

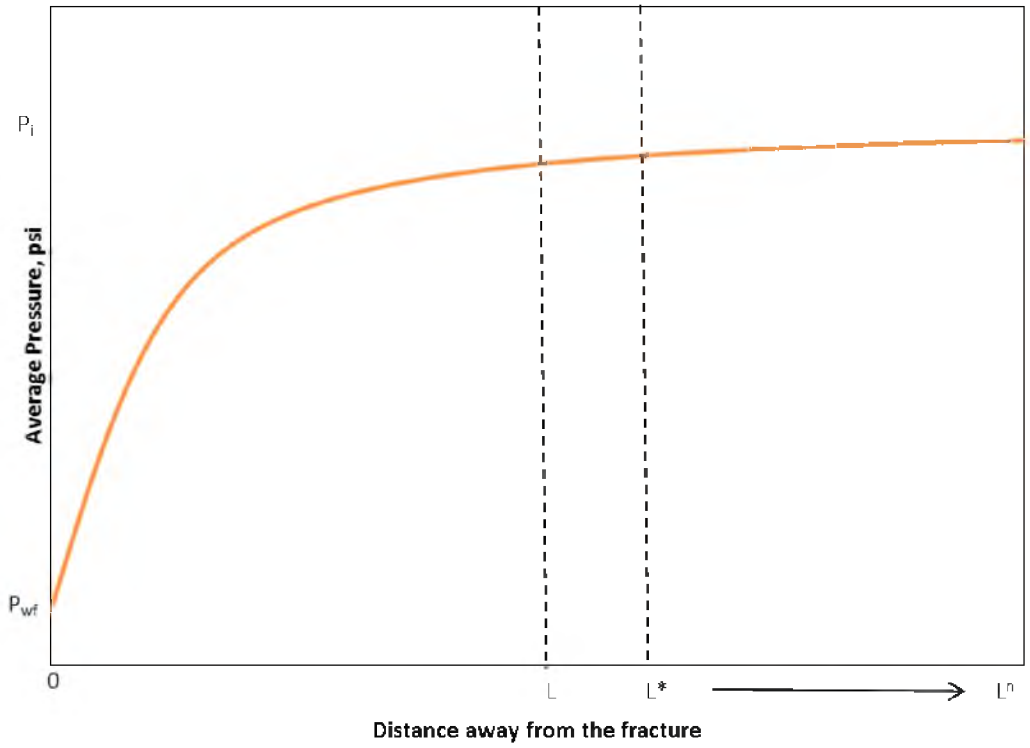

Figure 2.16 Average pressure profile plot calculated by varying L

If an average pressure curve such as the one shown in **Figure 2.16** is obtained by an alternative method, a pressure profile may be "back-calculated" without knowledge of permeability, viscosity, and so forth. Also, permeability and diffusivity values can be back-calculated by simple substitution.

The novel idea behind the transient flow material balance is the fact that a conventional material balance formulation is used to independently calculate average reservoir pressures at different values of "distance" or in this case L, L^* and L^n as shown in **Figure 2.17**.

The material balance method provides with a good average pressure profile until it breaks down in the near-well region. There are several reasons for this behavior, one of which is partly due to the concept that reservoirs of varying extents (quantified by the use

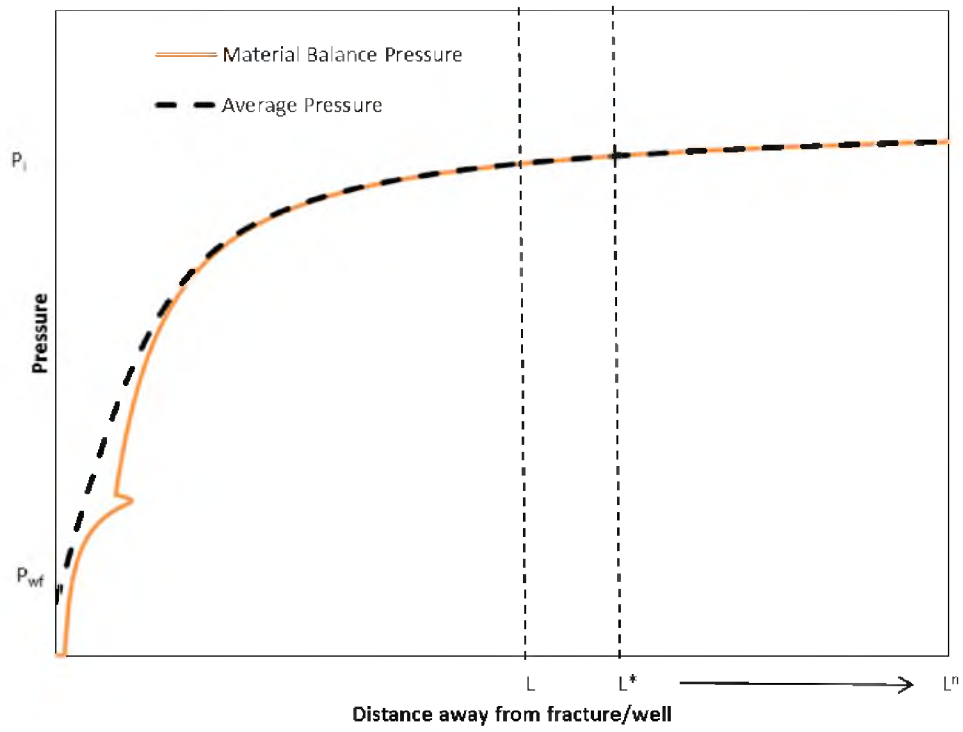

Figure 2.17 Material balance average pressure compared to an average pressure surrogate curve

of the "distance" variable) span identical pressure profiles. This only holds as long as the extent of the reservoir is "large" enough for the flow to be considered transient.

Since material balance makes use of production data, different pressure profiles can be calculated at different production data points. Diffusivity and permeability calculations can also be made for a range of production data points for analysis.

2.6.2 Corrected Average Pressure Theory

It was found that there is a difference between material balance (equilibrium) average pressure and average pressure while producing. The aim here is to find the average pressure difference, so that a corrected average pressure can be determined. To do this, a simple

equation relating equilibrium and producing average pressure is needed, and is presented as follows.

Consider a simple case of a reservoir consisting of two tanks. Both tanks have 100% porosity, 100% oil saturation, and have the same volume. Tank 1 has a pressure of 2000 psi and tank 2 has a pressure of 5000 psi as shown in **Figure 2.18**.

Since both tanks are identical, except for their pressures, the instantaneous average pressure of this system is 3500 psi, which is the arithmetic average of 2000 and 5000. However, simulation shows that the equilibrium average pressure of this system at equilibrium is 3540, a 40 psi difference from the instantaneous average.

To equate both, instantaneous and equilibrium systems, their corresponding oil volumes are brought to atmospheric pressures (produce this fluid). The atmospheric fluid volume of systems must be exactly the same. This is equity is visualized in **Figure 2.19**.

Mathematically, **Figure 2.19** is expressed in equation 2.25.

$$\frac{V_1}{Bo_1} + \frac{V_2}{Bo_2} = \frac{V_1 + V_2}{B_o(\bar{P})} \qquad 2.25$$

Or,

$$\frac{V_1}{Bo_1} + \frac{V_2}{Bo_2} = \frac{V_{Total}}{B_o(\bar{P})} \qquad 2.26$$

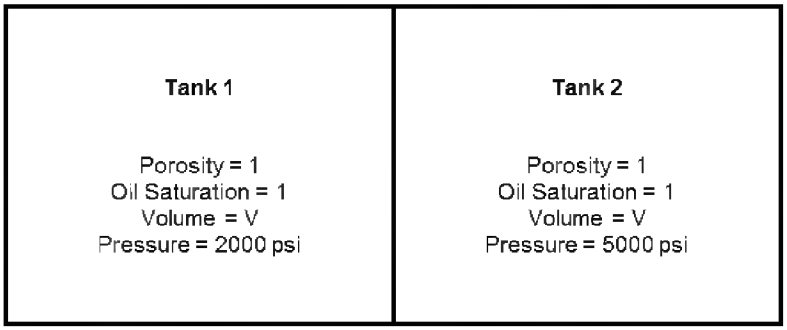

Figure 2.18 System consisting of Tanks 1 and 2

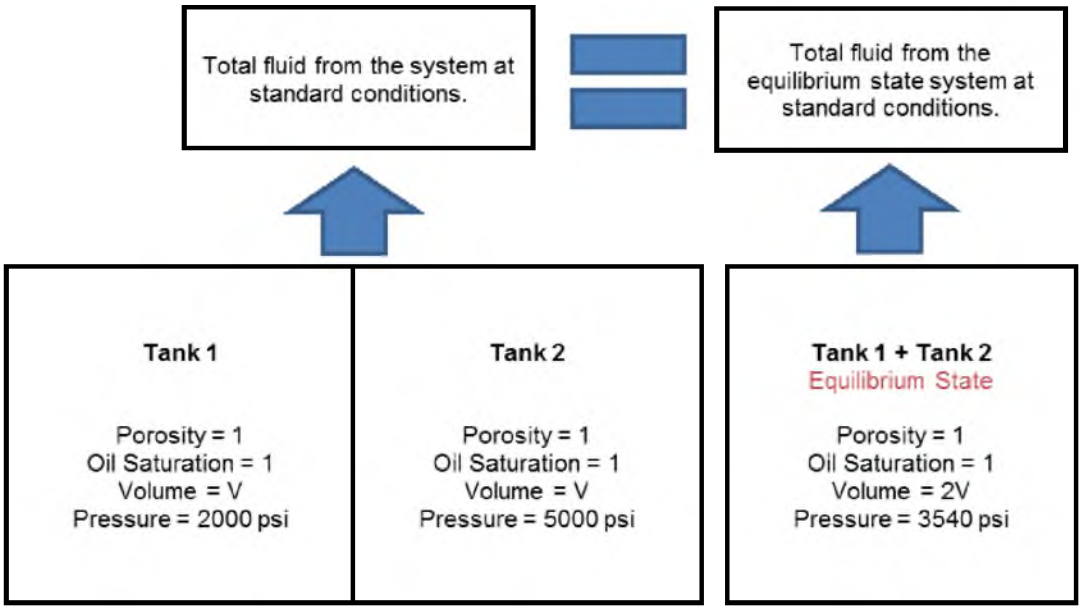

Figure 2.19 Equivalence between Tanks 1 and 2 at producing state and Tanks 1 and 2 at equilibrium state

By taking into account that both tanks have the same volume, and expanding this to an arbitrary number of tanks, the following relation can be established.

$$\sum_{i=1}^{n} \frac{d_i}{Bo_i} = \frac{L}{B_o(\bar{P})} \tag{2.27}$$

where d_i and L are individual tank length and sum of all tank lengths correspondingly. Equation 2.27 can also be expressed as an integral.

$$\int_0^L \frac{1}{B_o(P)} \partial x = \frac{L}{B_o(\bar{P})} \tag{2.28}$$

A more rigorous expression that takes into account porosity and oil saturation can be similarly derived.

$$\int_0^L \frac{\phi(P) S_O(P)}{B_o(P)} \partial x = \frac{L\phi(\bar{P}) S_O(\bar{P})}{B_o(\bar{P})} \tag{2.29}$$

Similarly, this relation can be obtained for the gas case as shown by equation 2.30.

$$\int_0^L \frac{\phi(P)S_g(P)}{B_g(P)}\partial x = \frac{L\phi(\bar{P})S_g(\bar{P})}{B_g(\bar{P})} \quad 2.30$$

Equation 2.31 results from equation 2.30 for the case of a rectangular reservoir as shown in **Figure 2.3**.

$$\frac{wh}{5.61458}\int_0^L \frac{\phi(P)S_O(P)}{B_o(P)}\partial x = OOIP - N_p \quad 2.31$$

For a rectangular multiphase reservoir, a gas analogous expression is similarly derived.

$$\frac{wh}{5.61458}\int_0^L \left(\frac{\phi(P)S_o(P)R_s(P)}{B_o(P)} + \frac{\phi(P)S_g(P)}{B_g(P)}\right)\partial x = GOIP - G_p \quad 2.32$$

Equations 2.31 and 2.32 may be used separately or in combination to obtain more accurate results than the basic transient material balance approach. The solutions to these equations can be reached numerically or analytically depending on the PVT data format.

CHAPTER 3

RESERVOIR SIMULATION SIMPLIFICATION WORKFLOW FOR HYDRAULICALLY FRACTURED RESERVOIRS

Production from unconventional formations, such as shales, has significantly increased in recent years by stimulating large portions of a reservoir through the application of horizontal drilling and hydraulic fracturing. As a result, reservoir numerical simulation of tight and ultra-tight reservoirs has become the standard tool to assess and predict production performance from these unconventional resources. Because many of these unconventional fields are immense, consisting of multistage and multiwell projects, simplification of simulation models is common both in the industry and academia. It is important to represent the results from a full-scale model by performing computations on smaller models that capture the physics while keeping the computational time manageable.

First, the most widely used simplified models are shown not to be representative of a full-scale reservoir model. These models do not account for many important factors such as fracture interference, well interference, and so forth, resulting in inaccurate rate predictions, especially when interference or boundary dominated flow take place. A novel, rigorous workflow is proposed, and compared to other literature models and to a full-scale model. Procedures, results, observations, and limitations of this workflow are then discussed. The models that result from the application of the proposed simplification

workflow can predict the fluid rates, cumulative production, and gas oil ratio with higher accuracy than popular simplified models while retaining low run times.

3.1 Background

For over five decades, numerical reservoir simulation has been one of the most important reservoir engineering tools. Simulation continues to be the best way to quantitatively describe multiple phase fluid flow behavior in highly complex, heterogeneous systems.[20] Over time, reservoir simulation has become the final hydrocarbon potential assessment tool, if not the only one, due to its incredible flexibility and success during exploitation of underground natural resources. This is why continued research efforts are made to increase the accuracy and flexibility of these simulators and to decrease the computational time required to run single or multiple studies.

Generally speaking, the process of building a reservoir model can vary depending on the objectives of a project. Reservoir models may encompass full, comprehensive fields that are built based on geological, seismic, and petrophysical interpretations. These static models are then upscaled to meet computational limits and handed over to engineers for fluid recovery optimization through well management strategies, tertiary oil recovery, and production schedule based on the current economic climate. Simulation models may also be very simple to either study particular aspects of smaller reservoirs or for research purposes where analytical expressions are validated or supported. The latter situation is very common, particularly for projects where a full reservoir simulation study is either too costly or large enough for simulation run times to be impractical. In these cases, simplified models are used both in academia and the industry.

Unfortunately, the success accrued by numerical simulation has been somewhat taken for granted, leaving space for models that do not accurately represent physical reality. This is the case for the simplified "single fracture" model which is used widely in the industry and academia.[21-27]

Recent drilling technologies in low permeability reservoirs include horizontal drilling and multistage hydraulic fracturing. Such systems are typically modeled as shown in **Figure 3.1**. Such systems are widely known to be impractical due to immense simulation run times and also the effort put forth to build such models is considerable. For this and other reasons, simplification techniques have been proposed to avoid full scale studies; such is the case of the single fracture model.

The single fracture model is a result of a concept known as Stimulated Reservoir Volume (SRV). This is the volume stimulated by hydraulic fracture half lengths, fracture height, and number of propped fractures.[28] The single fracture approach consists of a simulation model containing a single fracture draining from an allocated volume of reservoir. Typical dimensions of the model correspond to the length of the fracture and interfracture spacing as shown in **Figure 3.1**.

The advantage of this approach is the substantially low computational requirements by assuming all fractures in the field behave similarly, hence they can be represented by a single fracture. In the single fracture model, total fluid production of the entire horizontal well is trivially calculated by multiplying production from the single fracture model by the number of fractures in the well as described by equation 3.1.

$$X = n_f \, x_{Single\ fracture} \qquad 3.1$$

where, X is well fluid (oil, gas or water) flowrate or cumulative production; n_f is the number

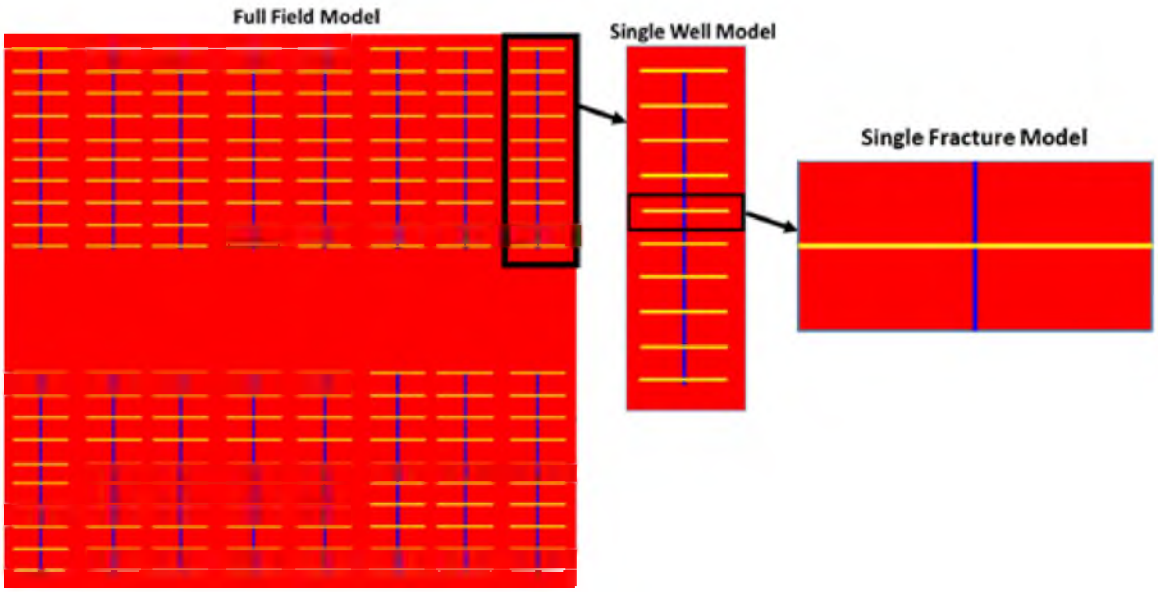

Figure 3.1 Aerial view of typical multiwell and multistage reservoir simulation model and how it may be simplified

of fractures, and $x_{single\ fracture}$ is the single fracture fluid flowrate or cumulative production. Similarly, total production for a multiwell project is calculated from the single fracture model as shown in equation 3.2.

$$X = n_w n_f x_{Single\ well\ model} \tag{3.2}$$

where n_w corresponds to the number of wells.

The problem with the single fracture model is that while it properly represents early transient flow, also called infinite-acting reservoir behavior[29], it fails as soon as boundary dominated flow takes over. Therefore, one of the objectives of this work is to establish the validity of the single fracture model and to propose a new, more accurate simulation modeling technique. This new technique retains the low simulation run times which is key to the single fracture model, while accurately accounting for fracture and well interference effects.

3.2 Workflow Components

In this workflow, an alternative to the popular single fracture model is presented. Simulation models resulting from the proper application of this new workflow should retain the single fracture's short run times while achieving a higher degree of accuracy. The primary objective of this workflow is to establish a standard in the literature in terms of full-scale simulation model simplification.

This simplification workflow standard is meant to guide and provide the simulation engineer with educated criteria in the sometimes blind mission to simplify full-scale models. The structure of the simplification workflow revolves around the consideration of fluid flow phenomena taking place in numerical simulation. The workflow is formally introduced after important fluid flow phenomena is addressed.

3.2.1 Interference Effects

As presented earlier, one of the fluid flow phenomena ignored by the single fracture model is the interference effect that result when two transient pressure fronts meet either from neighboring wells, fractures or both. As shown in **Figure 3.1**, the single fracture model is limited to dimensions corresponding to the horizontal fracture half-length and interfracture spacing. Assuming two neighboring fractures share the same operating conditions, such as flowing bottom-hole pressures and fluid rates, these two fractures are expected to reach mutual interference at some point between them. At this point, the single fracture model imposes a no-flow boundary condition, which is expected to mimic interference effects. Unfortunately, in the upcoming sections, it is shown that this representation may not be accurate enough when a single fracture model is compared to a

full-scale model.

Interference may substantially affect production from fractures and even wells depending on the operating conditions, fluid type, spacing, and diffusivity. Elliot (1951)[30] has shown the great effects of well interference on production to the point where wider well spacing was highly recommended in conventional reservoirs. Given the evidence supporting interference effects on fluid production, it is hard to neglect inter-fracture and interwell interference on simulation models, especially if operating conditions differ from fracture to fracture or well to well.

3.2.2 Boundary effects

Conditions imposed to simulation boundaries are several and serve a number of purposes. Such is the case of the constant pressure boundary condition which is applied to represent aquifers or the no-flow boundary representing nonpermeable faults or discontinuities in a reservoir. Model boundaries are always present in some form or another in any simulation model; the most common version of boundary conditions is the no-flow boundary which works by simply setting outside fluxes to zero, therefore nullifying any fluid contribution from the boundary. Under this condition, boundary dominated flow begins as a new flow regime which can be identified through production analytics.

Reservoir boundaries and their conditions not only greatly affect hydrocarbon flow, but also delineate a reservoir's original hydrocarbon in place. This is yet another disadvantage of the single fracture model that accounts for the volume stimulated only by internal fractures. External fractures, which are the first and last fractures in a horizontal well, have greater hydrocarbon potential depending on reservoir boundaries as shown in **Figure 3.2**.

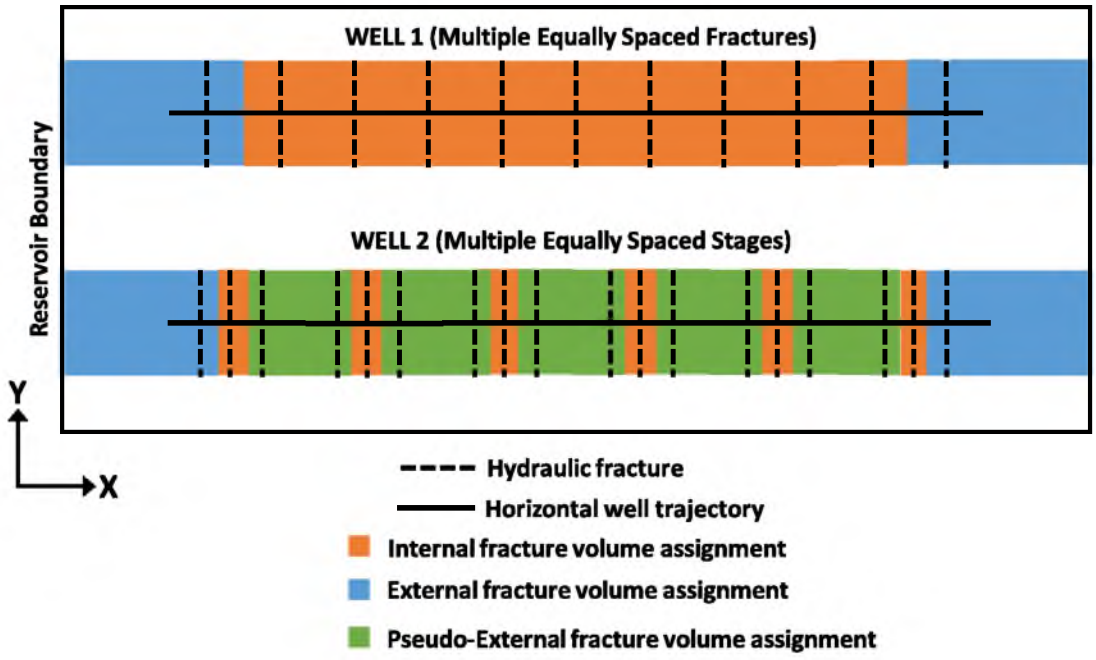

Figure 3.2 Types of internal and external fractures and their corresponding volume assignments (top view)

3.2.3 Multiple Hydraulic Fracture Representation

Hydraulic fracture creation and propagation are challenging topics of research in geomechanics which force stimulation and simulation engineers to work with what is available. Microseismic fracture mapping is the closest the oil and gas industry has come to imaging hydraulic fracture shape; however, this method does not account for fracture closure after treatment and may overestimate the contact area between the reservoir and the well. For most practical applications, geophysicists and engineers agree with an adequate fracture half-length and height for a rectangular shaped fracture to be used in numerical simulation.

Under the assumptions made about hydraulic fractures' dimensions, fracture generalization in horizontal wells is widely practiced in the literature. If the injection

operating conditions are identical for all fractures in a given horizontal well, it is believed that all fractures will possess similar dimensions and rock-flow properties. This has generated the assumptions that all fractures are identical and will behave similarly as stated in most analytical and numerical research works by both the industry and academia.

Multiple hydraulic fracture representation through a single fracture is one of the most important assumptions in computer modeling of simplified hydraulically fractured reservoirs. In this workflow, this concept is also used, but instead of a single fracture generalization, two or even more generalizations can be made. In summary, these generalizations come in the form of internal fractures and external fractures. Types of internal and external fractures can be easily identified as shown in **Figure 3.2**. In this work, the fluid flow behavior and contribution to production from internal and external fractures are taken into account to achieve more accurate results.

3.2.4 Other Simulation Phenomena

There are other important components that should be considered when making decisions about a computer simulation model. Most simulation phenomena such as reservoir boundary conditions and interference effects that influence fluid flow may be common while others may not show up as often, such as vertical gridding (gravity segregation), grid geometry, natural and hydraulic fractures, property heterogeneity, and special well completions, among others. Because the objective of this paper is to establish a generalized workflow rather than presenting every possible fluid flow mechanics applicable to particular models, only a word of caution is presented here. Engineering judgement, dimensionless analysis, and even a trial and error analysis may suggest whether

a particular simulation phenomenon should be neglected or not.

In the following sections, application of the aforementioned simulation phenomena is discussed. The core of this simplification workflow revolves around fluid flow phenomena and the use of symmetry to come up with a simplified simulation model truly representative of a full-scale model. Other simulation phenomena not specifically discussed here should be included in the particular workflow used to build these particular models.

3.2.5 Symmetry Application

As mentioned earlier, the single fracture model relies on the assumptions that all fractures propped in a horizontal well and under the same operating conditions behave identically. Therefore, as shown in equations 3.1 and 3.2, the behavior of a single well is represented by multiplying the results from a single fracture model by the number of fractures in the well. This application of symmetry, however, does not capture important fluid flow phenomena that was discussed in the previous sections.

Models can significantly benefit from any symmetrical behavior as long as all contributing fluid flow phenomena is captured. A simplified simulation model is a small, representative piece of a full-scale simulation model that captures all significant physical and chemical phenomena, thus decreasing required run times while remaining reasonably accurate. Under this definition, the modeler must focus on all contributing forces to fluid flow if a simplified system is to be built. In the following section, the proposed simplification workflow is introduced where important fluid flow components are revisited and combined with a symmetry application that results in a reliable simplified model.

3.3 Proposed Simplification Workflow

The solution to most numerical simulation models is dependent on the contribution of various physical forces and fluid flow phenomena. Some of these factors may be deemed negligible for practical reasons and excluded from the simulation altogether. A simple example of how these factors combine to reach a solution for a specific problem is shown in **Figure 3.3**.

After all significant factors have been identified for a particular project as depicted in **Figure 3.3**, the simplification process may begin. As mentioned in the previous section, one of the many assumptions made in the literature is the multiple hydraulic fracture representation which states that all hydraulic fractures propped under similar operating conditions behave similarly. Hence, a single (or multiple) representative fracture is enough for numerical and analytical solutions which means that the "Fracture variation" component of the solution process in **Figure 3.3** may be crossed out. Similarly, other contributing factors may be crossed out based upon assumptions or previous analysis. Once a solution process is built and simplified, the concept of symmetry is applied by capturing all remaining factors. This is explained more thoroughly in the upcoming examples.

Lastly, results from the simplified model must be modified to represent full-scale simulation. Equations that make these conversions are intuitive as in the case of the single fracture model. However, as models grow in complexity, these equations may become less obvious. Equation 3.3 is designed to help keep track of important elements in simple and complex simulation models.

$$X = \sum_{i=1}^{e} S_i k_i x_i \tag{3.3}$$

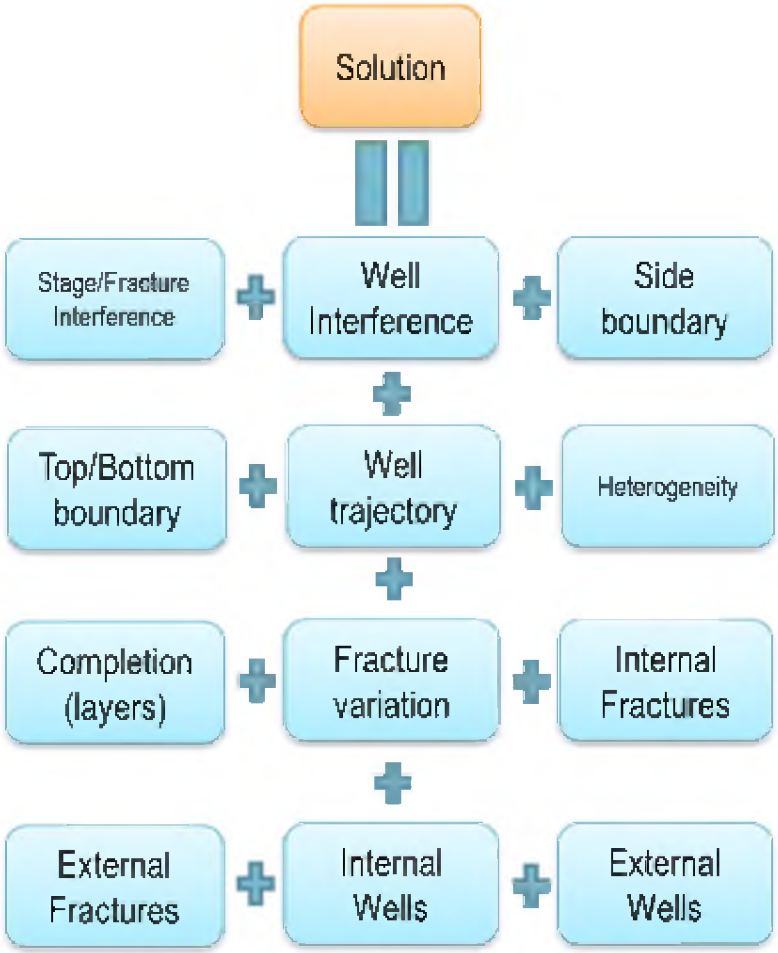

Figure 3.3 Example of a solution process diagram that shows various force contributions to flow in a simple hydraulically fractured reservoir.

where e is the number of elements; s_i is the symmetric factor for the ith element; k is the multiplier factor for full model representation and x_i is the cumulative production or production rate from the ith element. The application of this equation is shown in the next section.

The simplification workflow steps can be summarized as follows:

1. Build a solution process diagram by accounting for all present phenomena in the system.

2. Simplify the solution process diagram by crossing out negligible factors based on assumptions or previous analysis.
3. Prepare a unit model representative of a full-scale model by applying symmetry and accounting for all remaining factors in step 2.
4. Transform simplified results to full-scale results by applying equation 3.3.

3.4 Case Examples

3.4.1 Single Well Case

In this instance, the single fracture model and a model prepared after application of the simplification workflow are compared to a full-scale, black-oil, single horizontal well model. To give some context of the problem at hand, the full-scale model is shown in **Figure 3.4** with basic model properties as described in **Table 3.1**.

The single fracture version of the full-scale model shown in **Figure 3.4** consists of a model with no-flow boundaries at the fractures edges and half interfracture spacing as shown (bounded by red dashed lines) in **Figure 3.5**.

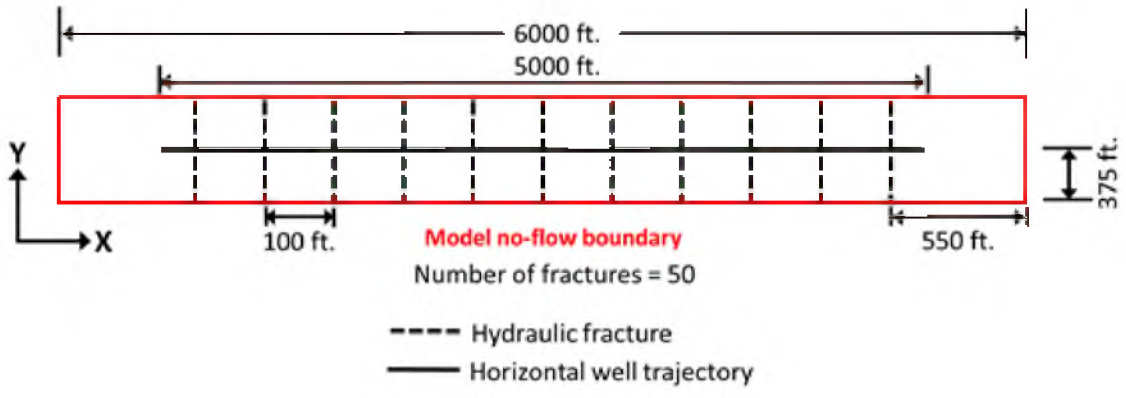

Figure 3.4 Horizontal well with 50 equally spaced fractures

Table 3.1 Summary of reservoir model and operational parameters

Reservoir Top (ft):	9600
Matrix Permeability, kx, ky, (nD):	50, 100, 500, 1000
Matrix Permeability, kz (nD):	0.1 * kx
Fracture Orientation	YZ plane
Number of Fractures	50
Initial Reservoir Pressure (psia):	4500
Rock Compressibility (1/psia) @5000 (psia)	$4X10^{-6}$
Initial HC Saturation (%):	84 (Single phase)
Reservoir Porosity (%):	8
Flowing Bottom hole Pressure (psi):	500
Bubble Point Pressure (psia)	1965
Oil Gravity (API)	52
Reservoir Temperature (^{O}F)	245

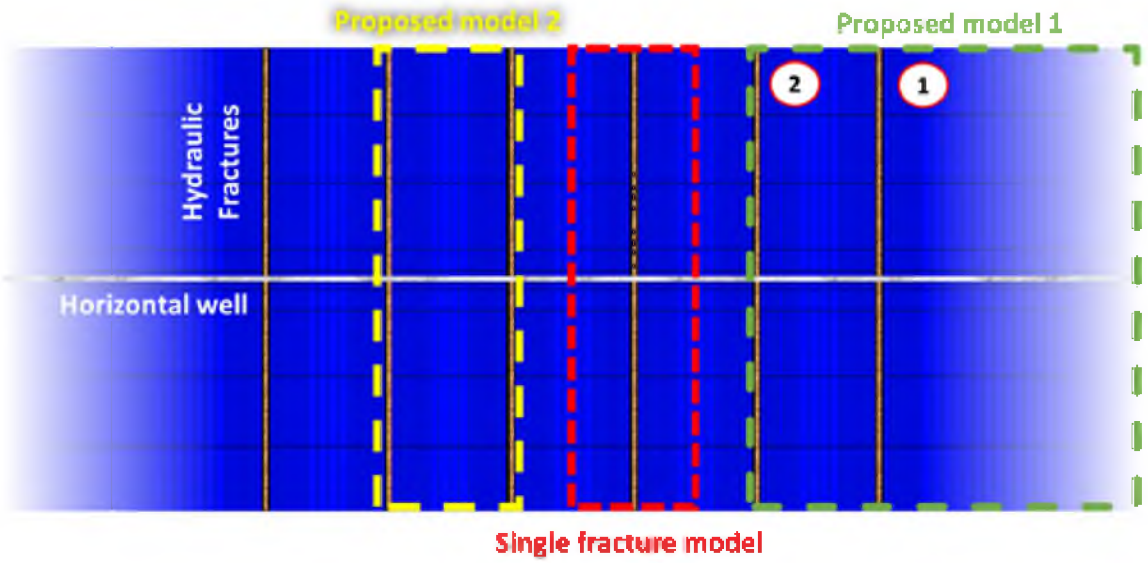

Figure 3.5 Aerial view of a full-scale horizontal well and its simplification approaches as presented by the single fracture and proposed models. Dashed lines represent no-flow boundaries for each model.

From this model, it is straightforward to capture fracture interference through reservoir boundaries located exactly halfway between two neighboring fractures. By application of equations 3.1 and 3.2, the results of this model are modified in an attempt to represent a full-fledged horizontal well model. Note that the single fracture and the proposed models simulate only a portion of the full model.

On the other hand, application of the proposed simplification workflow by following the steps described in the previous section results in a different model. Firstly, important phenomena, albeit not all (for the purpose of simplicity), are shown in **Figure 3.3**.

Secondly, factors in the solution process diagram are crossed out on the basis of the model driving forces. Because this model is homogenous, with identical fractures spaced equally from one another and consists of a single well, components such as interwell interference, heterogeneity, and so forth can be crossed out. If the model is thin enough

and/or gravity segregation is deemed negligible based on previous analysis, layering and layer-based completions can also be neglected under this basis. The final version of the solution process diagram is shown in **Figure 3.6** (a).

Lastly, the model is built based upon the solution process and symmetry application. According to **Figure 3.6** (a), fracture interference needs to be included in the reservoir simulation as well as contribution from external and internal fractures. Clearly, under these requirements, the single fracture model is insufficient and a new model is necessary. Based on the model requirements and taking advantage of symmetry, "Proposed model 1" is built as shown in **Figure 3.5**.

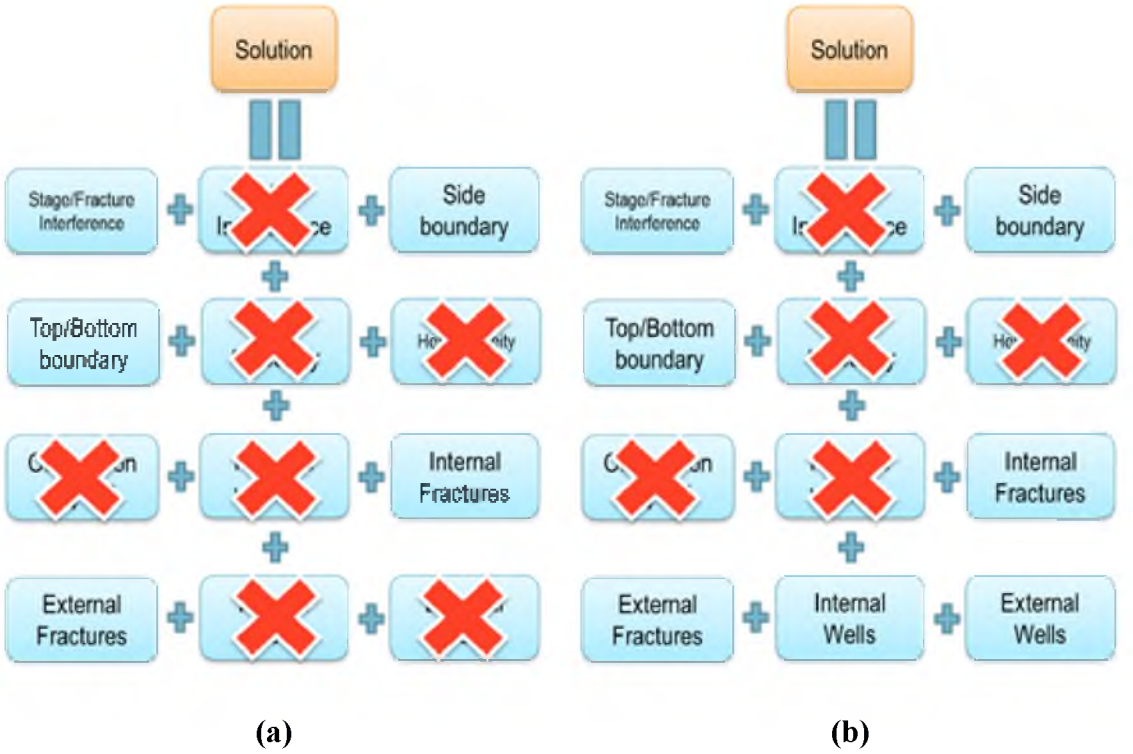

(a) **(b)**

Figure 3.6 Solution process diagram simplification for a single well model (a) and multi-well model (b)

As presented in "Proposed model 1", there is a fracture located at the far left of the model and another one located at the right at a regular fracture spacing distance. The left fracture is representative of interior fracture behavior while the right fracture represents exterior fracture behavior as required by the solution process diagram in **Figure 3.6** (a).

With this model, all the requirements in the solution process diagram are satisfied such as fracture interference and interior and exterior fracture behavior. Contrary to the single fracture model, this proposed model, result of the application of a new standardized simplification workflow, consists of two fractures.

"Proposed model 2" is the result of the same solution process diagram shown in **Figure 3.6 (a)** if the "External fractures" component were also crossed out. Because several horizontal wells consist of a substantial number of hydraulic fractures, it may be feasible to ignore the contribution of external fractures to flow without sacrificing much accuracy. "Proposed model 2" also consists of two fractures at each side of the model, both serving the purpose of capturing the interference effect of internal fractures.

Results of these three models (full-scale model, single fracture model, and proposed model 1 are discussed in the Results section. It is important to note that while results of the full-scale model are readily available, results from the simplification approaches need to be calculated either using equations 3.1, 3.2, or 3.3. The application of these equations is discussed as well for clarity.

3.4.2 Multiwell and Multifracture Case

Similarly to the single well case, other more complex cases can be explored with this new simplification workflow. As a more thorough example, a three horizontal well model

is considered for simplification this time. Fluid as well as rock properties are found in **Table 2.1** and the model schematics can be found in **Figure 3.7**.

For the purpose of this example, the solution process diagram for the single well case shown in **Figure 3.3** will be also used for this instance. After all important driving forces are taken into consideration and the solution diagram is simplified, the resulting diagram is shown in **Figure 3.6 (b)**. Similarly to the single well case, a model is built by taking into consideration fracture interference effects as well as interwell interference. The resulting model is shown in **Figure 3.8**.

As shown in the simplification schematics, the single fracture model does not change substantially while the proposed model adapts to capture well interference. Fractures elements are labeled as 1, 2, 3, and 4 which represent external fractures in external wells,

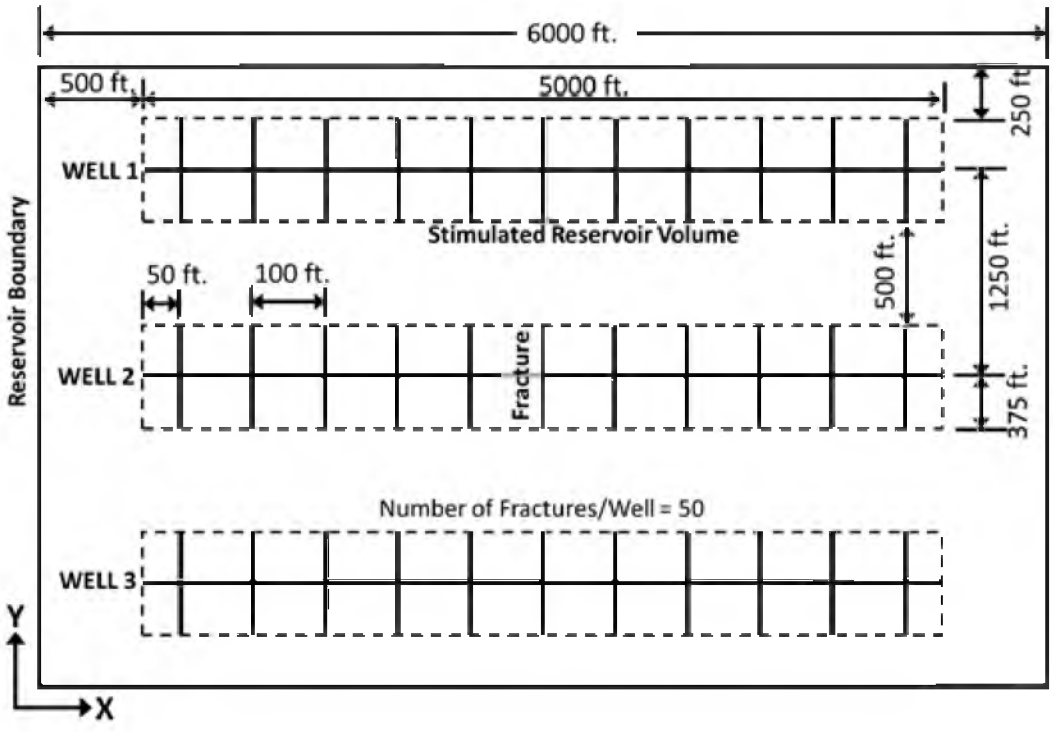

Figure 3.7 Full-scale multiwell simulation model schematic

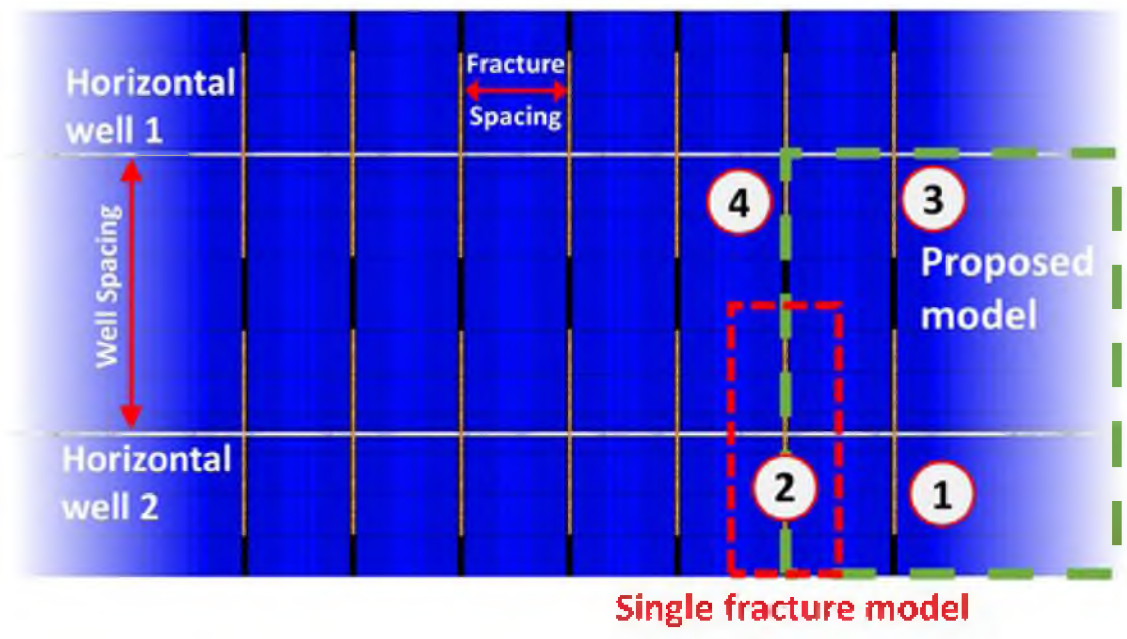

Figure 3.8 Aerial view of a full-scale multi-well model and its simplification approaches as presented by the single fracture and proposed models. Dashed lines represent no-flow boundaries for each model.

internal fractures in external wells, external fractures in internal wells, and internal fractures in internal wells, respectively. In order to clarify the objective of these fracture elements, one must consider the fluid flow contributions made by internal and external fractures in the single well case. By applying this concept to wells, the concept of internal and external wells is born. Hence, by application of symmetry, the proposed model is shown in **Figure 3.8** and satisfies all components of its corresponding simplified solution process diagram.

Note, that the proposed model only takes into account half a fracture for the internal well, and a full fracture of the external well. This was done with the purpose of capturing boundary effects as soon as external wells perceive them and to capture interference between wells and fractures while applying symmetry.

3.5 Results

3.5.1 Single Well Case

After all three reservoir models (simplified single fracture, proposed simplified model 1, and a single well full-scale model) were run, the final step of the simplification process consists of scaling results. As mentioned before, the single fracture results are modified trivially as shown in equations 3.1 and 3.2. On the other hand, results modification from the "Proposed model 1" is not as obvious. Knowing that the number of fracture elements in "Proposed model 1" as shown in **Figure 3.5** is 2, equation 3.3 becomes:

$$X = S_1 k_1 x_1 + S_2 k_2 x_2 \qquad 3.4$$

Taking into consideration the fracture element labels 1 and 2 in **Figure 3.5**, **Table 3.2** lists value assignments for variables in equation 3.4.

Upon inspection of **Figure 3.5**, the symmetric factor for element 1 is 1 because the entire fracture element is modeled by the simplified model. Similarly, the symmetric factor for fracture element 2 is 2 because only half of the fracture behavior is considered in the simplified model.

The multiplier factor represents the number of elements present in the full-scale model. Since element 1 represents external fractures, its multiplier factor is 2. Fracture element 2 represents internal fractures, hence its corresponding multiplier factor is the total number of fractures minus 2.

Upon value substitution of equation 3.4 based on **Table 3.2**, equations 3.5 and 3.6 are used to determine modified oil rates and oil cumulative production, respectively.

$$q_{oil} = 2q_{1,oil} + 2q_{2,oil}(\mathrm{n}_f - 2) \qquad 3.5$$

$$N_p = 2N_{1,p} + 2N_{2,p}(\mathrm{n}_f - 2) \qquad 3.6$$

Table 3.2 Symmetric and multiplier factors for elements 1 and 2 for the "Proposed model 1"

	1	**2**
S	*1*	*2*
K	*2*	n_f-*2*

Equation 3.7 shows typical cumulative gas oil ratio calculation according to data from **Table 3.2**.

$$GOR = \frac{N_{gas}}{N_{oil}} = \frac{N_{1,gas} + N_{2,gas}(n_f - 2)}{N_{1,oil} + N_{2,oil}(n_f - 2)} \quad 3.7$$

Four cases for each model (single well full-scale model, single fracture model, and "Proposed model 1") were run with horizontal permeabilities varying from 50 nD to 1000 nD. Based on the above equations and the results obtained by numerical simulation, oil rates, cumulative production, and cumulative GOR were calculated and compared as shown in **Figure 3.9** and **Figure 3.10**.

As observed in **Figure 3.9**, cumulative oil production for all cases is almost identical for an initial period of time because during transient flow, fracture interference is not experienced in any model.

However, as soon as boundary dominated flow and/or interference effects take place, there is a substantial difference between the full-scale model and the single fracture model. Since the proposed model does account for exterior fracture and interior fracture interference effects, it matches almost perfectly with the full-scale model. A similar situation is observed in oil rates as seen in **Figure 3.10** where the quality of results from the single fracture model is even less relatable to the full-scale model.

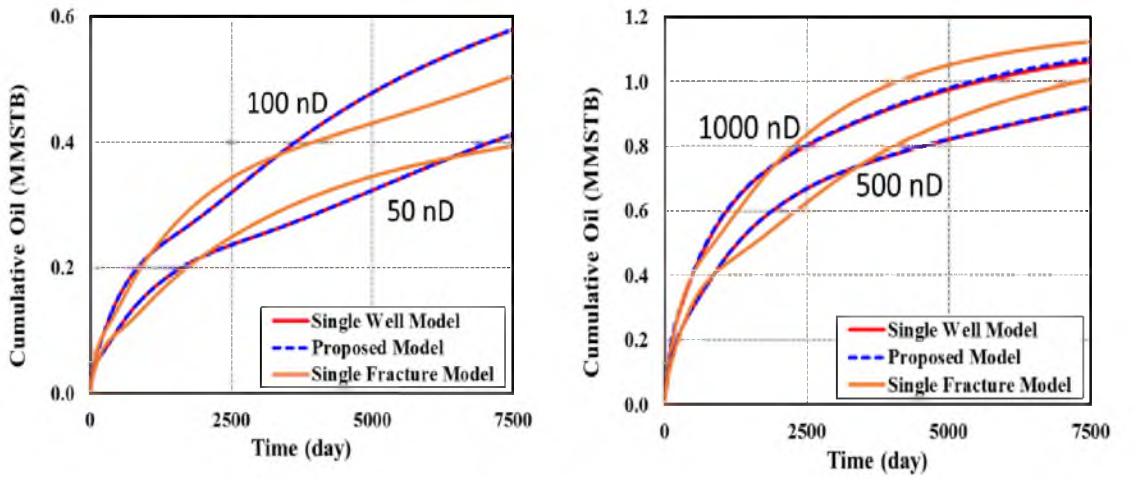

(a) **(b)**

Figure 3.9 Cumulative oil comparison for 50nD and 100 nD (a) 500nD and 1000 nD (b)

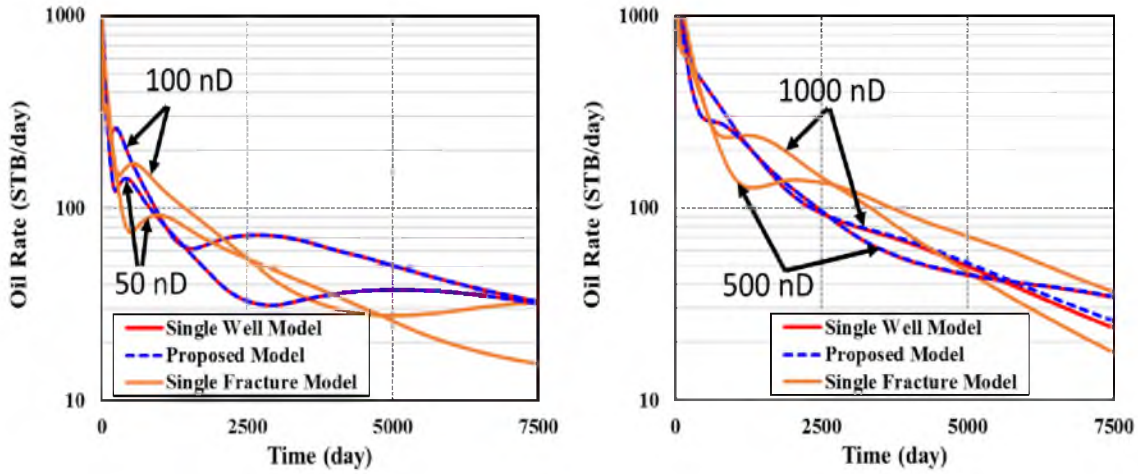

(a) **(b)**

Figure 3.10 Oil rate comparison for 50nD and 100 nD (a) 500nD and 1000 nD (b)

One interesting feature observed for models considering internal and external fracture behavior is shown in **Figure 3.11**. Cumulative GOR for both fracture cases show upper and lower bounds which encapsulate the cumulative GOR behavior of the entire model. In other words, when the contribution of internal fracture is more significant than that of the external fractures, the entire model will show a GOR behavior close to the external fracture (lower bound). Similarly, when the contribution of external fractures is more significant, the entire model shows a GOR behavior closer to the internal fracture (upper bound) behavior. Hence, it is concluded that the full-scale GOR behavior cannot be higher than the internal fracture GOR or lower than external GOR behavior regardless of the number of fractures. This is proven as shown in **Figure 3.12**.

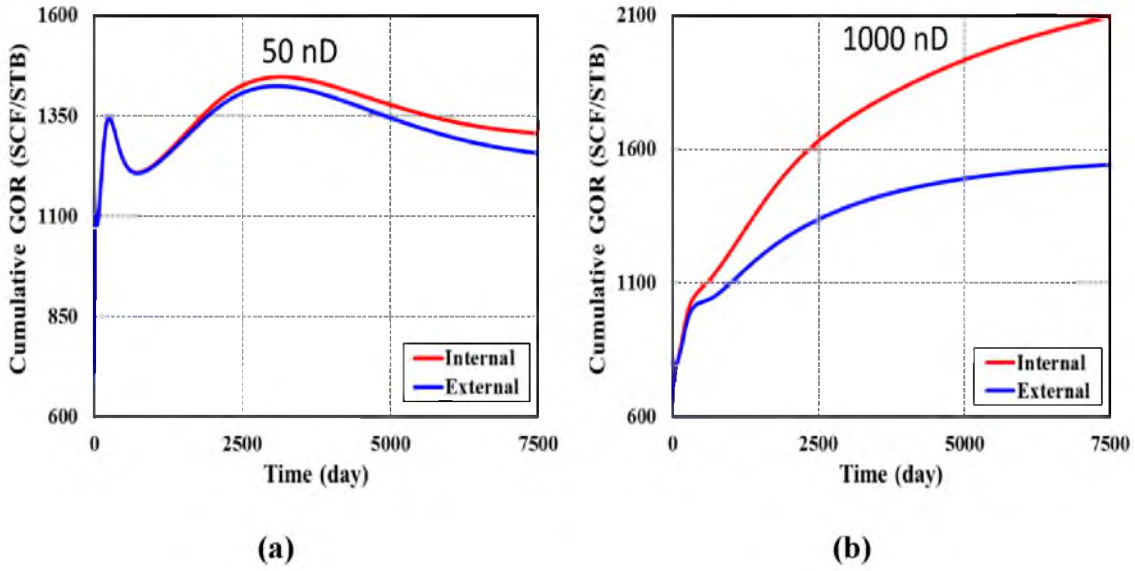

Figure 3.11 Internal and external fracture cumulative GOR comparison for a 50 nD case (a) and a 1000 nD case (b)

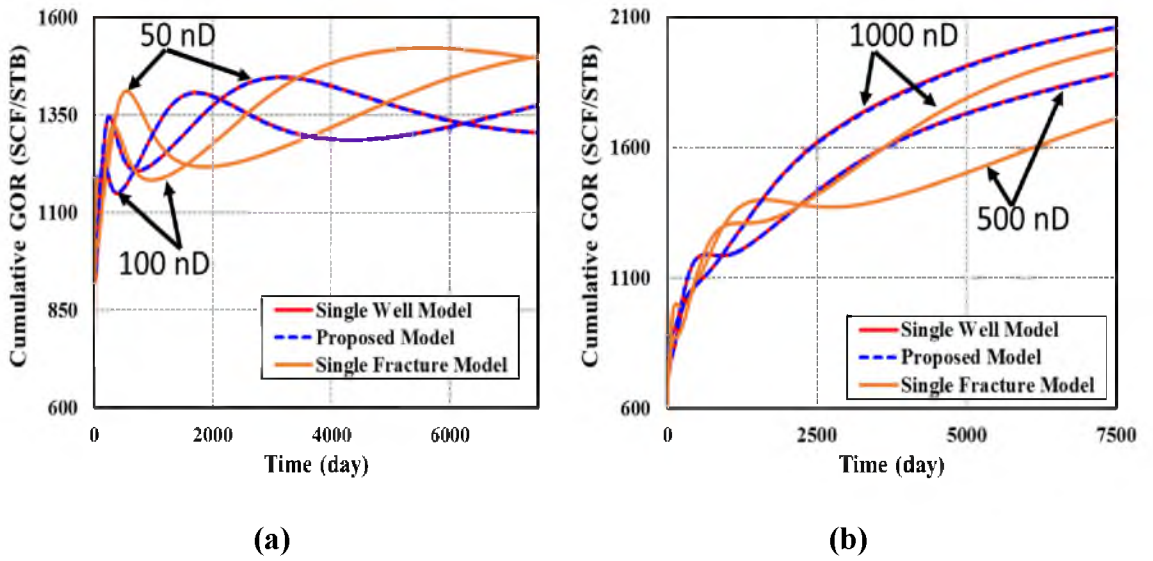

Figure 3.12 Cumulative GOR comparison for 50nD and 100 nD (a) 500nD and 1000 nD (b)

The qualitative difference between the full-scale model or the proposed model and the single fracture model are obvious from these results. A more quantitative approach was also applied to help determine the effectiveness of the proposed model which is product of the simplification workflow presented. **Table 3.3** shows calculated Average Absolute Relative Error (AARE) and Normalized Root Mean Square Error (NRMSE) of both simplified models results when compared to full-scale results.

The highest error calculated for the proposed model is about 2% for the GOR in the 50 nanodarcy case, whereas the highest error for the single fracture model is almost 100% for the single fracture case. It is again shown that error accrued by the single fracture model can be quite substantial.

Table 3.4 shows run times for all three models proving that the new models retain valuable short times without sacrificing accuracy.

Table 3.3 Comparison of simplified models to a full-scale model through statistical analysis for the single well case

	Reservoir Permeability (nD)	Proposed Model		Single Fracture Model	
		NRMSE (%)	AARE (%)	NRMSE (%)	AARE (%)
Oil Rate	50	0.28	3.72	11.95	98.25
	100	0.00	0.06	12.49	98.01
	500	0.52	2.79	17.43	97.96
	1000	0.01	0.58	1.00	10.46
Cumulative Oil	50	0.08	1.33	3.46	5.02
	100	0.03	0.03	4.34	4.73
	500	0.17	1.44	3.96	3.84
	1000	0.20	0.08	2.73	2.98
Cumulative GOR	50	2.25	1.03	15.43	7.32
	100	0.77	0.90	6.25	5.83
	500	1.14	0.83	7.63	4.31
	1000	1.67	2.14	4.32	2.68

Table 3.4 Run time comparison for different models for the single well case

Reservoir Permeability (nD)	Run Time (Minutes)		
	Single Fracture Model	Proposed Model	Full-Scale Model
50	1.6	1.6	17.9
100	1.4	1.5	17.8
500	1.4	1.5	17.9
1000	1.4	1.4	19.7

3.5.2 Multiwell and Multifracture Case

Another advantage of this new technique is that it can be applied to well spacing. Well and fracture spacing studies are very important when it comes to oil production optimization. An accurate and simple simulation model is crucial to conduct timely studies. Even though full-scale reservoir models are desirable for the most accurate description of fluid flow behavior, multiwell fields are usually handled separately without considering well and fracture interference.

The single fracture model's results from the last section can be used to calculate results for three wells. This is not the case for the proposed model which accounts for more fracture elements representing different components that contribute to fluid flow. Similarly to the previous section, symmetric and multiplier factors are determined using fracture elements as labeled in **Figure 3.8** and shown in **Table 3.5**.

Applying equation 3.3 to this case, the oil rate expression becomes:

$$q_{oil} = 4q_{1,oil} + 4(\mathrm{n}_f - 2)q_{2,oil} + 4(n_w - 2)q_{3,oil} + 4(\mathrm{n}_f - 2)(n_w - 2)q_{4,oil} \qquad 3.8$$

Table 3.5 Symmetric and multiplier factors for a multiple horizontal well case

	1	2	3	4
S	*1*	*2*	*2*	*4*
K	*4*	*2(nf-2)*	*2(nw-2)*	*(nf-2)(nw-2)*

Results comparison were made in the same fashion as the single well case as shown below. Cumulative oil production, oil rates, and cumulative GOR are shown in **Figure 3.13**, **Figure 3.14**, and **Figure 3.15**, respectively.

Even though the error in the proposed model is slightly higher than the single well case, it is still significantly lower than the single fracture approach as shown qualitatively by plots and quantitatively in **Table 3.6**. Computational run times were also determined for each case as shown in **Table 3.7**.

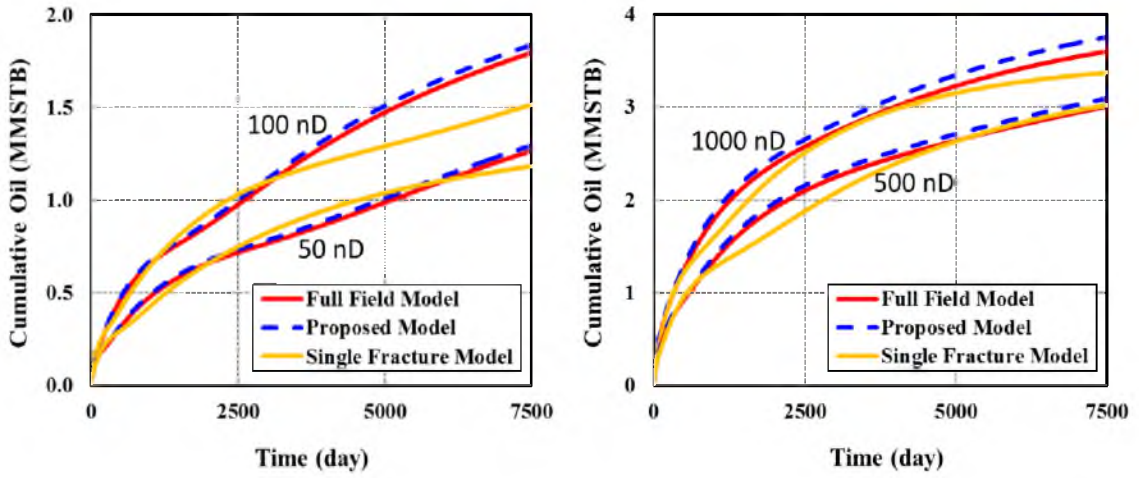

a) **b)**

Figure 3.13 Cumulative oil production comparison for 50nD and 100 nD (a) 500nD and 1000 nD (b)

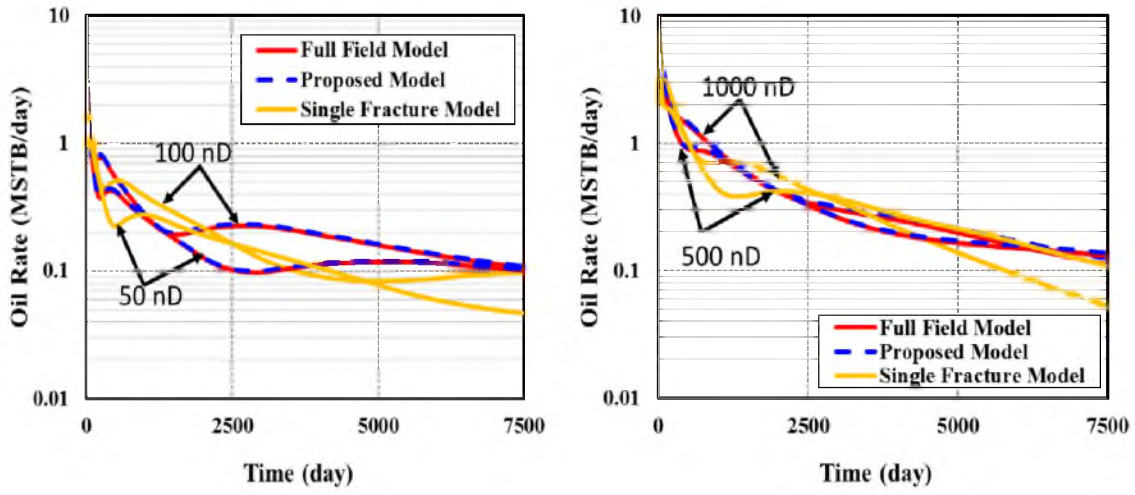

(a) **(b)**

Figure 3.14 Oil rate comparison for 50nD and 100 nD (a) 500nD and 1000 nD (b)

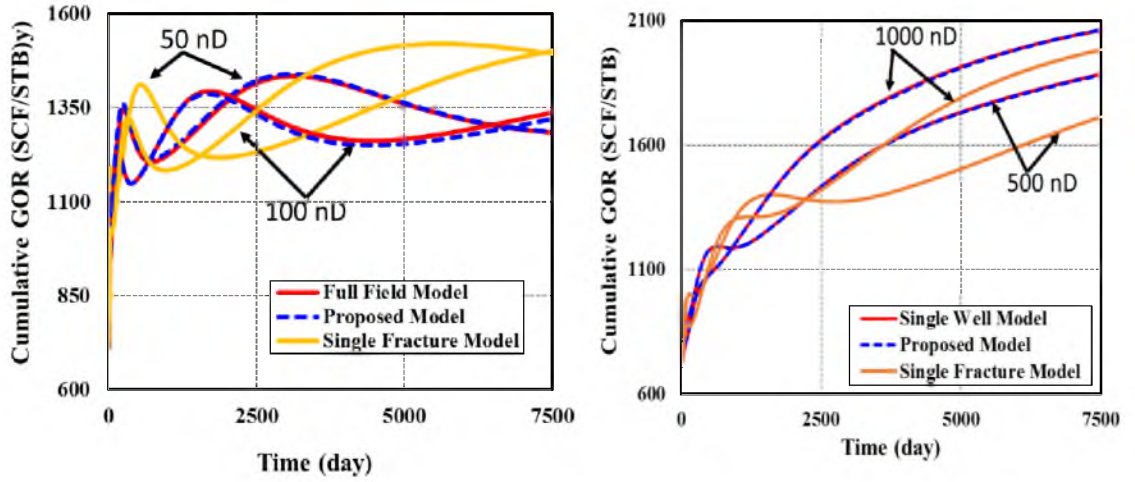

a) **b)**

Figure 3.15 Cumulative GOR comparison for 50nD and 100 nD (a) 500nD and 1000 nD (b)

Table 3.6 Comparison of simplified models to a full-scale model through statistical analysis for the multiwell case

	Reservoir Permeability (nD)	Proposed Model		Single Fracture Model	
		NRMSE (%)	AARE (%)	NRMSE (%)	AARE (%)
Oil Rate	50	2.48	2.95	2.18	21.43
	100	2.60	2.94	0.78	18.97
	500	3.11	4.69	0.95	14.40
	1000	3.37	6.96	0.98	16.89
Cumulative Oil	50	0.92	3.85	3.74	4.86
	100	0.99	4.27	5.39	5.27
	500	1.32	5.55	1.71	2.26
	1000	1.95	6.49	3.09	3.17
Cumulative GOR	50	3.57	2.08	15.35	6.76
	100	2.80	1.94	13.01	6.01
	500	2.15	2.46	4.66	2.75
	1000	1.67	2.14	4.32	2.68

Table 3.7 Run time comparison for different models for the multiwell case

Reservoir Permeability (nD)	Run Time (Minutes)		
	Single Fracture Model	Proposed Model	Full-Scale Model
50	1.6	2.7	81.3
100	1.4	2.7	77.7
500	1.4	2.4	74.7
1000	1.4	2.5	73.1

Again, it is shown that models resulting from the application of the proposed simplification workflow are reliably accurate and save valuable project time. Similarly, more complex systems can also be simplified by application of the present simplification workflow by accounting representative fracture elements and applying equation 3.3. This workflow is particularly helpful for well spacing optimization studies where modeling time and computational run times are impractical for full-scale models.

3.6 Fracture and Well Spacing Application

One clear application of the simplification workflow is the study of well and fracture spacing. Several studies have addressed hydraulic fracture spacing with the aim to optimize profitability of hydrocarbon production. The fact that increased oil production is not directly proportional to the added number of wells due the drainage interference of wells is well recognized from the early research on vertical well spacing in conventional reservoirs.[31-34]

Zuber et al. (1995)[35] and Baker et al. (2012)[36] presented well and fracture spacing studies where simulation and economic analyses were conducted for natural gas coalbeds. Meehan (1995)[37] conducted simulation studies to identify optimal fracture treatment designs and well spacing configurations for heterogeneous reservoirs. Meyer et al. (2010)[38] presented approximate analytical production solutions for multiple patterned transverse hydraulic fractures where they looked at Net Present Values (NPV) as a function of number of fractures and propped fracture lengths. Hards et al. (2013)[39] used a fully compositional simulation to optimize fracture design, fracture spacing, and well spacing for the Cardium formation. Jin et al. (2013)[40] estimated ultimate recovery based on correlations developed using fracture parameters to optimize fracture spacing in oil reservoirs. Eburi et al. (2014)[41] looked at well interference effect on estimated ultimate recovery to seek optimum well spacing in liquid rich shale plays.

Several studies were conducted to optimize well spacing configurations based on NPV in various fields such as the Eagle Ford[42,43] and the Bakken.[44] Integrity of well spacing with fracture half-length and number of fractures was studied in tight gas reservoirs.[45,46,47] Mechanical properties in reservoir such as in-situ stress were considered in fracture spacing optimization[48,49] by maximizing the fracture network between hydraulic fracture and natural fractures.[50] Optimum fracture spacing of 200 ft. was found in gas-condensate reservoirs considering the Knudson flow through micropores.[51] Fewer wells were drilled in liquid lean reservoir compared to liquid rich reservoir as shown in the simulation study on the effect of fluid compositions on well spacing for fixed hydraulic fracture geometry.[52] Besides the deterministic approach using simulations, stochastic methods are also popular using empirical relationships such as decline curve analysis to study well spacing

optimization in oil reservoirs.[53,54]

In this section, a brief application of the simplification workflow is presented. After the workflow is applied, a resulting simplified model that represents a typical multiwell and multistage configuration is used for simulation and a brief spacing economic analysis is performed. The strengths of the workflow are shown in the form of accurate results and low simulation times for several simulation case studies where an economic assessment can be made quickly and accurately.

For this case study, a 640 acre section is considered with fluid properties and operating conditions shown in **Table 3.8**. Fracture propped lengths are constant as they are not considered for this study. The two main variables for the simulation models are fracture spacing and well spacing. Due to geometrical considerations, fracture spacings of 40, 60, 120, 176, and 240 feet are considered. The number of wells in this scope are set to 1, 2, 4, 6, and 8.

As shown in example 3.4.2, a multistage and multiwell system can be represented by 4 elements. Spacing between these 4 elements determines fracture and well spacing as can be seen in **Figure 3.8**. One set of simulations were run with all spacing combinations and a matrix permeability of 50nD. Two more sets were performed matrix permeabilities of 500 and 1000nD totaling 75 unique simulation cases.

After simulations were run, results processing was done by application of equation 3.8 with symmetric and multiplier factors values from **Table 3.5**. It was clear that recovery factors are proportional to the number of fractures and number of wells. Hence, an economic analysis was carried out to determine the optimal configuration for this specific case.

Table 3.8 Spacing study reservoir simulation data

Reservoir Top (ft):	12100
Matrix Permeability, kx, ky, (nD):	50, 500, 1000
Fracture half-length (ft):	305
Matrix Permeability, kz (nD):	0.1 * kx
Initial Reservoir Pressure (psia):	4500
Rock Compressibility (1/psia) @5000 (psia)	$4X10^{-6}$
Initial HC Saturation (%):	84 (Single phase)
Reservoir Porosity (%):	8
Flowing Bottom hole Pressure (psi):	500
Bubble Point Pressure (psia)	1965
Oil Gravity (API)	52

After 30 years of production, Net Present Values (NPV) for all 75 cases were calculated using capital and operating cost information found in **Table 3.9**. Surface functions of well and fracture spacing are plotted. Ideally, the optimum NPV is found at the maxima of the surface by numerical calculation of:

$$\frac{\partial \mathrm{NPV}(n_w, n_f)}{\partial n_w} = 0 \;\; ; \;\; \frac{\partial \mathrm{NPV}(n_w, n_f)}{\partial n_f} = 0 \qquad 3.9$$

As shown by **Figure 3.16**, **Figure 3.17**, and **Figure 3.18**, net present values for this study were found to be indirectly proportional to fracture and well spacing for most cases.

Table 3.9 Economic analysis capital and operating costs

Land acquisition ($/acre):	2,500
Permitting ($):	2,700
Site Construction ($):	400,000
Horizontal drilling cost ($/ft):	450
Vertical drilling cost ($/ft);	200
Cost per fracture ($/nɛ):	350,000
Completion ($/well):	200,000
Production to gathering station ($/well):	450,000
Royalty (%):	15
Discount Rate (%):	10
Depth, (ft):	12,100
Lateral length, (ft):	5,280
Oil Price ($/STB):	50
Gas Price ($/MSCF):	2.8
Monthly operating cost ($/well):	5,000

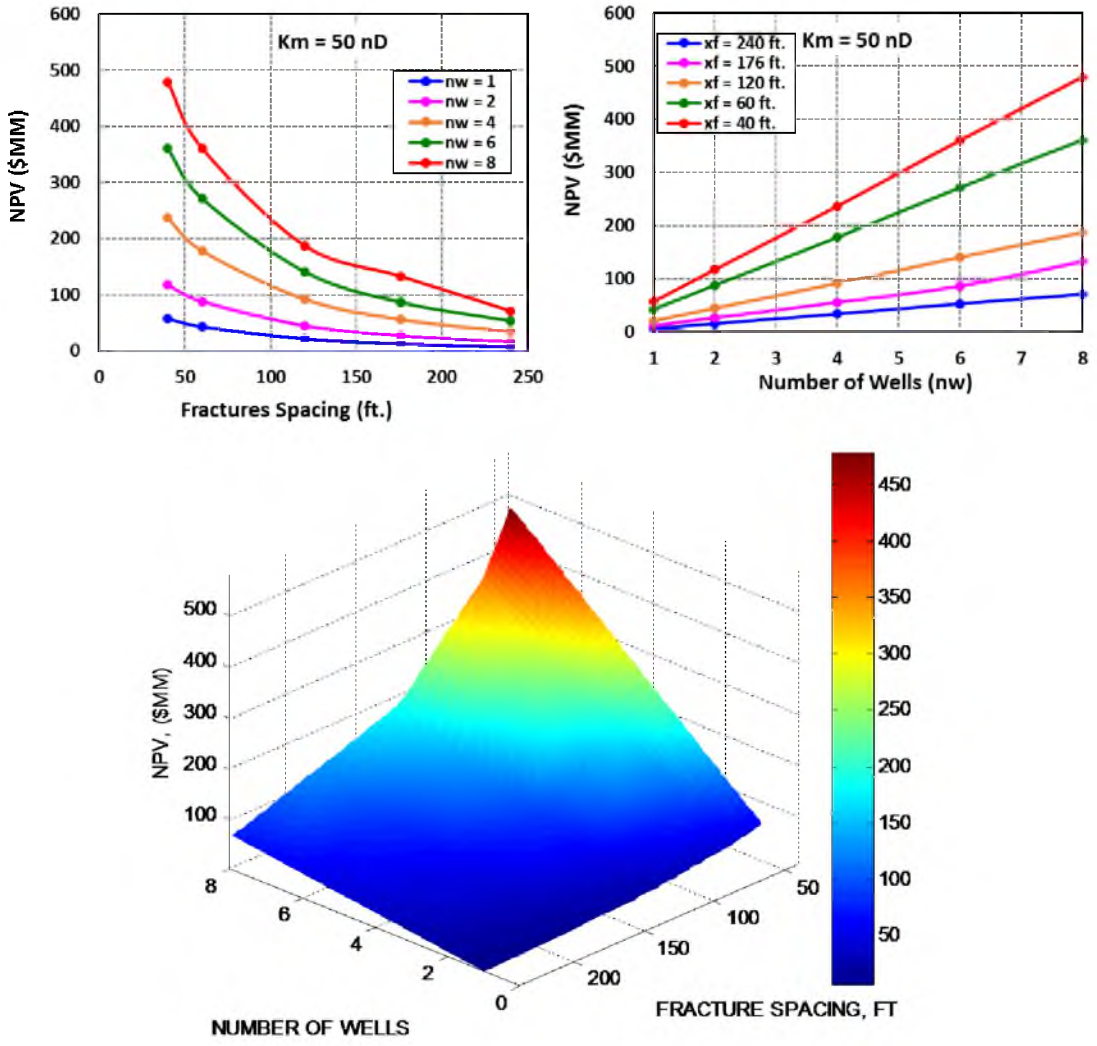

Figure 3.16 Net present value for a 50 nD matrix permeability spacing study

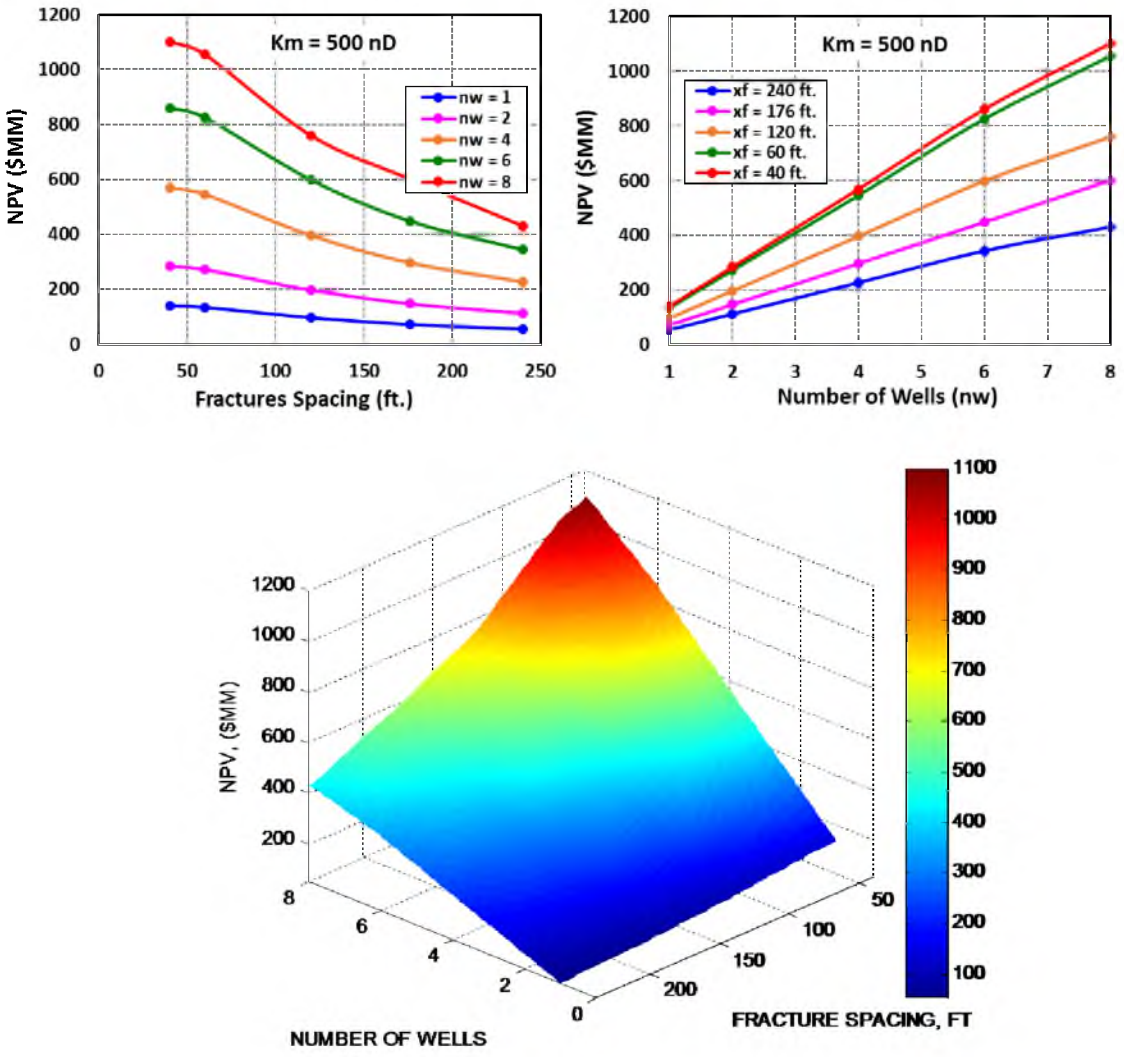

Figure 3.17 Net present value for a 500 nD matrix permeability spacing study

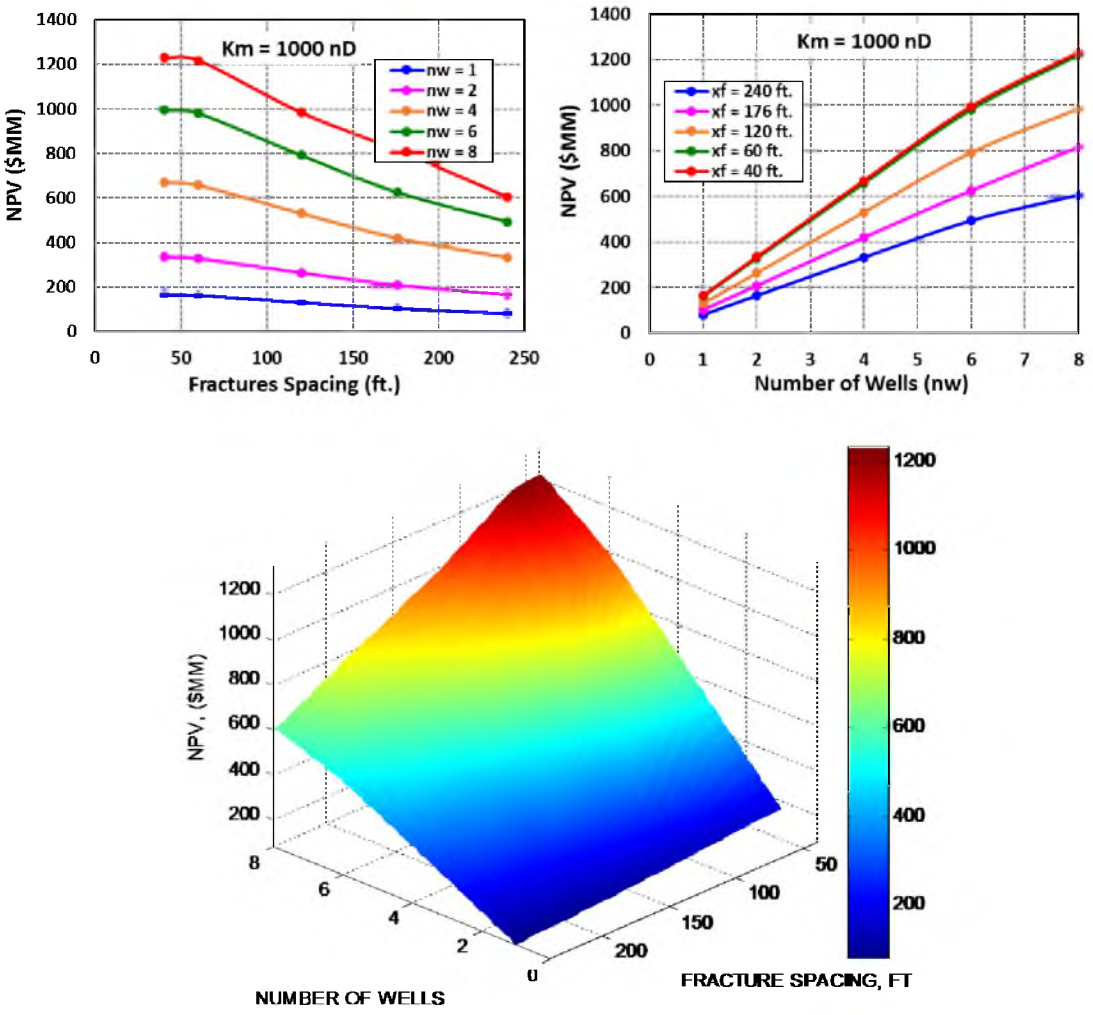

Figure 3.18 Net present value for a 1000 nD matrix permeability spacing study

The most important finding is the definite impact of matrix permeability to fracture and well spacing. The relationship between NPV and fracture spacing change dramatically as fracture spacing becomes less and less important as permeability increases. This is due to interference being reached faster in high permeability reservoirs. Without any further calculation, it is clear from the surface plots that optimum economic configurations tend to be in the short spacing range.

The total run time associated with the 75 cases studied in this section is less than a day, thus proving the efficiency of simplified models that result from the application of the present standardized workflow.

3.7 Key Findings

A new standardized simplification workflow was presented and proven to greatly reduce simulation run times while achieving accurate results for production from low-permeability formations with hydraulically fractured wells. The simplification steps were explained in detail by accounting for phenomena that contribute to fluid flow, building a solution process diagram and crossing out phenomena deemed not relevant. A simulation model, which is a representative unit of a full-scale model and based on the simplified solution process, is built and its results are then modified to represent the full-scale behavior. It was shown that models resulting from this process require very low simulation run times while producing results that match full-scale model results. It was also shown that other simplified models may not be accurate representations of a full-scale system, thus proving the necessity for a new standardized simplification workflow.

CHAPTER 4

A NEW DISCRETE FRACTURE MODEL IMPLEMENTATION

Natural fractures have been identified as important fluid flow drivers for most unconventional reservoirs. In most cases, history matching through reservoir simulation is not possible without due consideration of fracture contributions to the flow. In light of this, several attempts have emerged to include and properly represent natural and hydraulic fracture physics into numerical simulation.

Amongst the most popular fracture representations found in the literature, three models seem to be standard for most engineering practices: single continuum, dual porosity, and the discrete fracture model. Even though studies have shown the advantages and disadvantages of some of these models,[55] the relative low simulation run times and explicit representation of fracture networks make the discrete fracture model the preferred method.

Implementations of the discrete fracture methodology have been made to finite element method (FEM) simulators in the last decades with promising results. A brief introduction to reservoir fractures from a geological point of view is followed by a discussion on the finite element numerical methods used in this research work. With this background information, the DFM implementation to FEM simulation is introduced and a new approach to the discrete fracture concept is proposed.

Verification studies are performed on the newly developed approach by comparison to

analytical solutions and single continuum simulation results. The strengths, weaknesses and possible improvements to the suggested implementation are then discussed.

4.1 Background

4.1.1 Natural and Hydraulic Fractures

Reservoir fractures can be defined as macroscopic planar discontinuities where a loss of rock cohesion has taken place through geological processes such as overburden or tectonic forces.[56] Hydraulic fractures, on the other hand, are artificially created by injection of water into the rock, eventually causing the rock medium to crack. These fissures are then held open by proppant agents. Hydraulic fractures may be engineered to acquire certain penetration, half lengths, and widths within the reservoir and are generally depicted as shown in **Figure 2.3** and **Figure 3.1**. Even though natural and hydraulic fractures are complex phenomena still under research, fractures in general can be described as ruptures in reservoir rocks.

Most fractures can be characterized as faults and joints as shown in **Figure 4.1**. Faults are fractures along which one side has moved relative to rock on the other side.[57] When no movement has occurred, the fractures are then known as joints.

Faults can be categorized in one of two big groups: Dip slip and strike slip faults. Dip slip faults separate two rock blocks known as the hanging wall and footwall where the motion of the hanging wall relative to the footwall block occurs in a direction parallel to the dip of the fault plane. Depending on the movement direction of the hanging wall, inclined slip faults can be classified as normal faults or reverse faults as shown in **Figure 4.2**.

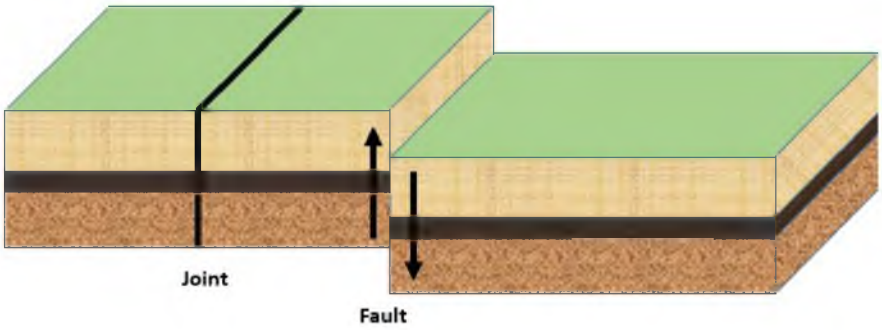

Figure 4.1 Fault and joint visual representation

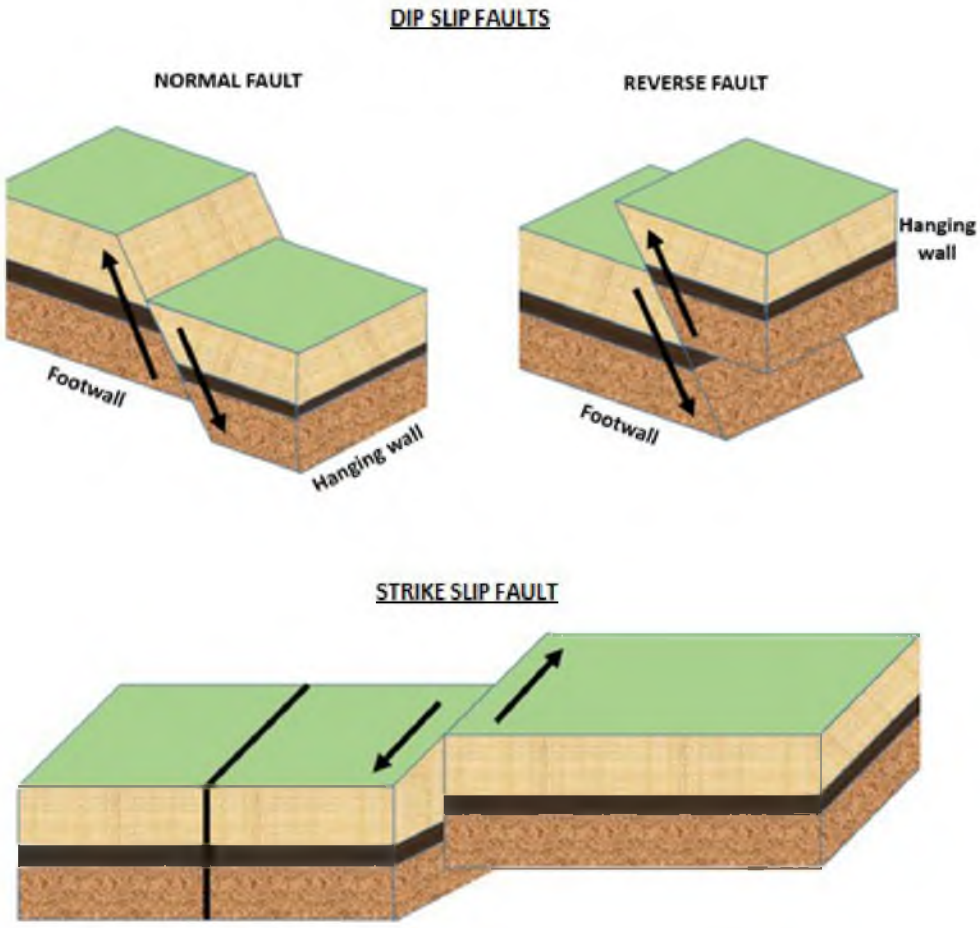

Figure 4.2 Schematics of dip slip and strike slip faults.

Strike slip faults, on the other hand, do not have hanging walls or foot walls, this is because the motion of the pair of rock blocks occurs in a direction parallel to the strike line of the fault plane. This is also illustrated in **Figure 4.2**.

The theory on fractures from a geological standpoint is too robust to be included in this section. Ample information in regard to the formation, classification, and evaluation of fractures can be found elsewhere. [57, 58]

4.1.2 Fracture Representation in Numerical Simulation

Fractures need to be characterized before consideration into numerical simulation is considered. Fracture information such as height, half-length, and conductivity is obtained by geophysicists and stimulation engineers. Seismic surveying at the time of hydraulically fracturing the target reservoir is one of the most trusted tools to gather information about the morphology and growth of fractures.[59] Information of the injection schedule, proppant, and fracking fluid is also used to determine fracture size through simulation when microseismic mapping is not available.

Because fracture permeability and width are hard to come by independently, fracture conductivity has become an important measure for fracture flow effectiveness. Fracture conductivity is defined as follows:

$$C_f = \mathrm{wk}_f \tag{4.1}$$

Equation 4.1 is usually expressed in field units of [md-ft]. To help understand fracture conductivity's relationship with the matrix, the dimensionless conductivity is introduced:

$$C_{fD} = \frac{\mathrm{wk}_f}{\pi k x_f} \tag{4.2}$$

Cinco-Ley et al. (1978)[60] showed that a dimensionless conductivity of 10 or more

reduces fracture pressure drop considerably. Hence, values for dimensionless conductivity at this range are considered essentially infinite. Non-Darcy effects are accounted for by correcting the dimensionless fracture conductivity as shown by Gidley (1991).[61]

Despite advances being made in the analysis of fractures, numerical simulation remains as the only way to handle complex fracture networks. However, fracture representations in the simulation space are varied and have been implemented in various type of simulators. For the most part, there are three common methods used to model fractures:

1. Single porosity model
2. Dual porosity model
3. Discrete Fracture Model (DFM)

The following sections are dedicated to reviewing these models.

4.1.2.1 The Single Porosity Model

This fracture model has been vastly used in the literature and consists of simply representing fractures explicitly. The fracture is meshed together with the matrix and the properties are given explicitly to the grid blocks hosting the fracture. Grid refinement around the fracture is necessary for convergence and can be distributed logarithmically or linearly as studied by Panja et al. (2014).[62] A simple single porosity model is shown in **Figure 4.3**

The main disadvantage of the single porosity model is the large (sometimes enormous) number of grid blocks associated with the model that result in very long run times and large model sizes. Even though this problem can be somewhat alleviated with the introduction

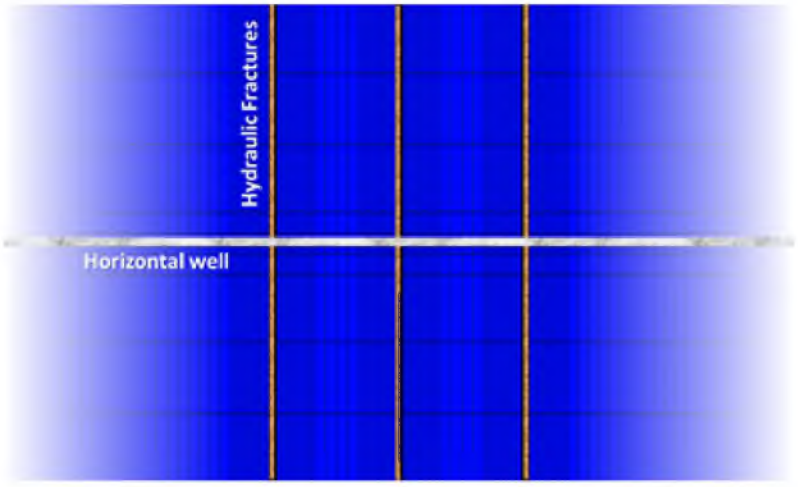

Figure 4.3 Top view of a single porosity fracture model with linear grid refinement

of Local Grid Refinement (LGR) techniques, other modeling techniques have emerged to address proper physical representation of the fracture while keeping run times relatively low.

There is a second approach to the single porosity model where the permeability tensor for each grid block is modified to include the influence of fractures to fluid flow.[63] The modified permeability is obtained using upscale methods as described by Oda (1985).[64] However, this approach is mostly used to model short fractures as the characteristic length of the fracture is smaller than the characteristic length of the hosting grid-block.

4.1.2.2 The Dual Porosity Model

The main concept of the dual porosity model is that matrix blocks and fractures are represented by two different continua. Fluid flow is carried through connecting fractures while the reservoir volume is represented by matrix blocks. A shape factor describes the connectivity of flow between matrix blocks and fractures. Mathematically, this model can

be expressed as:

$$\Omega = \Omega_m + \Omega_f \tag{4.3}$$

A schematic of the dual porosity concept is shown in **Figure 4.4**. This model was first introduced by Warren et al. (1963)[65] to model natural fractures in single phase flow systems. Kazemi et al. (1976)[66] later introduced a dual porosity application to a two phase immiscible system. The governing equations for fractures and matrix blocks are shown as follows:

$$\Omega_f: \quad \frac{\partial}{\partial t}\left(\frac{\varphi S_p}{B_p}\right)_f = q_{p,mf} + \nabla \cdot \left(\frac{kr_p}{\mu_p}\right)_f \bar{\bar{\mathbf{K}}}_f \nabla \Phi_p \tag{4.4}$$

$$\Omega_m: \quad \frac{\partial}{\partial t}\left(\frac{\varphi S_p}{B_p}\right)_m = -q_{p,mf} \tag{4.5}$$

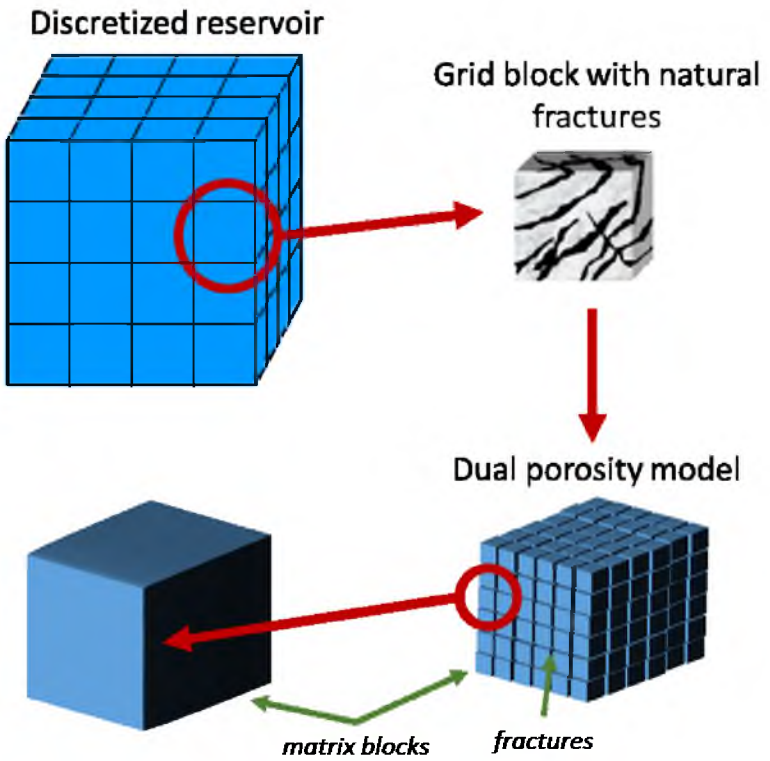

Figure 4.4 Dual porosity model representation

where $q_{p,mf}$ in equations 4.4 and 4.5 is the matrix-fracture transfer function and can be calculated with equation 4.6.

$$q_{p,mf} = \sigma \bar{\bar{\mathbf{K}}}_{\boldsymbol{m}} \left(\frac{kr_p}{\mu_p}\right)\left(\Phi_{p,m} - \Phi_{p,f}\right) \tag{4.6}$$

where σ is the shape factor which can be calculated as shown by equation 4.7

$$\sigma = \frac{4N(N+2)}{l^2} \tag{4.7}$$

N is the number of fracture normal sets. Calculation of l for $N = 1, 2$, and 3 is shown as follows:

$$l = \begin{cases} l_x & N = 1 \\ \dfrac{2l_x l_y}{l_x + l_y} & N = 2 \\ \dfrac{3l_x l_y l_z}{l_x l_y + l_y l_z + l_x l_z} & N = 3 \end{cases} \tag{4.8}$$

where l_x, l_y and l_z are spacings of fractures planes for each direction.

The shape factor can also be calculated based on the Gilman-Kazemi[67] formulation as shown in equation 4.9.

$$\sigma = 4\left(\frac{1}{l_x^2} + \frac{1}{l_y^2} + \frac{1}{l_z^2}\right) \tag{4.9}$$

The concept of the shape factor, however, is controversial given the fact that a rigorous theoretical base for this concept is nonexistent. This remains one of the main drawbacks of the classic dual porosity model even though some work was made to address this particular issue.[68,69,70]

The original dual porosity model has other disadvantages that include the lack of gravity drainage, capillary continuity, reinfiltration, and viscous displacement. Fortunately, several researchers have proposed various improvements to account for gravity

segregation.[71-73] Other research efforts went into the development of a subdomain model[67,72-76] and a pseudo function method.[73-81]

A new implementation to the classic dual porosity model extends the original concept of matrix-to-fracture flow to incorporate matrix-to-matrix and fracture-to-fracture flow. This implementation is known as the dual porosity / dual permeability model and can be compared to the classic dual porosity model as shown in **Figure 4.5**. This formulation is governed by equations 4.10 and 4.11.

$$\Omega_f: \quad \frac{\partial}{\partial t}\left(\frac{\varphi S_p}{B_p}\right)_f = -q_{p,mf} + \nabla \cdot \left(\frac{kr_p}{\mu_p}\right)_f \bar{\bar{\mathbf{K}}}_f \nabla \Phi_p \tag{4.10}$$

$$\Omega_m: \quad \frac{\partial}{\partial t}\left(\frac{\varphi S_p}{B_p}\right)_m = q_{p,mf} + \nabla \cdot \left(\frac{kr_p}{\mu_p}\right)_m \bar{\bar{\mathbf{K}}}_m \nabla \Phi_p \tag{4.11}$$

The additional term in the matrix equation expresses the matrix-to-matrix flow portion of the dual porosity / dual permeability formulation. In fact, this additional term results in a model that requires greater computational effort than the classic dual porosity model.

The limitations of the dual porosity model are well recognized for several applications. Because fractures are not modeled explicitly, hydraulic fracture modeling can become challenging. This problem is only accentuated by considering the lack of a rigorous basis for shape factors as previously discussed. For this reason, fracture interpretation through the discrete fracture model seems to be a solution.

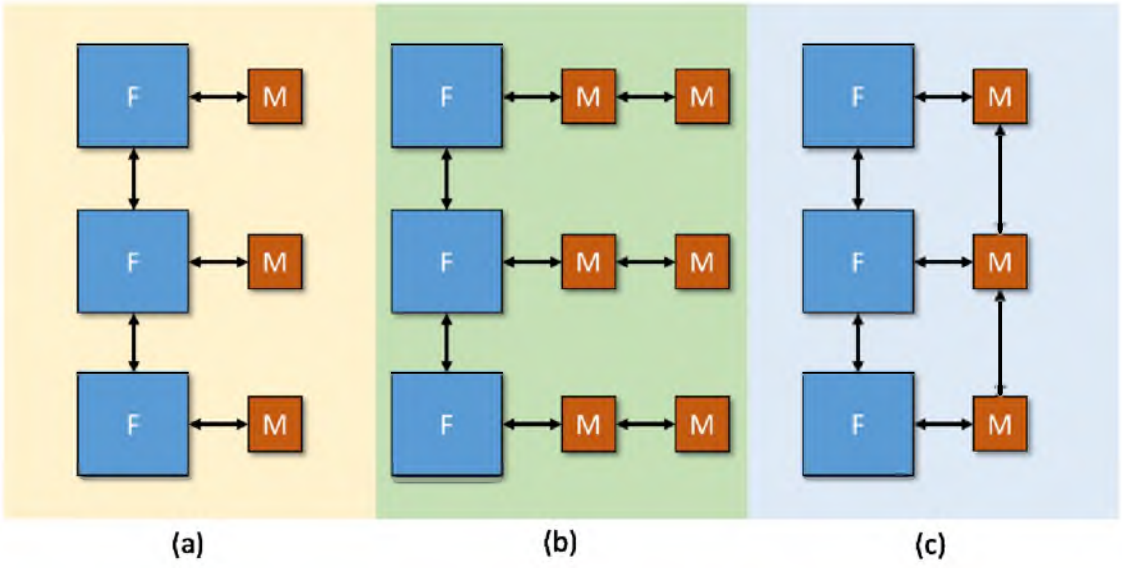

Figure 4.5 Matrix-Fracture connectivity schematic for the (a) dual porosity model, (b) subdomain model and (c) dual porosity / dual permeability model.

4.1.2.3 The Discrete Fracture Model

In the discrete fracture model formulation, the matrix is an n-dimensional domain that contains fractures represented by (n-1)-dimensional elements. For instance, a two-dimensional discretized reservoir contains one-dimensional fractures shown as lines as visualized in **Figure 4.6**.

One of the earliest papers that used the DFM formulation to study fluid flow in a porous medium was published by Wilson et al. (1974).[82] In this paper, they studied steady-state seepage in a fracture system beneath a dam. The first model consisted of an unstructured single porosity model where fractures are represented by triangular finite elements. In the second model, one-dimensional finite elements represent fractures in an impermeable medium.

A two-dimensional model was implemented in a fractured medium using upstream weighted finite element method by Noorishad et al. (1982).[83] Baca et al. (1984)[84] followed

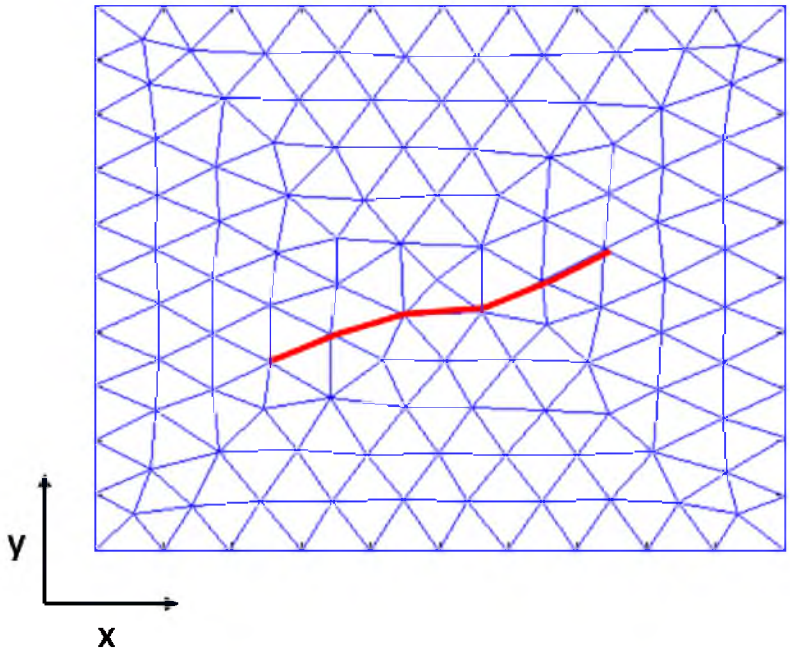

Figure 4.6 Reservoir triangular element discretization around a fracture (red line)

a similar approach to study two-dimensional single phase flow with heat and solute transport. Single phase approach was then extended by Bourbiaux et al. (1999)[68] to multiphase flow, where a joint-element technique was used to represent fracture networks.

Kim et al.[55,85,86] and Yang (2003)[87] used a similar approach as Noorishad et al. and Baca et al. to develop a two-phase black oil model with a parallel computing option. Karimi (2001)[88] applied the same concept and developed an Implicit Pressure Explicit Saturation (IMPES) two-phase black oil model simulator. Fu (2007)[89] extended this application to a three-dimensional fully implicit multiphase flow simulator where fractures are represented as triangular faces of tetrahedrons. Monteagudo et al.[90,91] introduced a crossflow equilibrium concept between fractures and matrix to address the issue of capillary continuity.

In summary, the discrete model offers several advantages over the single porosity and

dual porosity models:

- Fractures are modeled explicitly. The effect of individual fractures on fluid flow are accounted for.
- Computational time is greatly reduced.

For these reasons, the DFM has been developed and widely implemented to finite difference and finite element simulators. However, one disadvantage remains in that (n-1)-dimensional fracture elements share the same pressures as their host matrix control volumes. In other words, fractures are mathematically an additional flux term to their host control volumes while having no control volumes on their own. This results in fracture capacity being ignored altogether during simulation.

After a brief discussion on the mass conservation equations and discretization methods used to develop a two-dimensional two-phase simulator, a new DFM implementation is introduced. This novel approach makes use of existing tools in an attempt to grant fractures with their own control volumes without dealing with complicated remeshing schemes. In fact, fracture orientation and position are shown to be independent of matrix gridding.

4.2 Governing Equations

The continuity equation for a single-phase flow problem can be derived from classic continuity equations.[19]

$$-\nabla \cdot \rho \mathbf{v} = \frac{\partial \varphi \rho}{\partial t} + \bar{q} \tag{4.12}$$

Dividing the fluid flow continuity equation by fluid density at standard conditions and combining it with the formation volume factor definition (shown in APPENDIX A) yields:

$$-\nabla \cdot \frac{\mathbf{v_l}}{B_l} = \frac{\partial}{\partial t}\left(\frac{\varphi S_l}{B_l}\right) + q_l \tag{4.13}$$

Where the subscript l refers to a fluid phase and q_l is the volume produced or injected per unit bulk volume per unit time at standard conditions.

To fully accommodate equation 4.13 for multiphase flow, the concept of relative permeability is applied:

$$\nabla \cdot \left(\frac{\mathbf{k}k_{rl}}{B_l\mu_l}\nabla\Phi_l\right) = \frac{\partial}{\partial t}\left(\frac{\phi S_l}{B_l}\right) + q_l \tag{4.14}$$

For a three-phase system consisting of oil, water, and gas, the governing equations for each phase are:

$$\text{Oil:} \quad \nabla \cdot \left(\frac{\mathbf{k}k_{ro}}{B_o\mu_o}\nabla\Phi_o\right) = \frac{\partial}{\partial t}\left(\frac{\phi S_o}{B_o}\right) + q_o,$$

$$\text{Water:} \quad \nabla \cdot \left(\frac{\mathbf{k}k_{rw}}{B_w\mu_w}\nabla\Phi_w\right) = \frac{\partial}{\partial t}\left(\frac{\phi S_w}{B_w}\right) + q_w, \tag{4.15}$$

$$\text{Gas:} \quad \nabla \cdot \left(R_s\frac{\mathbf{k}k_{ro}}{B_o\mu_o}\nabla\Phi_o + \frac{\mathbf{k}k_{rg}}{B_g\mu_g}\nabla\Phi_g\right)$$

$$= \frac{\partial}{\partial t}\left(\frac{\varphi S_o}{B_o}R_s + \frac{\phi S_g}{B_g}\right) + R_s q_o + q_g.$$

Notice that the gas governing equation accounts for gas flow from free gas in the system as well as gas present in the oil phase. These equations are tied by capillary and volume conservation rules:

$$P_{cow}(S_w) = P_o - P_w \tag{4.16}$$

$$P_{cog}(S_g) = P_g - P_o \tag{4.17}$$

$$S_o + S_w + S_g = 1 \tag{4.18}$$

The system of equations presented in this section describe the multiphase fluid flow system. These equations are commonly solved in a discretized fashion either by finite

difference or finite element methods. For any kind of discretization method used in this research work, the general governing equation 4.13 can be rearranged as a residual function and integrated over a control volume *i*:

$$R^i = 0 = \int_{\Gamma^i} \frac{\mathbf{v}}{B} \cdot \hat{\mathbf{n}} ds + \int_{cvi} \frac{\partial}{\partial t}\left(\frac{\phi S}{B}\right) dx + \int_{cvi} q dx \qquad 4.19$$

where $\hat{\mathbf{n}}$ is the unit normal outward on surface Γ^i and phase l has been omitted for clarity.

The first integral in the right hand side of equation 4.19 is the flux into or out of a defined control volume, the second integral is the accumulation term, and the last integral is the flow contribution from a well model. Definition of these terms depends on the discretization methods used. The following sections discuss common discretization methods and their definitions of transmissibility-based flux.

4.3 Numerical Methods

In the previous section, the governing system of equations was presented in their rigorous forms. In order to solve these equations, numerical methods are employed in reservoir simulation. To achieve this, equations are discretized into a nonlinear system using temporal and spatial discretization methods. Temporal discretization is done by a regular first order method for the present work. Spatial discretization can be achieved by a general finite volume method. With implementation of finite volumes into this framework, geometrical information can be obtained in order to calculate:

1. Volumes corresponding to each control volume node in order to compute accumulation terms.
2. Transmissibility between connected control volumes which is then used to compute flow terms.

Bulk finite volume and transmissibility calculations are made depending on the discretization method of choice.

4.3.1 Transmissibility

The concept of transmissibility-based flow calculation is now widespread in commercial simulators for both finite difference and finite element methods. The mathematical description of transmissibility and relation to flux has been discussed extensively.[92-94] and is only summarized here.

Mathematically, transmissibility between two finite irregular volumes Ω_I and Ω_J is defined as:

$$T_{i,I,J} = \bar{\bar{\mathbf{K}}}\nabla\alpha_i \cdot \vec{n}_{I,J}A_{I,J} \qquad 4.20$$

where α_i is an interpolation function.

As shown by equation 4.20, transmissibility is only dependent on static values of the permeability tensor and the geometry of control volumes. This information can be pre-computed before simulation starts for storage and later use. With this equation at hand, flux for phase l between volumes Ω_I and Ω_J can be expressed as:

$$F_{l,I,J} = \frac{k_{rl}}{\mu_l}\sum_{i=1}^{N_v} T_{i,I,J}\Phi_{l,i} \qquad 4.21$$

where relative permeability and viscosity are determined using an upstream weighing scheme and N_v is the number of connected nodes.

Equation 4.21 is computed depending on the discretization method applied. The next few sections will briefly address some common discretization method based on transmissibility-based finite volume flow.

4.3.1.1 Classic Finite Difference Method

The finite difference method is the most widespread discretization scheme for reservoir simulation. In this method, all finite volumes are rectangular blocks where variables are assigned inside the block. Volume for block i is trivially calculated as shown below:

$$V_i = DxDyDz \tag{4.22}$$

Transmissibility between two adjacent finite volumes I and J in the x-direction can be calculated as shown by Abou-Kaseem et al. (2013).[95]

$$T_{i,I,J} = \frac{2\beta_c}{\frac{Dx_I}{A_I k_{I,J}} + \frac{Dx_J}{A_J k_{I,J}}} \tag{4.23}$$

where β_c is a unit conversion factor and A refers to the involved block cross-section areas shown in **Figure 4.7**. Material balance dictates that transmissibility from block J to I is:

$$T_{j,I,J} = -T_{i,I,J} \tag{4.24}$$

Flux can now be calculated. Since $N_v = 2$, substitution into equation 4.21 yields:

$$F_{l,I,J} = \frac{k_{rl}}{\mu_l}(T_{i,I,J}\Phi_{l,i} + T_{j,I,J}\Phi_{l,j}) \tag{4.25}$$

The general finite difference method gives rise to two grid systems: the block-centered grid and the point-distributed grid. The main difference between these two grid systems are illustrated in **Figure 4.8** and listed below:[95]

1. Boundary grid points for a point-distributed grid are placed on boundaries and not inside grid blocks as in the block-centered grid.
2. Bulk volumes and rates for boundary grid points are a half, a quarter or an eighth of whole blocks depending on the number of boundaries they fall on.
3. The transmissibility of boundary grid points parallel to the boundary is half of what it would be for a whole block.

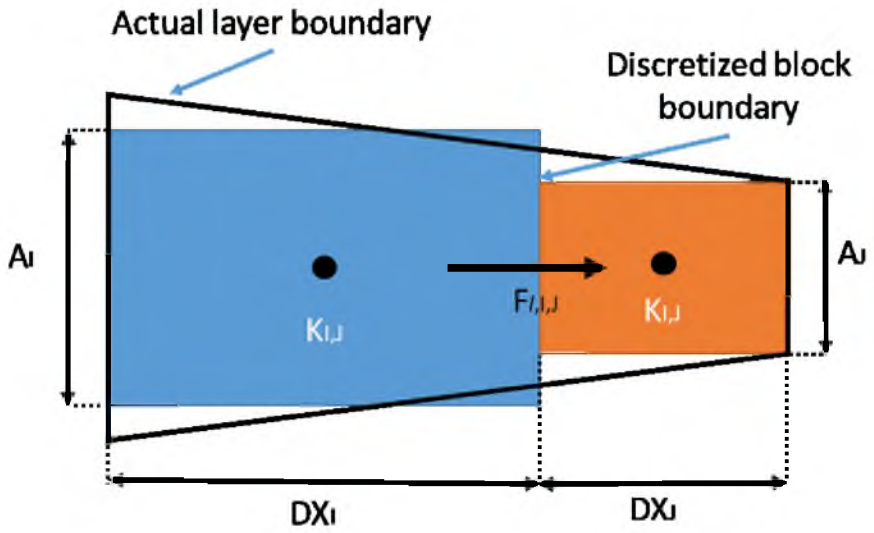

Figure 4.7 Transmissibility illustration for the classic finite difference method

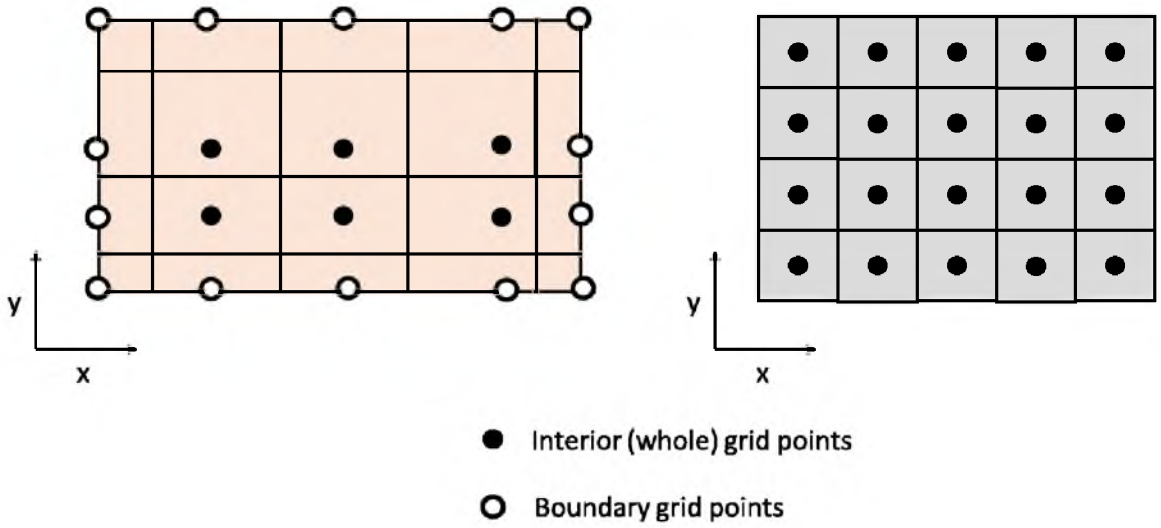

Figure 4.8 Example configurations for a point-distributed (left) and block-centered grid (right) systems

4.3.1.2 Corner Point Method

Complex reservoir models have always been a challenge for standard finite difference grid systems. The corner point method addresses these challenges by defining three-dimensional finite volumes through eight corner points, thus allowing for distorted geometries. Corner point volumes are formed by six tetrahedrons, each tetrahedron is defined by four vertices as shown by equation 4.26:

$$\begin{aligned} a &= (a_1, a_2, a_3), \\ b &= (b_1, b_2, b_3), \\ c &= (c_1, c_2, c_3), \\ d &= (d_1, d_2, d_3), \end{aligned} \tag{4.26}$$

As the complexity of these blocks grows, so do their volume and transmissibility calculations. By noting vertex coordinates, tetrahedron volumes can be calculated as:

$$C_i = \frac{1}{6}\|\det(a-b, b-c, c-d)\| \tag{4.27}$$

Transmissibility between blocks I and J shown in **Figure 4.9** can be calculated as shown below[96]:

$$T_{i,I,J} = \frac{1}{\frac{1}{T_I^*} + \frac{1}{T_J^*}} \tag{4.28}$$

which is basically a harmonic average of the x-direction transmissibilities of the connected blocks. These are computed as:

$$T_I^* = k_{x,I}\frac{A_{x,I,J}Dx_I + A_{y,I,J}Dy_I + A_{z,I,J}Dz_I}{{Dx_I}^2 + {Dy_I}^2 + {Dz_I}^2} \tag{4.29}$$

$$T_J^* = k_{x,J}\frac{A_{x,I,J}Dx_J + A_{y,I,J}Dy_J + A_{z,I,J}Dz_J}{{Dx_J}^2 + {Dy_J}^2 + {Dz_J}^2} \tag{4.30}$$

Similarly to the standard finite difference method, transmissibility from J to I, and flux

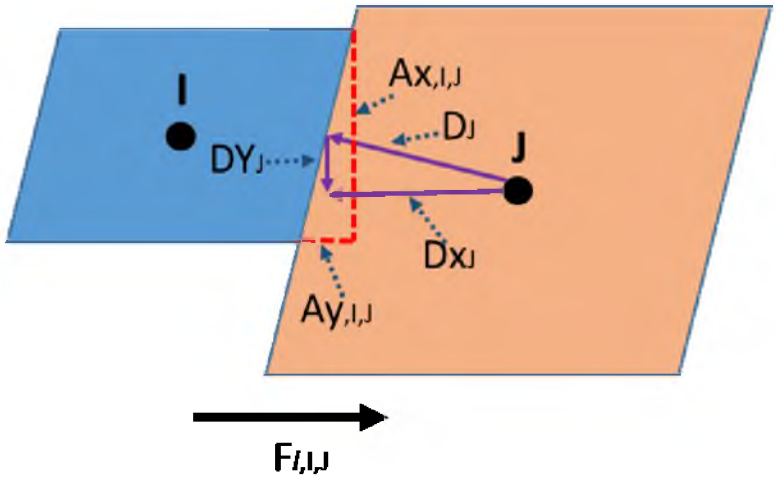

Figure 4.9 Transmissibility illustration for the corner-point method

are calculated as shown below:

$$T_{j,I,J} = -T_{i,I,J} \tag{4.31}$$

$$F_{l,I,J} = \frac{k_{rl}}{\mu_l}(T_{i,I,J}\Phi_{l,i} + T_{j,I,J}\Phi_{l,j}) \tag{4.32}$$

4.3.1.3 Control Volume Finite Element Method

In this research work, the CVFEM as developed by Yang (2003),[87] Fu (2007),[89] and is considered for implementation. In 2D cases, reservoir domains are discretized into triangular elements, whereas in 3D the domain is discretized into tetrahedral elements. Because the aim of this work is to introduce a new discrete fracture model, a 2D simulator was developed to test the physics of the new DFM concept. Henceforth, the CVFEM discretization method for a two-dimensional simulator is introduced here.

Figure 4.10 shows a triangular element containing three subcontrol volumes associated with vertices that meet at the centroid. The sum of all subcontrol volumes associated to a particular vertex assembles a complete control volume as shown in **Figure 4.11**.

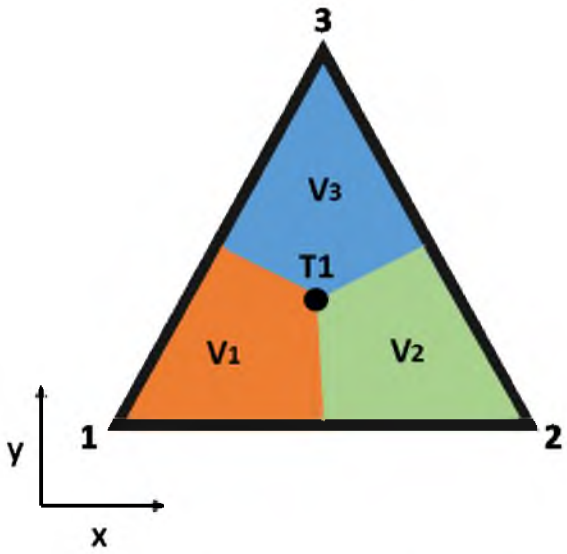

Figure 4.10 Simple triangular element and its associated subcontrol volumes

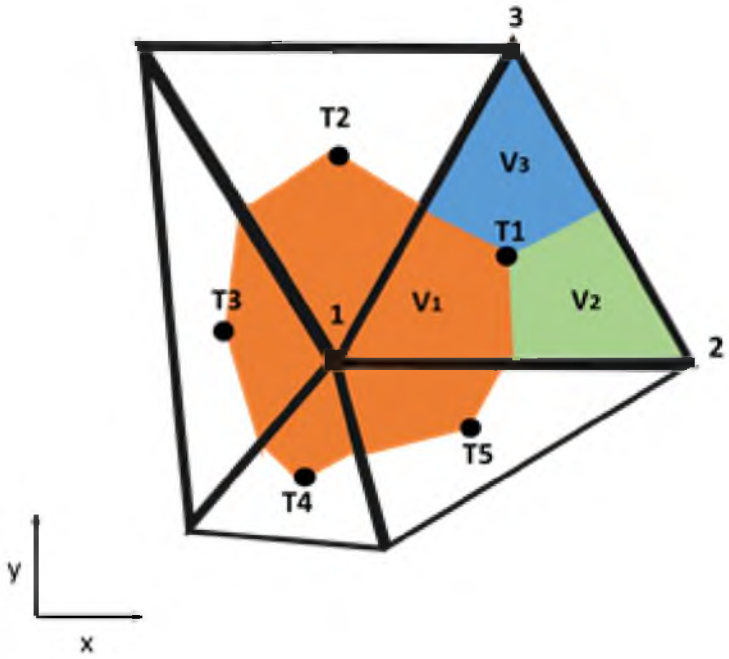

Figure 4.11 Assembly of control volume associated to vertex "1"

The transmissibility, bulk volume, and weighting scheme for the mobility term for this discretization method are introduced next. Letting ∃ represent a triangular element space, the area of a triangle can be calculated by:

$$A_{\exists} = \frac{1}{2}\det\begin{bmatrix} x_1 & x_2 & x_3 \\ y_1 & y_2 & y_3 \\ 1 & 1 & 1 \end{bmatrix} \tag{4.33}$$

Equation 4.33 is useful for calculating bulk volumes. To derive transmissibilities we begin by defining the value of an element property located at $\mathbf{x} \in \Omega$:

$$\omega(\mathbf{x}) = \sum_{i=1}^{3} \omega_i L_i(\mathbf{x}) \tag{4.34}$$

where ω_i denotes the value of ω at vertex i inside the triangular element, and $L_i(\mathbf{x})$ is a linear interpolation function factor which is defined in natural coordinates as:

$$L_i = \frac{A_i}{A_{\exists}} \tag{4.35}$$

which is related to other triangular vertices values as follows:

$$L_1 + L_2 + L_3 = 1 \tag{4.36}$$

Hence, the property of location can be derived from equation 4.34:

$$\begin{aligned} x &= L_1 x_1 + L_2 x_2 + L_3 x_3 \\ y &= L_1 y_1 + L_2 y_2 + L_3 y_3 \end{aligned} \tag{4.37}$$

Expressed in matrix form, equation 4.37 can be rewritten as:

$$\begin{Bmatrix} x \\ y \\ 1 \end{Bmatrix} = \begin{bmatrix} x_1 & x_2 & x_3 \\ y_1 & y_2 & y_3 \\ 1 & 1 & 1 \end{bmatrix} \cdot \begin{Bmatrix} L_1 \\ L_2 \\ L_3 \end{Bmatrix} = \begin{bmatrix} x_1 & x_2 & x_3 \\ y_1 & y_2 & y_3 \\ 1 & 1 & 1 \end{bmatrix} \cdot \vec{L} \tag{4.38}$$

Or,

$$\vec{L} = \begin{bmatrix} x_1 & x_2 & x_3 \\ y_1 & y_2 & y_3 \\ 1 & 1 & 1 \end{bmatrix}^{-1} \cdot \begin{Bmatrix} x \\ y \\ 1 \end{Bmatrix} = \bar{\bar{\mathbf{C}}}^{-1} \cdot \begin{Bmatrix} x \\ y \\ 1 \end{Bmatrix} \tag{4.39}$$

Applying gradients,

$$\nabla\vec{L} = \bar{\bar{\mathbf{C}}}^{-1} \cdot \begin{bmatrix} \nabla x \\ \nabla y \\ \nabla 1 \end{bmatrix} \tag{4.40}$$

Or,

$$\nabla\vec{L} = \bar{\bar{\mathbf{C}}}^{-1} \cdot \begin{bmatrix} 1 & 0 \\ 0 & 1 \\ 0 & 0 \end{bmatrix} \tag{4.41}$$

By substituting equation 4.41 into equation 4.20, transmissibility is calculated as:

$$T_{i,I,J} = \left(\begin{bmatrix} k_{xx} & k_{xy} \\ k_{yx} & k_{yy} \end{bmatrix} \begin{Bmatrix} \frac{\partial L_i}{\partial x} \\ \frac{\partial L_i}{\partial y} \end{Bmatrix} \right)^{\mathrm{T}} \cdot \begin{Bmatrix} n_x \\ n_y \end{Bmatrix} M_{I,J} \tag{4.42}$$

where $M_{I,J}$ is the length of the interface between partial control volumes I and J.

Knowing that $N_v = 3$ for triangular elements, application of equation 4.21 yields a flux expression:

$$F_{l,I,J} = \frac{k_{rl}}{\mu_l}\left(T_{1,I,J}\Phi_{l,1} + T_{2,I,J}\Phi_{l,2} + T_{3,I,J}\Phi_{l,3}\right) \tag{4.43}$$

The flux term for a CVFEM discretization scheme is then fully defined.

4.3.2 Mobility Term Upstream Weighting

For multiphase flow, the flux across the interface area between two subcontrol volumes must be continuous. This is why the mobility term in the transmissibility calculation must have a single representative value for the interface. The upstream weighting scheme is used to determine the mobility term based on the direction of the flux as shown mathematically:

$$\frac{k_{rl}}{\mu_l} = m_p = \begin{cases} m_{p,I} & \text{if} \quad \nabla\Phi \cdot \vec{n}_{I,J} A_{I,J} \geq 0 \\ m_{p,J} & \text{if} \quad \nabla\Phi \cdot \vec{n}_{I,J} A_{I,J} \leq 0 \end{cases} \tag{4.44}$$

4.3.3 Formulation of Residual Functions

Having defined the flux term for popular discretization methods, the accumulation term is discussed now. Since pressure nodes are assigned to corresponding control volumes, the calculation of porosity and saturation is constant within the control volume. As a result, the fully implicit form of an accumulation term is:

$$\mathrm{Acc}_i = \int_{cvi} \frac{\partial}{\partial t}\left(\frac{\phi S}{B}\right) dx = \frac{\partial}{\partial t}\left(\frac{\phi S}{B}\right) \int_{cvi} dx = \frac{A_i}{\Delta t}\left[\left(\frac{\phi S}{B}\right)^{n+1} - \left(\frac{\phi S}{B}\right)^{n}\right] \quad 4.45$$

where A_i is the partial area of the control volume and properties are calculated at current simulation time $(n+1)$ and previous simulation time (n). Hence, by application of transmissibility-based flux and the accumulation term, the CVFEM partial residual function for partial control volume 1 (vertex 1) in **Figure 4.10** is:

$$\mathrm{r}_{l,1}^{(T1)} = F_{l,1,2} + F_{l,1,3} + \mathrm{Acc}_1 \quad 4.46$$

The partial residual function is calculated on an element-basis. To determine the global residual function, a sum of all partial residual functions from the elements that assemble a control volume is performed as visually shown in **Figure 4.11**.

$$\mathrm{R}_{l,1} = r_{l,1}^{(T1)} + r_{l,1}^{(T2)} + r_{l,1}^{(T3)} + r_{l,1}^{(T4)} + r_{l,1}^{(T5)} \quad 4.47$$

For a two-phase, two-dimensional system with n nodes, the residual vector is then defined as:

$$\mathbf{R} = \left[\mathrm{R}_{o,1}\ \mathrm{R}_{w,1}\ \mathrm{R}_{o,2}\ \mathrm{R}_{w,2} \cdots \mathrm{R}_{o,n}\ \mathrm{R}_{w,n}\right]^{\mathrm{T}} \quad 4.48$$

4.3.4 Current CVFEM-Based DFM Implementation

As discussed in previous sections, there exists three main fracture representation models for reservoir simulation. However, the discrete fracture model was found to be the

most practical model largely implemented into CVFEM reservoir simulation for two- and three-dimensions.[85,87,89]

The discrete fracture model is primarily known for treating fracture elements in an (n-1)-dimensional fashion for an n-dimensional reservoir domain where $\Omega = \Omega_m + \Omega_f$. For instance, in a three-dimensional domain, fractures are represented as the triangular faces of tetrahedral matrix elements and as lines for a two-dimensional case. There are three methods that can implement the DFM into CVFEM framework which are discussed below and illustrated in **Figure 4.12**.

1. **Representation 1:**

   The concept of this method was first introduced by Yang (2003)[87] for a 2D simulator and Fu (2007)[89] for a 3D simulator. In this representation shown in **Figure 4.12** (a) the vertices of the matrix element share the same properties as the vertices of its corresponding fracture. Even though properties such as rock and fluid information can be independently assigned to fractures elements and control volumes, the storage of the fracture is ignored. This is because fractures lack a control volume in their own right. Thus, the fracture contribution to flow is an additional flow term to the matrix governing equations.

2. **Representation 2:**

   Monteagudo et al. (2007)[91] introduced a different representation of the DFM where vertices of the matrix and the fracture are separated completely. Hence, fracture elements acquire their own set of properties. A cross-flow equilibrium concept is applied in this representation to eliminate transfer functions between matrix and fractures.

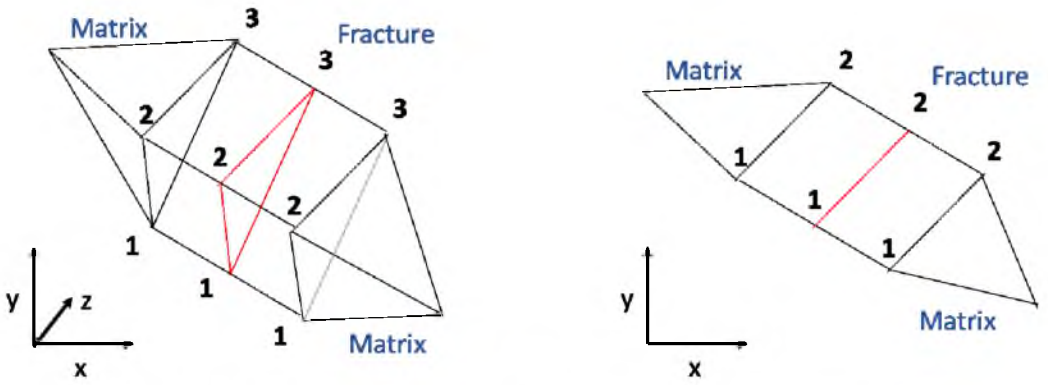

(a) Discrete fracture model 1 for 3D (left) and 2D (right) representations

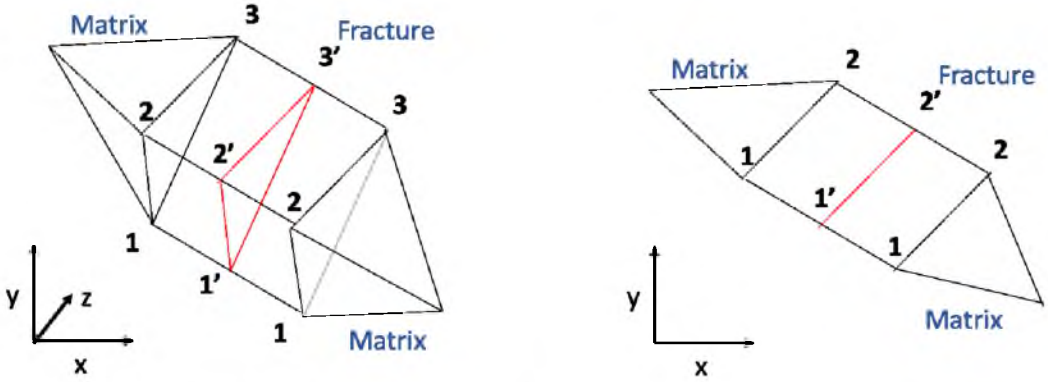

(b) Discrete fracture model 2 for 3D (left) and 2D (right) representations

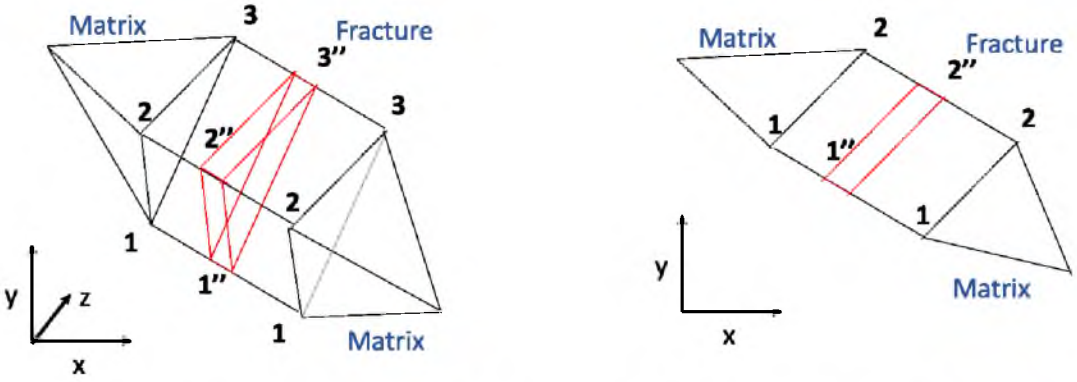

(c) Discrete fracture model 3 for 3D (left) and 2D (right) representations

Figure 4.12 Example discrete fracture representations

3. **Representation 3:**

   Here, representations 1 and 2 are combined to create a fracture model that still shares the same properties with its corresponding matrix vertices. The strength of this combination is that the model contributes to fluid flow in the form of an additional flux and provides fracture storage for fluids.

4.3.5 New CVFEM-Based DFM Implementation

In view of current DFM implementations into CVFEM simulators, a new implementation is suggested to: (1) Provide fracture nodes with their own control volumes, hence granting them with their own set of rock-fluid properties, fracture pressures and saturations and (2) Provide fracture geometries independence from matrix gridding configuration.

4.3.5.1 Fracture Representation

For a two-dimensional case, matrix discretization follows a delaunay triangulation that defines elements in Ω_m. As mentioned earlier, current DFM implementations define fracture elements from matrix nodes meaning that fracture orientation is dependent on matrix gridding. For this reason, in most DFM gridding practices, fractures are defined first as planes (for 3D) and lines (for 2D). Then, matrix gridding is done around fracture elements according to predetermined geometrical considerations.

In the new discrete fracture method, fractures are defined free of matrix gridding limitations. In other words, fractures can be placed anywhere on top of the matrix elements. Mathematically, letting $\Delta ABC \in \Omega_m$, $\overline{DE} \in \Omega_f$ and defining $S = \{x \mid \overline{DE} = \overline{AB} \vee \overline{DE} =$

$\overline{BC} \vee \overline{DE} = \overline{CA}$ } then S = "True". However, such equality is not necessarily true for the new implementation. An example of a discrete fracture network for each implementation is shown in **Figure 4.13**.

Fracture space Ω_f can be related to Ω_m when fracture fragmentation (discretization) is performed. **Figure 4.13** (b) shows a continuous fracture network with no association to matrix elements; connections between both spaces must be made to allow fluid transport through fractures. The first association is made by discretizing linear fracture elements in terms of matrix elements. To do this, we take ΔABC and $\overline{DE}$ as introduced earlier and define a set of connecting nodes as $V = \{(x, y) | \overline{DE} \cap \overline{AB} + \overline{DE} \cap \overline{BC} + \overline{DE} \cap \overline{CA}\}$ for the entire grid system.

The set of connecting nodes defines the linear fragmentation of a continuous fracture. Each resulting fracture fragment can then be handled as either an element or control volume block. A sample fragmentation is illustrated in **Figure 4.14** (a).

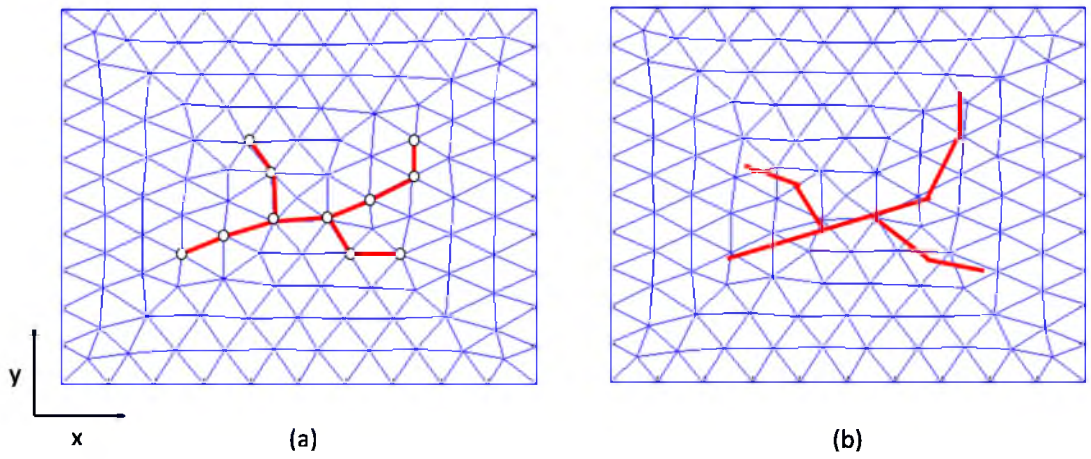

Figure 4.13 Discrete fracture elements for the (a) current and (b) the suggested implementation

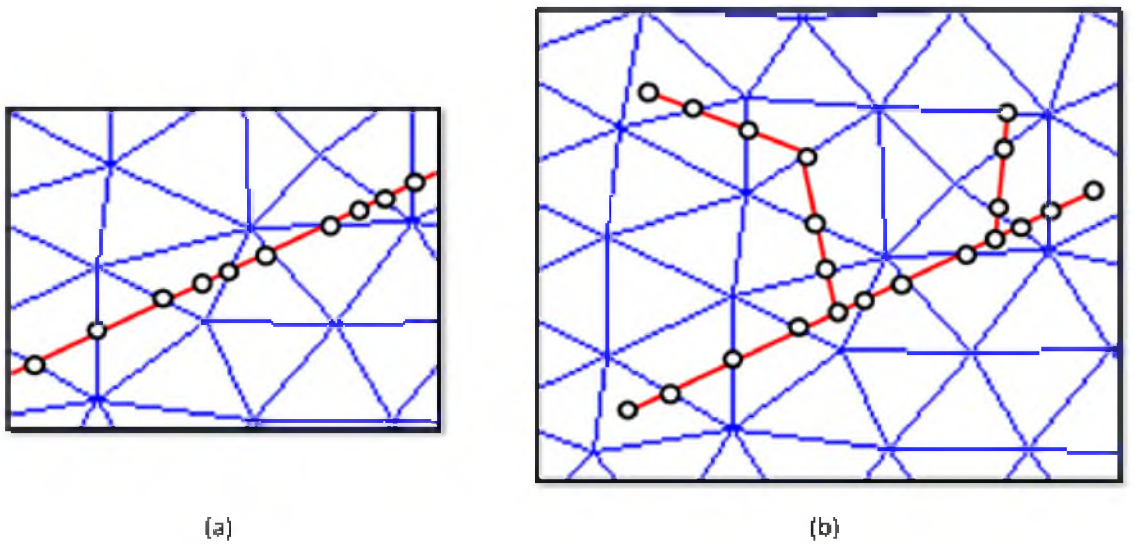

Figure 4.14 Discrete fracture (in red) fragmentation for (a) a simple and (b) a complex network

Figure 4.14 (a) illustrates the fracture fragmentation rule for a simple single irregular fracture, however, as fractures grow in complexity, new rules are added to handle fragmentation. As shown in **Figure 4.14**(b), two more fragmentation rules are added where connecting nodes are placed at fracture intersections and fracture tips.

Once fracture fragments are defined in Ω_f, fractures can be discretized using a method of choice.

4.3.5.2 Fracture Discretization

In earlier sections, popular discretization methods were discussed with some introduction to transmissibility and volume calculations. Based on the potential complexity present on fracture networks, a flexible grid system seems reasonable. This brings up methods such as the corner point and the control volume finite element schemes. Indeed, research work has been made in the area of unstructured grids that includes quadrilateral

elements. [97-100]

By using connecting nodes as a guide, fracture geometries are introduced. A set of manufactured fracture geometries corresponding to regular and irregular quadrilaterals are shown in **Figure 4.15** where fracture widths are overestimated for clarity.

There are three conclusions that emerge from inspection of **Figure 4.15**: (1) irregular blocks better represent fracture geometries by limiting fracture blocks to single matrix element, (2) when regular fracture segments form angles not equal to 180, overlapping between fracture blocks occur, and (3) at fracture intersections, overlapping occurs in regular and irregular blocks.

Although irregular blocks provide geometrical freedom for fracture blocks, the implementation is also more complicated. The definition of each irregular block is dependent on the coordinates of each vertex (which is a function of connecting nodes and matrix triangulation), whereas regular blocks can be defined only by predetermined fracture widths and connecting nodes. Because a simple implementation that compares to

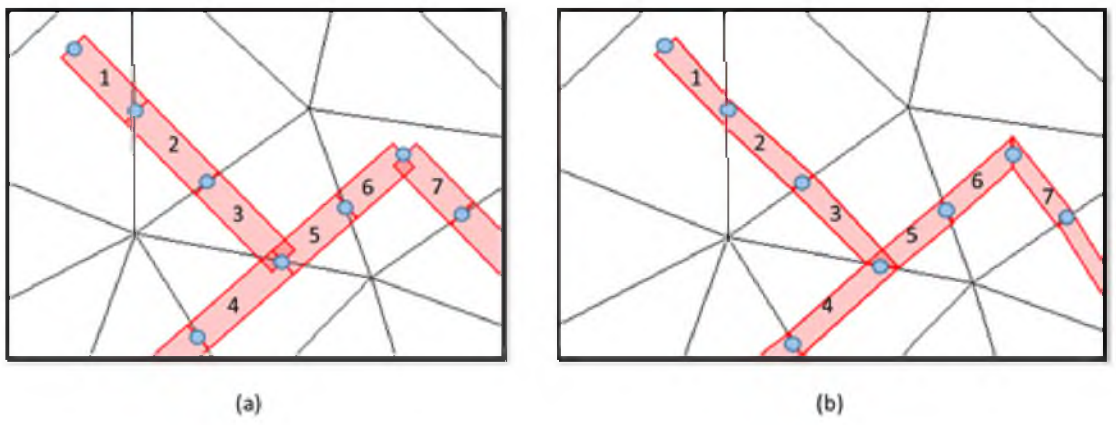

Figure 4.15 Exaggerated fracture block representations for (a) regular and (b) irregular geometries

the current DFM is sought for, a regular block geometry with a point-distributed grid system is implemented to the framework. The issue of overlapping fracture grid blocks is solved by transformation of the fracture space to a collection of linear spaces.

Understanding that fracture segments (now defined as grid-blocks) 2 and 5 or 2 and 4 as shown in **Figure 4.15** are not connected in the fracture space, means that flow will only follow a path as described by the fracture network alignment. Assuming that the matrix space contributes no flow to the fracture network, the fracture grid block branch 1-2-3-4-5-6-7 is shown in a linearized space in **Figure 4.16**.

By decomposing fracture networks into a set of discrete linearized fracture block chains, the overlapping issue is addressed. The governing equation for this discretized system is derived by looking at equation 4.14 presented earlier.

$$\nabla \cdot \left(\frac{\mathbf{k}^f k_{rl}}{B_l \mu_l} \nabla \Phi_l \right) = \frac{\partial}{\partial t} \left(\frac{\phi S_l}{B_l} \right) + q_l \qquad 4.14$$

By application of an integral over a control volume and rearranging to define a residual function:

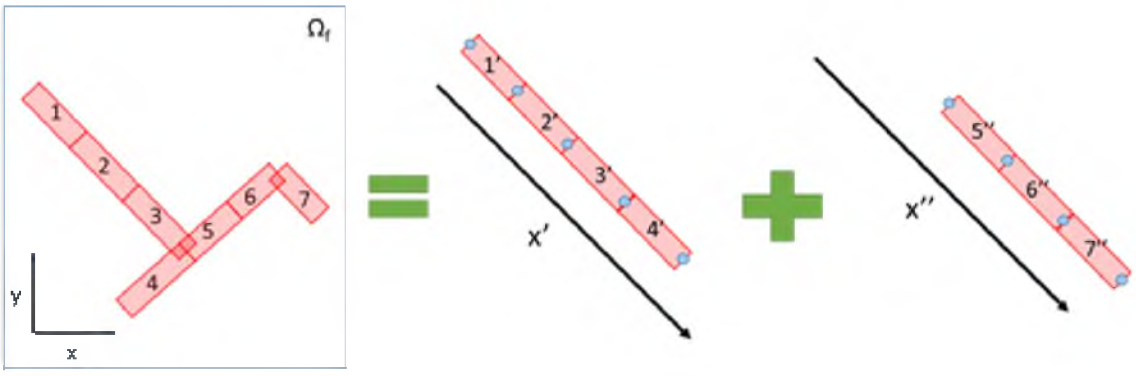

Figure 4.16 Fracture representation in linearized systems

$$R^i = 0 = -\int_{\Gamma^i} \frac{\mathbf{k}^f k_{rl}}{B_l \mu_l} \nabla \Phi_l \cdot \hat{\mathbf{n}} ds + \int_{cvi} \frac{\partial}{\partial t}\left(\frac{\phi S_l}{B_l}\right) dx + \int_{cvi} q_l dx \tag{4.49}$$

For a rectangular grid block i in a linearized system and following a finite difference discretization formulation:

$$R^i = -w_f \frac{\mathbf{k}^f k_{rl}}{B_l \mu_l} \nabla \Phi_{l,i+1} \hat{\mathbf{n}}' - w_f \frac{\mathbf{k}^f k_{rl}}{B_l \mu_l} \nabla \Phi_{l,i-1} \hat{\mathbf{n}}' + \frac{A_i}{\Delta t}\left(\left[\left(\frac{\phi S_l}{B_l}\right)^{n+1} - \left(\frac{\phi S_l}{B_l}\right)^{n}\right]\right) + q_{well} + q_{MF} + q_g \tag{4.50}$$

where w_f is fracture width, and $\int_{cvi} q_l dx$ is treated as the sum of flux terms for well models, matrix-fracture flow, and fluxes from different fracture linear spaces. Defining grid-block centers as a function of connecting nodes:

$$b_i(x, y) = \left(\left[\frac{p_{i,1}(x) + p_{i,2}(x)}{2}\right], \left[\frac{p_{i,1}(y) + p_{i,2}(y)}{2}\right]\right) \tag{4.51}$$

where b_i is a grid-block point and points $p_{i,1}$ and $p_{i,2}$ are its corresponding connecting nodes. Now, potential gradient can be defined for a linear system as follows:

$$\nabla \Phi_{l,i+1} = \frac{\Phi_{l,i+1} - \Phi_{l,i}}{b'_{i+1} - b'_i}$$
$$\nabla \Phi_{l,i-1} = \frac{\Phi_{l,i-1} - \Phi_{l,i}}{b'_{i-1} - b'_i} \tag{4.52}$$

Finally, the residual function for a fracture block i is calculated as:

$$\mathrm{R}_i = -w_f \frac{\mathbf{k}^f k_{rl}}{B_l \mu_l}\left(\frac{\Phi_{l,i+1} - \Phi_{l,i}}{b'_{i+1} - b'_i}\right) \hat{\mathbf{n}}' - w_f \frac{\mathbf{k}^f k_{rl}}{B_l \mu_l}\left(\frac{\Phi_{l,i-1} - \Phi_{l,i}}{b'_{i-1} - b'_i}\right) \hat{\mathbf{n}}' + \frac{A_i}{\Delta t}\left(\left[\left(\frac{\phi S_l}{B_l}\right)^{n+1} - \left(\frac{\phi S_l}{B_l}\right)^{n}\right]\right) + q_{well} + q_{MF} + q_g \tag{4.53}$$

Introducing transmissibility functions that can be precalculated before the start of a simulation:

$$T_{i,i\pm1} = \frac{\mathbf{k}^f w_f}{b'_{i\pm1} - b'_i} \tag{4.54}$$

Implementing upstream mobility ratio:

$$m_p = \frac{k_{rl}}{\mu_l} \tag{4.55}$$

The simplified residual function for a fracture linear system can be rewritten:

$$\mathrm{R}_i = -\frac{1}{B_l}\left[m_p T_{i,i+1}(\Phi_{l,i+1} - \Phi_{l,i}) + m_p T_{i,i-1}(\Phi_{l,i-1} - \Phi_{l,i})\right] \tag{4.56}$$

$$+\frac{A_i}{\Delta t}\left(\left[\left(\frac{\phi S_l}{B_l}\right)^{n+1} - \left(\frac{\phi S_l}{B_l}\right)^{n}\right]\right) + q_{well,i} + q_{MF,i} + q_{g,i}$$

As shown in **Figure 4.16**, the fracture network has been decomposed into two linear systems where grid block 3 has connectivity with grid blocks 4 and 5. The first term of the right-hand side of equation 4.56 describes the flux terms from blocks 2 and 4 into block 3. The term q_g takes into account flux contributions from decomposed fracture grid blocks, in this case, the flux from grid block 5. Hence, q_g is defined as:

$$q_{g,i} = -\sum_{\substack{n\neq i+1 \\ n\neq i-1}} \frac{m_p}{B_l}\left[T_{n,i}(\Phi_{l,n} - \Phi_{l,i})\right] \tag{4.57}$$

where n is defined as grid blocks that share connectivity nodes with i. The $q_{MF,i}$ term in equation 4.50 determines matrix flux contributions to fracture grid blocks. This flux term links matrix and fractures spaces and is illustrated in **Figure 4.17**.

The treatment of $q_{MF,i}$ is dependent on the matrix element where the fracture segment is hosted. In the current implementation, the way by which matrix potential nodes interact with fracture blocks can be illustrated as shown in **Figure 4.18**. Here, the matrix-fracture flux is the sum of all matrix node contributions.

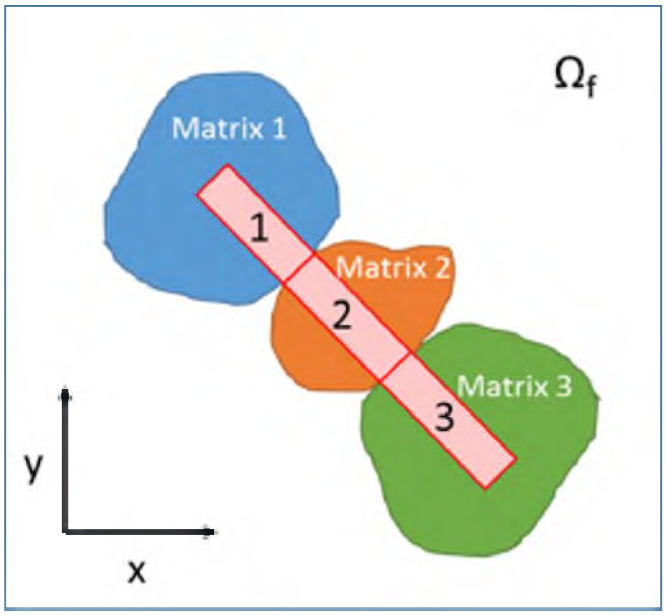

Figure 4.17 Fracture grid blocks surrounded by matrix spaces

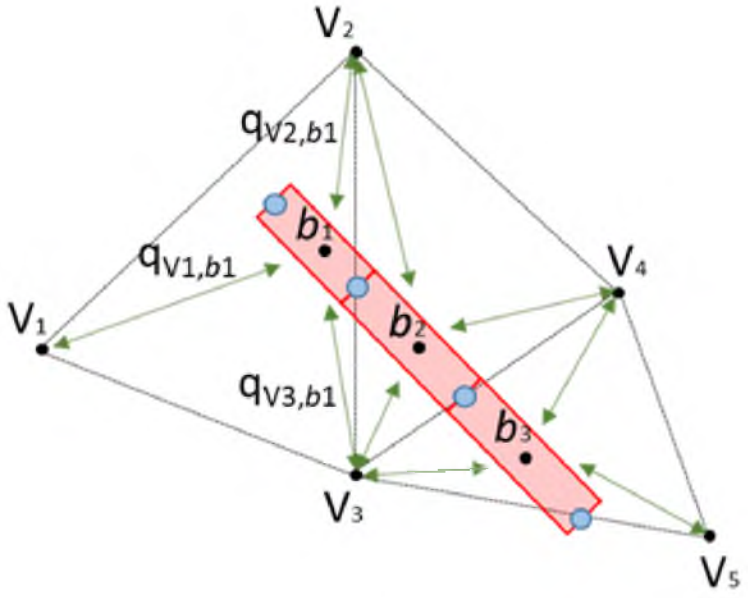

Figure 4.18 Representation of matrix nodes and fracture blocks interactions

$$q_{MF,b_i} = -\sum_{n=1}^{3} q_{V_n,b_i} \tag{4.58}$$

In this framework, the flux between fracture grid blocks and triangular nodes is defined by a two-point flux scheme by projection. We start by defining points: $= V_1(\mathrm{x},\mathrm{y})$, $B = b_1(\mathrm{x},\mathrm{y})$ and vector $\overrightarrow{CD}$ such that $\overline{AB}|\overrightarrow{CD}$ as shown in an example in **Figure 4.19**. Letting vertices M, N, O, P define quadrilateral b_1 then $\overline{MN}|\overline{OP}$ follows as per definition. Applying the dot product, a projection of fracture grid block b_1 onto $\overrightarrow{CD}$ (which is orthogonal to the flux direction between matrix node V_1 and fracture block b_1) is obtained:

$$proj_{\overrightarrow{CD}}\overline{MN} = \frac{\overrightarrow{MN}\cdot\overline{CD}}{|\overline{CD}|^2}\overline{CD} \tag{4.59}$$

$$proj_{\overrightarrow{CD}}\overline{OP} = \frac{\overrightarrow{OP}\cdot\overline{CD}}{|\overline{CD}|^2}\overline{CD}$$

Lengths are obtained as follows:

$$L_{V_1,b_1} = \left|proj_{\overrightarrow{CD}}\overline{MN}\right| + \left|proj_{\overrightarrow{CD}}\overline{OP}\right| = \frac{|\overrightarrow{MN}\cdot\overline{CD}|}{|\overline{CD}|} + \frac{|\overrightarrow{OP}\cdot\overline{CD}|}{|\overline{CD}|} \tag{4.60}$$

Then, the matrix-fracture flux for matrix node V_1 and fracture block b_1 can be defined as follows:

$$q_{l,V_n,b_i} = \frac{\alpha}{B_l}\left[T_{V_n,b_i}(\Phi_{l,V_n} - \Phi_{l,b_i})\right] \tag{4.61}$$

where the transmissibility term is defined as:

$$T_{V_n,b_i} = \frac{\mathbf{k}^{\boldsymbol{mf}} L_{V_n,b_i}}{|\overline{AB}|} \tag{4.62}$$

and permeability is defined as a harmonic average:

$$\mathbf{k}^{\boldsymbol{mf}} = \frac{2}{\frac{1}{\mathbf{k}^{\boldsymbol{m}}} + \frac{1}{\mathbf{k}^{\boldsymbol{f}}}} \tag{4.63}$$

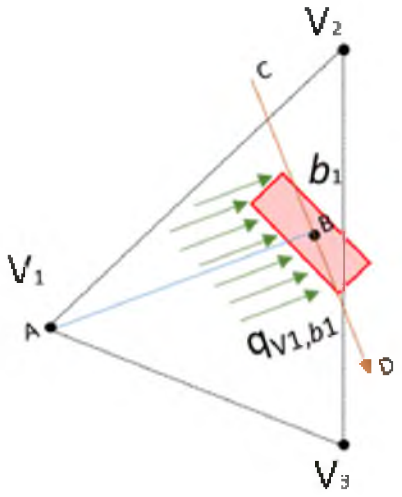

Figure 4.19 Flux from a matrix node onto a fracture grid block

Equations governing matrix-fracture and fracture-fracture flow are fully defined. The last term of equation 4.53 (q_{well}) which refers to well model flux is discussed next.

4.3.6 Well Model

The influence of a well in a simulation model is represented by a point source or a line source which consists of a series of connected point sources as shown in **Figure 4.20**. For injectors or producers, the flow exchange for a particular fluid phase in the reservoir is determined by equation 4.64:

$$q_{well,l,i} = WI_i \gamma_i (P_{well,l,i} - P_{l,i}) \tag{4.64}$$

where WI_i is the well index which is dependent on the discretization scheme and γ_i can be calculated using a downstream weighting scheme for injectors:

$$\gamma_i = \rho_{well,l,i} \mathrm{f}_p \left(\sum_{j=1}^{p} \frac{k_{rj}}{\mu_j} \right)_i \tag{4.65}$$

where p is the number of phases and $\mathrm{f}_p$is the volumetric fraction of phase l. For producers,

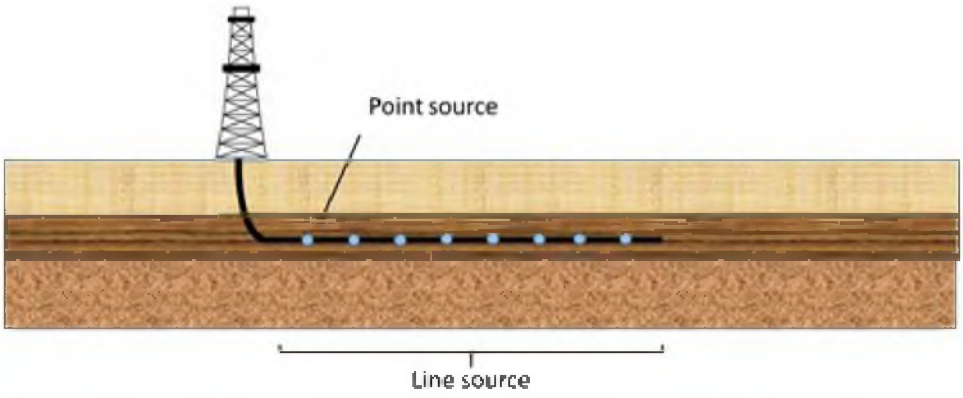

Figure 4.20 Well model representation in a simulation model

an upstream weighting scheme is used:

$$\gamma_i = \left(\rho_l \frac{k_{rl}}{\mu_l}\right)_i \tag{4.66}$$

Letting Np be the total number of point sources defined by $q_{well,l,i}$, a line source is the defined as:

$$q_{well,l} = \sum_{j=1}^{Np} q_{well,l,j} \tag{4.67}$$

when dealing with line sources, pressure drop along the wellbore due to gravitational and viscous forces need to be considered.[101-102] In this framework only gravitational forces due to hydrostatic pressure are considered.

4.3.6.1 Well Index

Well index as discussed in the previous section is determined depending on the discretization method used. Peaceman (1983)[103] introduced a well index expression that links the radius of the wellbore to the effective grid block radius where the well perforation is hosted.

$$WI_i = \frac{2\pi h k_{wb} f_h f}{ln\frac{r_{eff}}{r_{wb}} + S} \tag{4.68}$$

The effective radius, r_{eff}, is defined by the discretization method and the orientation of the well model. For a vertically oriented well that intersects a grid-block, the effective radius can be calculated for the finite difference method as:

$$r_{eff} = \frac{2\sqrt{\sqrt{k_{yy}/k_{xx}}\,\Delta x^2 + \sqrt{k_{xx}/k_{yy}}\,\Delta y^2}}{\sqrt{\pi}\left(\sqrt[4]{k_{yy}/k_{xx}} + \sqrt[4]{k_{xx}/k_{yy}}\right)} \tag{4.69}$$

For a two-dimensional CVFE discretization scheme, the effective radius can be calculated as follows:

$$r_{eff} = \sqrt{A_{cv}/\pi} \tag{4.70}$$

A visual representation of these two effective radii is shown in **Figure 4.21**.

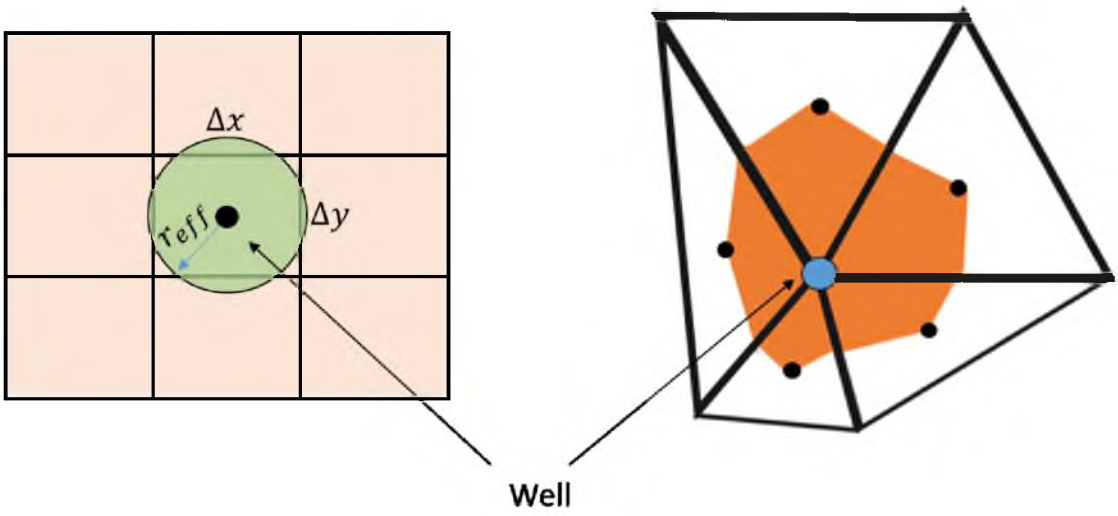

Figure 4.21 Well representation for a Cartesian grid (left) and triangular-element grid (right)

4.4 Verification Studies

Verification serves as a quality control tool used to assess and evaluate a model's representation of reality. This process reassures that a model solves the correct equations and represents physical phenomena properly. Depending on the problem at hand, there are several approaches to verification of numerical simulation including:

1. Indexing Method

   This is the most common verification methodology in reservoir engineering to assess a new simulator. The method verifies a new simulator by simply comparing its results to a particular problem to the results of an already well established simulator. Even though this is a strong and well accepted method, problems arise as simulators based on different discretization techniques are compared. For instance, control volumes that result from most traditional simulators are based on a block-centered finite difference scheme. Control volumes that result from a triangular finite-element method are not comparable to the cubic geometry of a block-centered grid geometry. In consequence, a rigorous comparison of the results and numerical performance between two different types of simulators is very difficult.

   Despite this problem, the indexing method can, to an extent, be used to compare results and physical behavior of a complex system.

2. Analytical Solution Method

   In this method, results from a newly developed simulator are compared to results from an analytical expression. Problems of this nature tend to be simple as they have several assumptions.

3. Method of Manufactured Solutions

   The code verification method of manufactured solutions works by addition of a manufactured solution function that satisfies initial and boundary conditions. By substituting in governing equations, a solution function seeks to find a source function. This source function is then found by treating it as a well producer or injector. A successful case results from the simulator converging to the manufactured solution. This process is well established in the fields of mathematics and computational fluid dynamics.

For the present work, verification studies are done by application of the indexing method and by comparison with an analytical solution.

4.4.1 Finite-Conductivity Fracture Behavior

A mathematical model that studies the behavior of a fully penetrating finite-conductivity vertical fracture was studied by Cinco-Ley et al. (1978).[60] They derived fracture pressure drop and matrix-fracture flux expressions through the use of dimensionless analysis. In this instance, their analytical expressions are compared to the simulation results from the newly developed implementation of the DFM. This was done before to verify the flow equations for the current DFM implmentation.[93] The problem consists of an isotropic and homogenous reservoir with a fully penetrating finite-conductivity vertical fracture that connects the well to the reservoir as shown in **Figure 4.22**.

As mentioned earlier, analytical formulations are limited by the assumptions made for their derivations. Here, important assumptions include laminar flow and negligible gravity

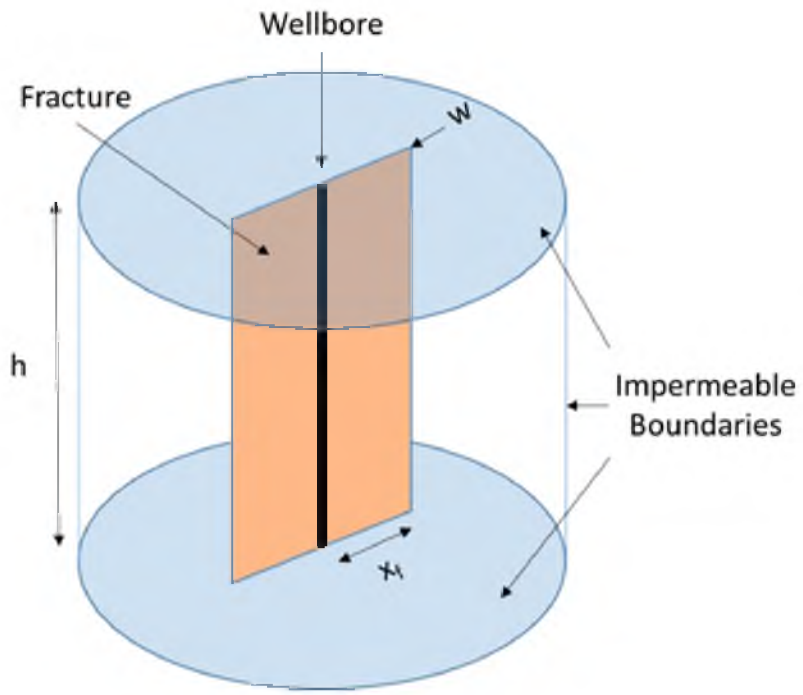

Figure 4.22 Finite-conductivity fracture system

effects for a one-phase slightly incompressible fluid flowing into the fracture first and then to the well. Based on these assumptions, the solution to this system can be split into two equations that govern both fracture and matrix fluid transport.

The fracture expression is shown below:

$$\frac{\partial^2 P_f}{\partial x^2} + \frac{\mu q_f(x,t)}{k_f wh} = \frac{\phi_f \mu c_t}{k_f}\frac{\partial P_f}{\partial t} \qquad 4.71$$

where the initial condition is:

$P_f(x, t = 0) = P_i$ for $0 \leq x \leq x_f$

and boundary conditions:

$$\frac{\partial P_f}{\partial x} = -\frac{\mu q_w}{2k_f wh} \; @x = 0$$

$$\frac{\partial P_f}{\partial x} = 0 \; @x = x_f$$

Similarly, the matrix expression is shown below:

$$\frac{\partial^2 P}{\partial x^2} + \frac{\partial^2 P}{\partial y^2} = \frac{\phi \mu c_t}{k} \frac{\partial P}{\partial t} \qquad 4.72$$

with the initial condition:

$$P(x, y, t = 0) = P_i$$

and boundary conditions:

$$P(x, y, = 0, t) = P_f(x, t) \text{ for } 0 \leq x \leq x_f$$

$$q(x, y = 0, t) = P_f(x, t) \text{ for } 0 \leq x \leq x_f$$

where q and P are flux and pressure measured at the reservoir domain; q_f and P_f are flux and pressures measured within the fracture domain. **Figure 4.23** illustrates the fracture-matrix fluid flow dynamics for this problem.

The solution as presented by Cinco-Ley et al. (1978)[60] is defined with dimensionless variables. Assuming that total compressibility is the same throughout the system, these are presented as follows:

Dimensionless distance:

$$x_D = \frac{x}{x_f}$$

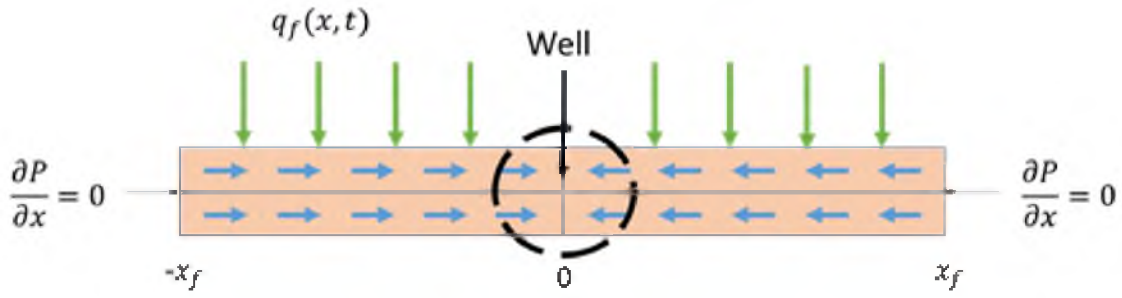

Figure 4.23 Fracture fluid flow model

$$y_D = \frac{y}{x_f}$$

Dimensionless time:

$$t_D = \frac{0.000264kt}{\phi\mu c_t {x_f}^2}$$

Dimensionless fracture hydraulic diffusivity:

$$n_{fD} = \frac{k_f \phi}{\phi_f k}$$

Dimensionless fracture storage capacity:

$$C_{fDf} = \frac{w\phi_f}{\pi x_f \phi}$$

Dimensionless fracture conductivity:

$$C_{fD} = C_{fDf} n_{fD} = \frac{wk_f}{\pi x_f k}$$

Dimensionless pressure drop:

$$P_{fD} = \frac{kh\left(P_i - P_f(x,t)\right)}{141.2qB\mu}$$

$$P_D = \frac{kh(P_i - P(x,y,t))}{141.2qB\mu}$$

Dimensionless flux:

$$q_{fD} = \frac{2q_f(x,t)x_f}{q}$$

$$q_D = \frac{2q(x,t)x_f}{q}$$

With all concerning dimensionless variables defined, the solution to equation 4.71 is given as:

$$P_{fD}(x_D,t_D)=\frac{x_f}{w}\sqrt{\frac{k\phi\pi}{k_f\phi_f}}\sum_{n=-\infty}^{\infty}\int_o^{t_D}\left(\frac{e^{-\frac{(x_D-2n)^2}{4(k_f\phi/\phi_f k)}}}{\sqrt{\tau}}\right.$$

$$\left.-\int_{2n-1}^{2n+1}q_{fD}(\chi,\tau)\frac{e^{-\frac{(x_D-\chi)^2}{4(k_f\phi/\phi_f k)}}}{2\sqrt{t_D-\tau}}d\chi\right)d\tau \qquad 4.73$$

The dimensionless pressure drop for the reservoir domain can be obtained by:

$$P_D(x_D,y_D,t_D)=\frac{1}{4}\int_o^{t_D}\int_{-1}^{1}q_D(\chi,\tau)\frac{e^{-\frac{(x_D-\chi)^2+y_D{}^2}{4(t_D-\tau)}}}{t_D-\tau}d\chi\,d\tau \qquad 4.74$$

To solve this problem, the expressions for the fracture and reservoir domain must be combined. In other words, dimensionless pressures and fluxes for both domains must be the same on the fracture-reservoir plane:

$$P_{fD}(x_D,t_D)=P_D(x_D,y_D,t_D)$$

And,

$$q_{fD}(x_D,t_D)=q_D(x_D,t_D)$$

For $-1\le x_D\le 1$ and $t_D>0$

A combination of equations 4.73 and 4.74 and use of Poisson's summation formula with the above fracture-reservoir relations yields:

$$\frac{1}{4}\int_o^{t_D}q_D(\chi,\tau)\frac{e^{-\frac{(x_D-\chi)^2}{4(t_D-\tau)}}}{t_D-\tau}d\chi d\tau$$

$$=\frac{1}{C_{fDf}}\left(t_D+\frac{2}{\pi^2 n_{fD}}\sum_{n=1}^{\infty}\frac{\cos(n\pi x_D)}{n^2}\left(1-e^{-n_{fD}n^2\pi^2 t_D}\right)\right) \qquad 4.75$$

$$-\frac{1}{C_{fDf}}\int_o^{t_D}\int_{-1}^{1}q_D(\chi,\tau)\left(\frac{1}{2}+\sum_{n=1}^{\infty}\cos(n\pi)\,(x_D-\chi)e^{-n_{fD}n^2\pi^2(t_D-\tau)}\right)d\chi\,d\tau$$

This equation is solved using Green's method. The resulting analytical solution can be used to verify output from the newly developed DFM implementation. A fully implicit

two-dimensional one-phase model was developed to study pressure drop along the fracture and reservoir-to-fracture flux. Key parameters for the studied simulation model are reported in **Table 4.1**.

The simulation was run for 10 and 20 fracture segments to study the effect of course fracture gridding. First, dimensionless pressure drop along the half length of the fracture was used as a comparison basis. **Figure 4.24** shows the comparison between simulation and Cinco-Ley's expressions for a 10-segment fracture model and fracture dimensionless conductivities of 0.2, 1, 2, and 10. The match is fairly decent with some noticeable gaps as dimensionless distance approaches zero. As shown by Cinco-Ley et al., pressure drop along the fracture is essentially zero when conductivities are in the order of 10.

Figure 4.25 shows the comparison for a 20-segment fracture model. Here, a very good agreement is found between simulation results and analytical results. A pressure distribution map as determined by simulation for an arbitrary production time is shown in **Figure 4.26**.

Dimensionless flux entering the fracture from the reservoir rock was also used as a comparison basis for conductivities of 0.2, 1, 2, and 10 as shown in **Figure 4.27**. Again, a good agreement was found for all dimensionless conductivities studied. Better matches would only be possible by refining the simulation model's grid configuration and fracture segmentation.

As shown by comparison of analytical and simulation results of a finite-conductivity fully penetrating fracture intersecting a vertical well, the newly developed DFM implementation is verified.

Table 4.1 Simulation key parameters

Reservoir Area (ft-ft):	500*500
Matrix Permeability (mD):	0.1
Porosity (%):	20
Total compressibility (psi^{-1}):	$6X10^{-6}$
Fluid viscosity (cp):	0.31
Initial Reservoir Pressure (psi):	4500
Flowing Bottom hole Pressure (psi):	2400
Fracture half length (ft):	70
Fracture conductivity (ft-mD)	4.4 to 220
Reservoir thickness (ft)	100
Constant Production Rate (bbl/day)	18

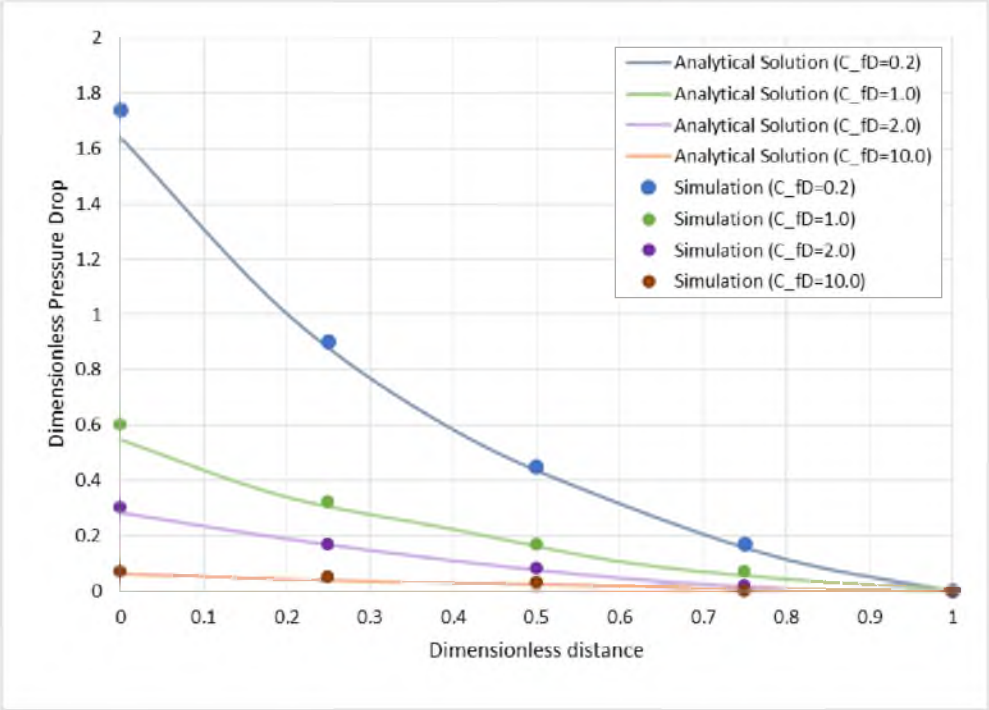

Figure 4.24 Analytical and simulation pressure drop results for a 10-segment fracture

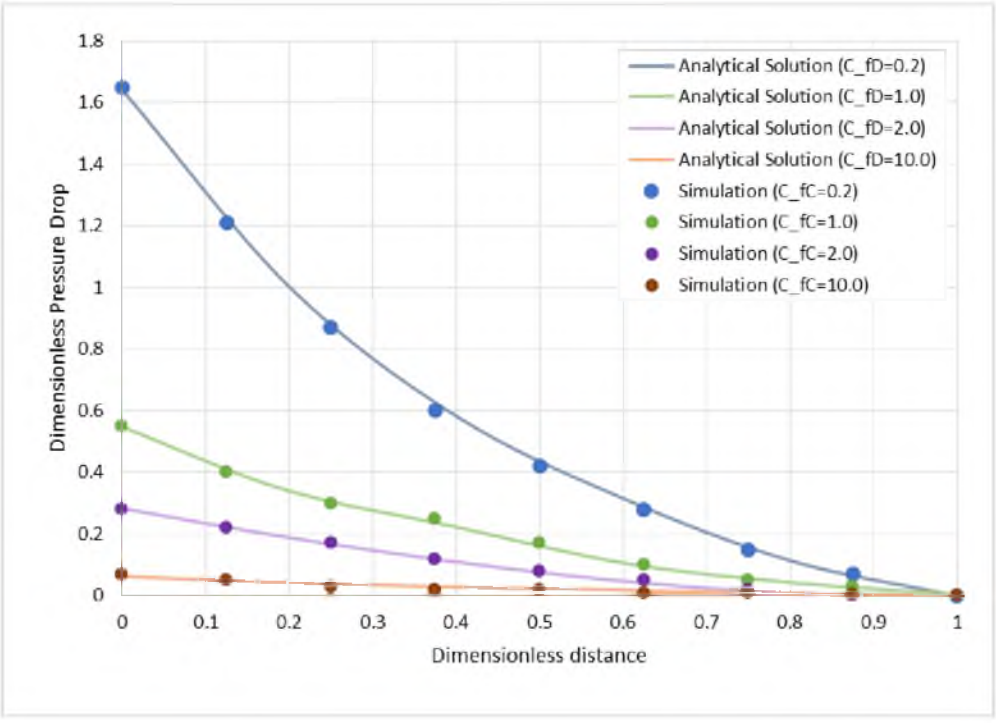

Figure 4.25 Analytical and simulation pressure drop results for a 20-segment fracture

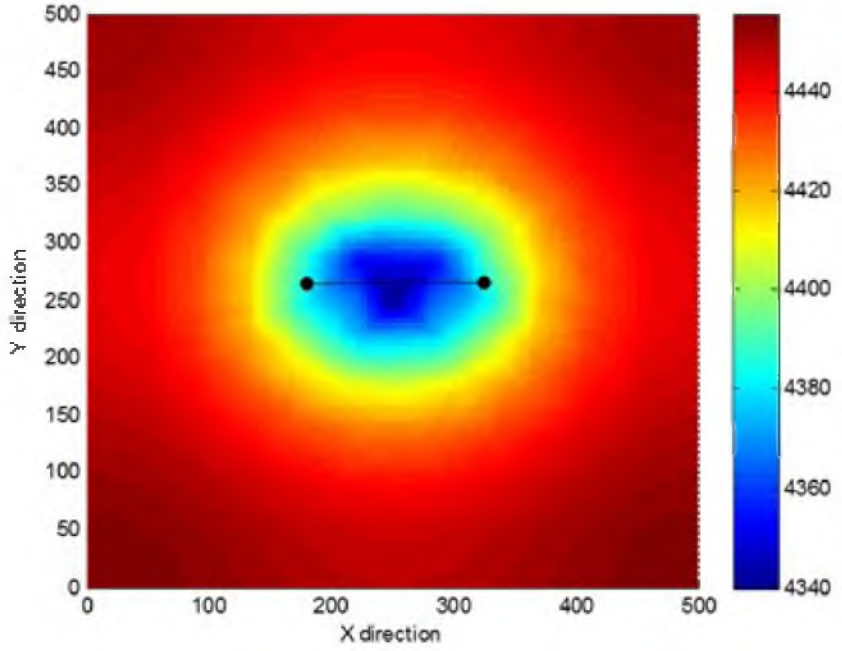

Figure 4.26 Areal simulation pressure distribution for the system

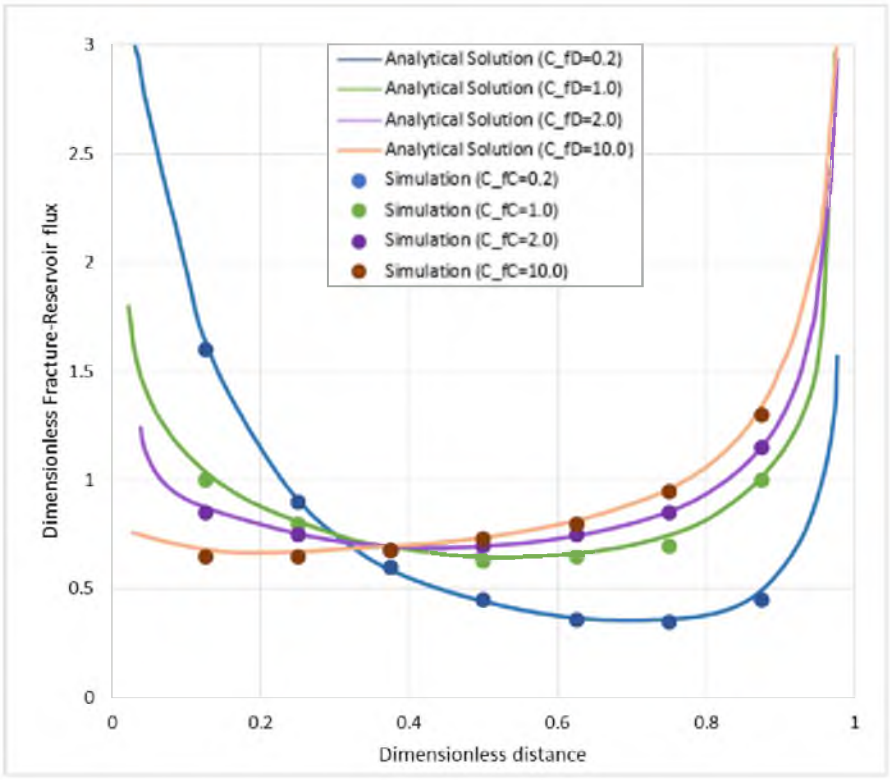

Figure 4.27 Analytical and simulation dimensionless flux results for a 20-segment fracture

4.4.2 Multistage and Multiwell Problem

In this section, a more complicated problem is used to validate the new DFM implementation in this research work. In Chapter 3, a multistage multiwell simplified model example was presented where fracture elements 1, 2, 3, and 4 were representatives of interior and exterior fractures for interior and exterior wells. A similar simulation is considered with all four fracture representative elements with simulation information listed in **Table 3.1** with bottom-hole pressure running at 2400 psi. Reservoir dimensions are shown in **Figure 3.7**. As a reference, the simplified model schematic is shown in **Figure 4.28**.

Oil rates from fracture elements 1, 2, 3, and 4 for a CMG simulation model and the new DFM are shown in **Figure 4.29**. Even though there are some noticeable differences in rates, the agreement in results is decent for two simulation programs working on different algorithms. Because of this, simulation run times are not a good comparison and are not presented here.

4.5 Key Findings

A new discrete fracture model was implemented into a control-volume finite element simulator. This new implementation is loosely based on the current discrete fracture model as developed by others.[55,87,89] The main advantage of this implementation include the fact that fractures are granted their own control volumes and that they can be manipulated independently of matrix gridding configurations. Transmissibility functions between matrix and fracture nodes are treated based on the fact that they operate in different spaces. This method gives rise to several approaches to fracture-matrix flux computations. In this

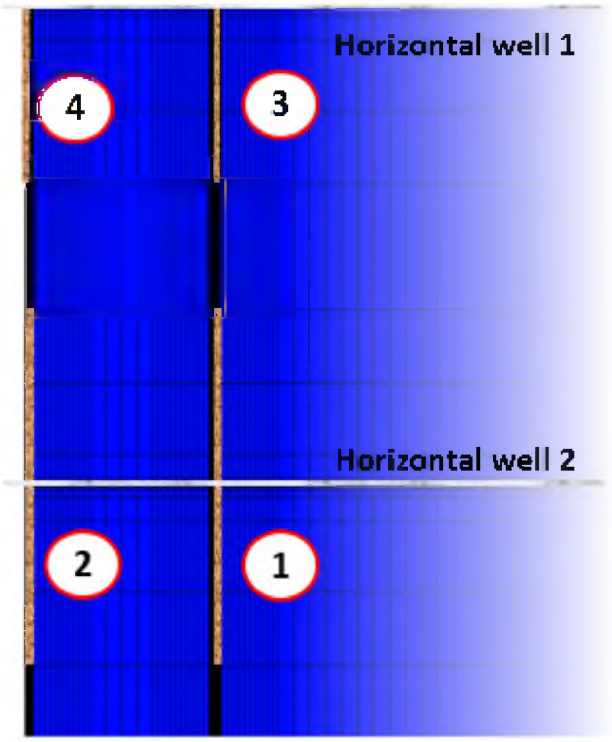

Figure 4.28 Simplified multi-stage multi-well simulation model

research work, a two-point flux formulation with a projection approach was used to keep the model simple.

Verification studies using analytical expressions and the indexing method were performed. The verification was only limited to comparison of results to assure that the right physics were represented in this new implementation. Performance studies were ignored since the aim of this research work was to present a new and more robust fracture representation.

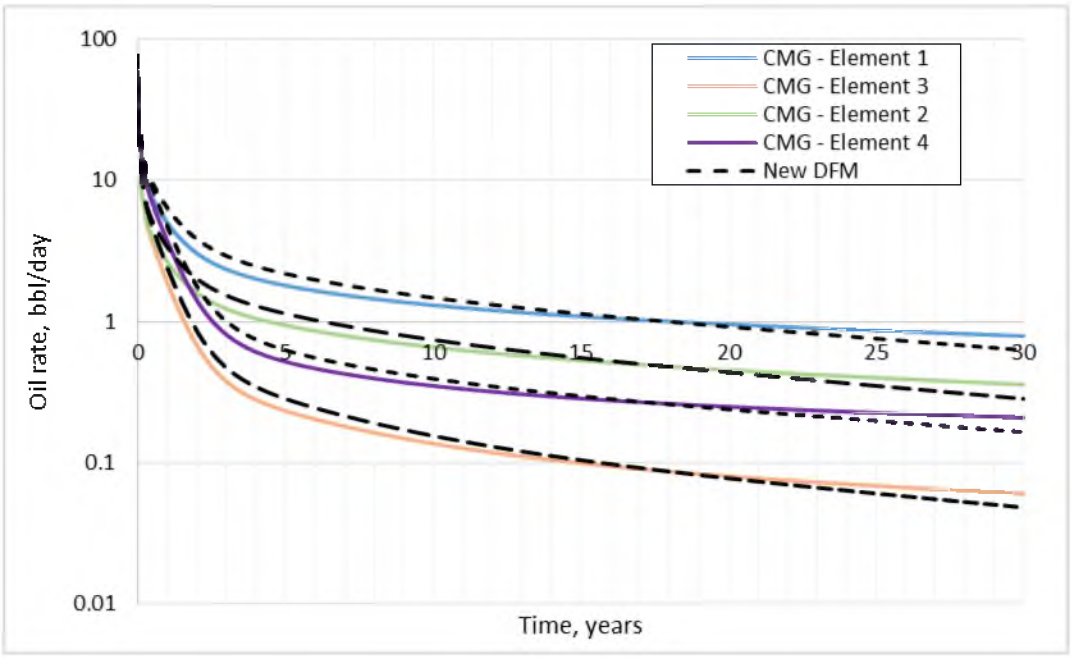

Figure 4.29 Simulation results comparison

CHAPTER 5

SUMMARY

5.1 Original Contributions

The following original contributions were made as a result of proposed research objectives:

1. **Development of an analytical technique to help quickly and easily identify essential reservoir and fluid properties.**

   A semi-analytical method based on conventional material balance was developed to identify pressure behavior in a transient system. Important reservoir information such as diffusivity, pressure, and average reservoir pressure decline are possible from this method. A correcting average pressure factor was introduced for gas reservoirs, thus expanding the applicability of this method to any type of fluid and flow geometry.

2. **Elaboration of a standard reservoir simulation modeling workflow for unconventional reservoirs.**

   A standard workflow was introduced to help the simulation engineer build a simplified simulation model that dramatically reduces run time without sacrificing accuracy. Popular simplified models such as the 'single fracture' approach were shown to have substantial accuracy flaws, especially for multi-

stage and multiwell projects. Simplified models that result from the application of the presented workflow retain the low simulation run times from the 'single fracture' model and achieve results successfully matching those of full-scale simulation. Besides a couple of application examples that were presented, a spacing study and economic analysis were performed with a total simulation run time of less than a day.

3. **Development of a new discrete fracture model for implementation in a control volume finite element method simulator.**

   A new discrete fracture model independent of matrix gridding that accounts for fracture flow and storage was developed and verified. A discretization technique that provides fracture with freedom to be placed anywhere in a matrix medium was introduced by deriving 2-point flux transmissibility calculations for matrix-fracture interactions. Fracture-fracture fluid flow is obtained through traditional discretization schemes. Comparison of simulation results with an analytical solution and application of the indexing method provided verification for the new implementation.

5.2 Recommendations for Future Work

Recommendation for future research work are made based on the different research topics presented here:

1. **Material balance applied to tight formations.**

   Future work on the material balance formulation can be done in sensitivity studies, particularly of fracture conductivity and reservoir heterogeneity.

Reservoir performance analytics based on diffusivity/permeability versus time relationship can be further developed and studied using field data. Post-transient stage applications can also be implemented in the current methodology for a comprehensive tool.

2. **Reservoir simulation simplification workflow for hydraulically fractured reservoirs.**

   In this topic, case studies can be performed to different well and fracture configurations. Even though this study was particularly aimed to hydraulically fractured reservoirs, its applications can be made to any simulation model by adjusting the solution process diagram and expanding symmetric and multiplier factor calculations. Expansion of this workflow can be shown by accounting for reservoir compartmentalization and heterogeneity.

3. **A new discrete fracture implementation**

   Implementation of this framework to a 2.5- or 3-dimensional model is the next step. Other phenomena such as geochemistry can be implemented to this framework in the form of a module. Of special interest is the application of a geomechanical implementation to study the behavior of fracture morphology and property changes as fluid is withdrawn from a reservoir. Other work such as capillary pressure contrast studies in a matrix-fracture context would add to the overall application of this new discrete fracture implementation.

APPENDIX A

RESERVOIR ROCK AND FLUID PROPERTIES

A.1 Porosity

Porosity is defined as the ratio of pore volume and bulk volume as mathematically shown below:

$$\varphi = \frac{V_{pore}}{V_{bulk}} \tag{A.1}$$

Because porosity is a function of volume, it is dependent on rock compressibility. One relation that approximates porosity based on formation compressibility and pressure drop can be defined as:

$$\varphi(P) = \varphi_{ref}(1 + C_f(P - P_{ref})) \tag{A.2}$$

Where porosity is a function of formation compressibility, reference porosity, and reference pressure. Reference data is measured for particular rock formations and is generally taken as a user input in commercial simulators.

A.2 Permeability

Permeability is a rock property that measures the ease of flow through rock porous media. Darcy's law describe porous medium flow as strongly dependent on permeability as shown in equation A.3.

$$\mathbf{v} = -\frac{\mathbf{k}}{\mu}\nabla\Phi \tag{A.3}$$

Where **v** is Darcy velocity.

Mathematically, permeability is defined as a positive-definite tensor in a three-dimensional space.[104]

$$\mathbf{k} = \begin{bmatrix} k_{xx} & k_{xy} & k_{xz} \\ k_{xy} & k_{yy} & k_{yz} \\ k_{xz} & k_{yz} & k_{zz} \end{bmatrix} \tag{A.4}$$

A.3 Phase Saturation

In multiphase flow problems, multiple types of fluid are present in the porous space of a rock medium. Analogous to the porosity concept, fluid saturation is defined as the ratio of fluid saturation and pore volume as shown in equation A.5:

$$S_l = \frac{V_l}{V_{pore}} \tag{A.5}$$

Volume conservation then dictates that the sum of all fluid saturations is always unity:

$$\sum_{l=1}^{n} S_l = 1 \tag{A.6}$$

A.4 Phase Pressure and Potential

Potential accounts for the hydrostatic pressure that acts upon fluids in a porous medium can be calculated as:

$$\Phi_l = P_l + \rho_l \frac{g}{g_c} z \tag{A.7}$$

Where ρ_l is phase density, g is the gravitational constant, g_c is a universal gravitational conversion constant and z is the depth.

A.5 Capillary Pressure

Capillary pressure is defined as an interfacial pressure difference between two immiscible fluids as shown below:

$$P_c = P_n - P_w \tag{A.8}$$

Where *n* and *w* denote nonwetting and wetting phases, respectively. This denomination is given to fluids to differentiate their abilities to maintain contact with the solid rock surface.

In general, capillary pressures are functions of the wetting phase saturation, and tabulated data obtained from correlations or lab measurements are input for most commercial simulators.

A.6 Relative Permeability

To account for simultaneous multiphase flow, the relative permeability concept was created and implemented into Darcy's law. The effective permeability at which a particular fluid phase flows is dependent on its saturation as shown below:

$$\mathbf{k}_{eff} = \mathbf{k}k_{rl}(S_l) \tag{A.9}$$

By combining Darcy's law and equation A.9, the multiphase Darcy velocity is defined as:

$$\mathbf{v}_l = -\frac{\mathbf{k}k_{rl}}{\mu_l}\nabla\Phi_l \tag{A.10}$$

Where the subscript *l* denotes an individual phase and the relative permeability of such phase, k_{rl}, is a function of phase saturation.

A.7 Formation Volume Factor

Formation volume factor of a fluid phase is the ratio of fluid volume at reservoir conditions and fluid volume at standard conditions. Due to the compressibility of some fluid phases, these factors have varying degrees of pressure dependency. Formation volume factors are defined for oil, water, and gas as follows:

$$\text{Oil:} \quad B_o(P_o) = \frac{V_{o,RC} + V_{dg,RC}}{V_{o,STC}} = \frac{\rho_{o,STC} + R_s\rho_{g,STC}}{\rho_{o,RC}},$$

$$\text{Water:} \quad B_w(P_w) = \frac{V_{w,RC}}{V_{w,STC}} = \frac{\rho_{w,STC}}{\rho_{w,RC}}, \qquad \text{A.11}$$

$$\text{Gas:} \quad B_g(P_g) = \frac{V_{g,RC}}{V_{g,STC}} = \frac{\rho_{g,STC}}{\rho_{g,RC}}.$$

APPENDIX B

CONVENTIONAL MATERIAL BALANCE

B.1 Conventional Oil Material Balance

The conventional oil material balance equation is regarded as one of the core tools for reservoir engineers. This equation gives important insights into reservoir performance and potential for forecasting in conventional reservoirs. The mechanisms that drive fluid flow in a tank-like system are listed below:

a) Expansion of oil and dissolved gas

b) Expansion of originally free gas (gascap gas)

c) Connate water expansion and pore volume reduction

d) Underground withdrawal

e) Water influx

The contributions of these mechanisms can be combined to bring forth the material balance equation in its original form as shown in equation B.1.

$$N_P\left(B_o + (R_P - R_s)B_g\right) = NB_{oi}\left[\frac{(B_o - B_{oi}) + (R_{si} - R_S)B_g}{B_{oi}} + m\left(\frac{B_g}{B_{gi}} - 1\right) + (1 + m)\left(\frac{C_w S_{wc} + C_f}{1 - S_{wc}}\right)\Delta P\right] + (W_e + W_p)B_w \quad \text{B.1}$$

Where all parameters can be found in the nomenclature.

Similarly, the material balance equation for dry gas reservoirs is expressed as:

$$\left(\frac{P}{Z}\right) = \left(\frac{P}{Z}\right)_i \left(1 - \frac{G_p}{G}\right) \qquad \text{B.2}$$

There are multiple manipulations and forms of the material balance equation to help identify driving mechanisms, initial hydrocarbon in place, and ultimate recovery. Even though these solutions have been somewhat replaced by numerical simulation, they still are tremendously useful to perform quick calculations and to help engineers understand reservoir behavior.

APPENDIX C

GOODNESS OF FIT

C.1 Normalized Root Mean Square Error (NRMSE):

The Root Mean Square Error (RMSE), also known as the root mean square deviation (RMSD), is used to measure the total residuals of modeled values and observed values.

The RMSE is defined as the square root of the mean squared error:

$$RMSE = \sqrt{\frac{\sum_{i=1}^{n}\left(Y_{obs,i} - Y_{model,i}\right)^2}{N}} \quad \text{C.1}$$

Where Y_{obs} is observed values and Y_{model} is modeled values.

It is sometimes difficult to analyze the error in terms of absolute values because different outcomes vary in their absolute values, ranges, and units. Nondimensional forms of the RMSE are required to compare RMSE for different units and outcomes. The RMSE is normalized by dividing by the range of the observed data to get NRMSE (Normalized Root Mean Square Error)

$$NRMSE = \frac{RMSE}{Y_{obs,max} - Y_{obs,min}} \quad \text{C.2}$$

Where, $Y_{obs,max}$ is the maximum value of observed data and $Y_{obs,min}$ is the minimum value of observed data. The NRMSE may be expressed in term of percentage by multiplying by 100. The smaller percentage values indicate the better fit of the model curve

with observed data.

C.2 Average absolute relative error (AARE)

This is the direct measurement of total relative errors. Absolute values of errors are generally used to prevent the nullification of errors when adding positive and negative deviations. Another feature of AARE is that it does not consider absolute value of errors but calculates error relative to the actual value, in other terms, error is normalized by its actual value. The calculation method is shown in equation C3:

$$AARE = \frac{1}{N}\sum_{i=1}^{N}\left|\frac{Y_{obs,i} - Y_{model,i}}{Y_{obs,i}}\right| \quad \text{C.3}$$

APPENDIX D

ECONOMIC ANALYSIS

D.1 Net Present Value

The NPV is defined as a factor that reflects the degree to which cash inflow compares to the capital investment of a project. The use of NPV is handy when comparing projects with different costs and cash inflows as it determines relative profitability. Naturally, the higher the NPV, the better. Mathematically, NPV is defined as follows:

$$NPV = \sum_{t=1}^{T} \frac{C_t}{(1+r)^t} - C_o \qquad \text{D.1}$$

Where, Ct is the net cash inflow during period t, Co is the total capital cost, r is the discount rate, and t is the number of time periods.

REFERENCES

1. *Annual Energy Outlook 2012*; U.S. Energy Information Administration: Washington, DC, 2012.

2. *Review of the Emerging Resources 2011*; U.S. Energy Information Administration: Washington, DC, 2011.

3. Sieminski, A. In *International Energy Outlook*, Deloitte Oil and Gas Conference, Houston, Texas, USA, Nov 18, 2014.

4. Schilthuis, R. J. Active Oil and Reservoir Energy. *Trans. AIME.* **1936,** *118* (01), 33-52.

5. Havlena, D.; Odeh, A. The Material Balance as an Equation of a Straight Line. *JPT* **1963,** *15* (08), 896-900.

6. Pickup, G. E.; Christie, M. A. Top-Down Reservoir Modelling: From Material Balance to Reservoir Simulation. *SPE.* **2009**.

7. Walsh, M.; Ansah, J.; Raghavan, R. In *The New, Generalized Material Balance as an Equation of a Straight Line: Part 1-Applications to Undersaturated, Volumetric Reservoirs*, Permian Basin Oil and Gas Recovery Conference, Midland, Texas, USA, Mar 16-18, 1994; Society of Petroleum Engineers: Midland, Texas, USA, 1994.

8. Penuela, G.; Idrobo, E. A.; Ordonez, A.; Medina, C. E.; Meza, N. S. In *A new Material-Balance Equation for Naturally Fractured Reservoirs Using a Dual-System Approach*, SPE Western Regional Meeting, Bakersfield, California, USA, Mar 26-30, 2001; Society of Petroleum Engineers: Bakersfield, California, USA, 2001.

9. Niz, E.; Idrobo, E. A.; Peñuela, G.; Ordóñez, A.; Calderón, Z. H. Ecuación de Balance de Materia para Sistemas de Doble Porosidad con Capa de Gas Inicial. *CTF.* **2004,** *2* (5), 97-115.

10. Sandoval, P.; Calderon, Z.; Ordonez, A. In *The New, Generalized Material Balance Equation for Naturally Fractured Reservoirs*, Latin American and Caribbean Petroleum Engineering Conference, Cartagena de Indias, Columbia, May 31 - Jun 3, 2009; Society of Petroleum Engineers: Cartagena de Indias, Colombia, 2009.

11. Ojo, K.; Osisanya, S. In *Material Balance Revisited*, Nigeria Annual International Conference and Exhibition, Abuja, Nigeria, Jul 31 - Aug 2, 2006; Society of Petroleum

Engineers: Abuja, Nigeria, 2006.

12. McNeil, R. In *The "Flowing" Material Balance Procedure*, Annual Technical Meeting, Calgary, Alberta, Canada, Jun 7-9, 1995; Petroleum Society of Canada: Calgary, Alberta, Canada, 1995.

13. Mattar, L.; McNeil, R. The "Flowing" Gas Material Balance. *Journal of Canadian Petroleum Technology.* **1998,** *37* (02).

14. Kanu, A. U.; Obi, O. M. In *Advancement in Material Balance Analysis*, SPE Nigeria Annual International Conference and Exhibition, Lagos, Nigeria, Aug 5-7, 2014; Society of Petroleum Engineers: Lagos, Nigeria, 2014.

15. Nobakht, M.; Clarkson, C. R. In *A New Analytical Method for Analyzing Production Data from Shale Gas Reservoirs Exhibiting Linear Flow: Constant Rate Production*, North American Unconventional Gas Conference and Exhibition, The Woodlands, Texas, USA, Jun 14-16, 2011; Society of Petroleum Engineers: The Woodlands, Texas, USA, 2011.

16. Katz, D. L. V. *Handbook of Natural Gas Engineering*; McGraw-Hill: New York, 1959.

17. Miller, F. G. Theory of Unsteady-State Influx of Water in Linear Reservoirs. *J. Inst. Pet.* **1962,** *48* (467), 365-379.

18. Dake, L. P. *Fundamentals of Reservoir Engineering*; Elsevier Scientific Pub. Co.: New York, 1978.

19. Bird, R. B.; Stewart, W. E.; Lightfoot, E. N. *Transport Phenomena*; Wiley: New York, 1960.

20. Mattax, C. C.; Dalton, R. L. Reservoir Simulation. *JPT.* **1990,** *42* (06), 692-695.

21. Chaudhary, A. S. Shale Oil Production Performance from a Stimulated Reservoir Volume. M.Sc. Thesis, Texas A&M University, August 2011.

22. Qanbari, F.; Clarkson, C. In *Production Data Analysis of Multi-Fractured Horizontal Wells Producing from Tight Oil Reservoirs–Bounded Stimulated Reservoir Volume*, SPE/EAGE European Unconventional Resources Conference and Exhibition, Vienna, Austria, Feb 25-27, 2014; Society of Petroleum Engineers: Vienna, Austria, 2014.

23. Wan, T.; Meng, X.; Sheng, J. J.; Watson, M. In *Compositional Modeling of EOR Process in Stimulated Shale Oil Reservoirs by Cyclic Gas Injection*, SPE Improved Oil Recovery Symposium, Tulsa, Oklahoma, USA, Apr 12-16, 2014; Society of Petroleum Engineers: Tulsa, Oklahoma, USA, 2014.

24. Patwardhan, S. D.; Famoori, F.; Gunaji, R. G.; Govindarajan, S. K. Simulation and Mathematical Modeling of Stimulated Shale Gas Reservoirs. *Ind. Eng. Chem. Res.* **2014,**

53 (51), 19788-19805.

25. Nobakht, M.; Mattar, L.; Moghadam, S.; Anderson, D. M. In *Simplified yet Rigorous Forecasting of Tight/Shale Gas Production in Linear Flow*, SPE Western Regional Meeting, Anaheim, California, USA, May 27-29, 2010; Society of Petroleum Engineers: Anaheim, California, USA, 2010.

26. Sanchez-Rivera, D.; Mohanty, K.; Balhoff, M. Reservoir Simulation and Optimization of Huff-and-Puff Operations in the Bakken Shale. *Fuel.* **2015,** *147*, 82-94.

27. Luo, S.; Wolff, M.; Ciosek, J. M.; Rasdi, M. F.; Neal, L.; Arulampalam, P.; Willis, S. K. In *Probabilistic Reservoir Simulation Workflow for Unconventional Resource Play: Bakken Case Study*, SPE EUROPEC/EAGE Annual Conference and Exhibition, Vienna, Austria, May 23-26, 2011; Society of Petroleum Engineers: Vienna, Austria, 2011.

28. Mayerhofer, M. J.; Lolon, E.; Warpinski, N. R.; Cipolla, C. L.; Walser, D.; Rightmire, C. M. What is Stimulated Reservoir Volume?. *SPE PROD OPER.* 2010, 25 (1), 89-98.

29. Gobran, B.; Abbaszadeh, M.; Brown, S. Determination of Infinite-Acting Period for Well-Test Analysis. *SPE FE.* **1986,** *1* (04), 383-388.

30. Elliot, G. R. In *Well Interference Supports Wide Spacing*, Drilling and Production Practice, New York, New York, Jan 1, 1951; American Petroleum Institute: New York, New York, 1951.

31. Haseman, W. A theory of Well Spacing. *Trans. AIME.* **1930,** *86* (01), 146-155.

32. Miller, C.; Dyes, A. Maximum Reservoir Worth-Proper Well Spacing. *Trans. AIME.* **1959**, 334-340.

33. Roberts, T. Economics of Well Spacing. *SPE.* **1961**, 1-10.

34. Tokunaga, H.; Hise, B. In *A Method to Determine Optimum Well Spacing*, SPE California Regional Meeting, Santa Barbara, California, USA, Nov 17-18, 1966; Society of Petroleum Engineers: Santa Barbara, California, USA, 1966.

35. Zuber, M. D.; Kuuskraa, V. A. Optimizing Well Spacing and Hydraulic-Fracture Design for Economic Recovery of Coalbed Methane. *SPE Formation Evaluation.* **1990,** *5* (01), 98-102.

36. Baker, M. A.; Mazumder, S.; Sharma, H.; Philpot, J. A.; Scott, M. A.; Wittemeier, R. In *Well Design and Well Spacing Optimisation in Unconventional Plays*, SPE Asia Pacific Oil and Gas Conference and Exhibition, Perth, Australia, Oct 22-24, 2012; Society of Petroleum Engineers: Perth, Australia, 2012.

37. Meehan, D. Optimization of Fracture Length and Well Spacing in Heterogeneous Reservoirs. *SPE PROD FACIL.* **1995,** *10* (02), 82-88.

38. Meyer, B. R.; Bazan, L. W.; Jacot, R. H.; Lattibeaudiere, M. G. In *Optimization of Multiple Transverse Hydraulic Fractures in Horizontal Wellbores*, SPE Unconventional Gas Conference, Pittsburgh, Pennsylvania, USA, Feb 23-25, 2010; Society of Petroleum Engineers: Pittsburgh, Pennsylvania, USA, 2010.

39. Hards, E.; Taylor, R.; Wang, Z.; Fyten, G.; Storozhenko, K. In *Optimization of Cardium Fracture Design, Fracture Spacing, and Wellbore Spacing*, SPE Unconventional Resources Conference Canada, Calgary, Alberta, Canada, Nov 5-7, 2013; Society of Petroleum Engineers: Calgary, Alberta, Canada, 2013.

40. Jin, C. In *A Production Optimization Approach to Completion and Fracture Spacing Optimization for Unconventional Shale Oil Exploitation*, Unconventional Resources Technology Conference, Denver, Colorado, USA, Aug 12-14, 2013; Society of Petroleum Engineers: Denver, Colorado, 2013.

41. Eburi, S.; Padmakar, A.; Wilson, K.; Banki, R.; Wardell, I. In *Well Spacing Optimization of Liquid Rich Shale Plays Using Reservoir Simulation*, SPE Annual Technical Conference and Exhibition, Amsterdam, The Netherlands, Oct 27-29, 2014; Society of Petroleum Engineers: Amsterdam, The Netherlands, 2014.

42. Lalehrokh, F.; Bouma, J. In *Well Spacing Optimization in Eagle Ford*, SPE/CSUR Unconventional Resources Conference–Canada, Calgary, Alberta, Canada, Sep 30 - Oct 2, 2014; Society of Petroleum Engineers: Calgary, Alberta, Canada, 2014.

43. Malayalam, A. M. In *Multi-Disciplinary Integration for Lateral Length, Staging and Well Spacing Optimization in Unconventional Reservoirs*, Unconventional Resources Technology Conference, Denver, Colorado, USA, Aug 25-27, 2014; Society of Petroleum Engineers: Denver, Colorado, USA, 2014.

44. Yu, W. In *Optimization of Well Spacing for Bakken Tight Oil Reservoirs*, Unconventional Resources Technology Conference, Denver, Colorado, USA, Aug 25-27, 2014; Society of Petroleum Engineers: Denver, Colorado, USA, 2014.

45. Boulis, A.; Jayakumar, R.; Rai, R. In *A New Approach for Well Spacing Optimisation and Its Application to Various Shale Gas Resources*, International Petroleum Technology Conference, Beijing, China, Mar 26-28, 2013; International Petroleum Technology Conference: Beijing, China, 2013.

46. Sahai, V.; Jackson, G.; Rai, R. R. In *Effect of Non-uniform Fracture Spacing and Fracture Half-length on Well Spacing for Unconventional Gas Reservoirs*, EAGE Annual Conference & Exhibition incorporating SPE Europec, London, UK, Jun 10-13, 2013; Society of Petroleum Engineers: London, UK, 2013.

47. Alghannam, M.; Rahim, Z. In *Optimizing Spacing of Horizontal Multistage Fractured Wells in Gas Reservoirs*, SPE Saudi Arabia Section Technical Symposium and Exhibition, Khobar, Saudi Arabia, Apr 21-24, 2014; Society of Petroleum Engineers: Khobar, Saudi Arabia, 2014.

48. Roussel, N. P.; Sharma, M. M. Optimizing Fracture Spacing and Sequencing in Horizontal-Well Fracturing. *SPE Production & Operations.* **2011,** *26* (02), 173-184.

49. Morrill, J.; Miskimins, J. L. In *Optimization of Hydraulic Fracture Spacing in Unconventional Shales*, SPE Hydraulic Fracturing Technology Conference, The Woodlands, Texas, USA, Feb 6-8, 2012; Society of Petroleum Engineers: The Woodlands, Texas, USA, 2012.

50. Liu, C.; Liu, H.; Zhang, Y.; Deng, D.; Wu, H. Optimal Spacing of Staged Fracturing in Horizontal Shale-gas Well. *J. Petrol. Sci. Eng.* **2015**, *132*, 86-93.

51. Labed, I.; Oyeneyin, B.; Oluyemi, G. In *Hydraulic Fracture Spacing Optimisation for Shale Gas-Condensate Reservoirs Development*, SPE Offshore Europe Conference and Exhibition, Aberdeen, Scotland, UK, Sep 8-11, 2015; Society of Petroleum Engineers: Aberdeen, Scotland, UK, 2015.

52. Khanal, A.; Khoshghadam, M.; Lee, W. In *Effect of Well Spacing On Productivity Of Liquid Rich Shale (LRS) Reservoirs With Multiphase Flow: A Simulation Study*, SPE Liquids-Rich Basins Conference–North America, Midland, Texas, USA, Sept 2-3, 2015; Society of Petroleum Engineers: Midland, Texas, USA, 2015.

53. John, U. M.; Onyekonwu, M. O. In *Non-Linear Programming for Well Spacing Optimization of Oil Reservoirs*, Nigeria Annual International Conference and Exhibition, Tinapa - Calabar, Nigeria, Jul 31 - Aug 7, 2010; Society of Petroleum Engineers: Tinapa - Calabar, Nigeria, 2010.

54. John, M.; Ibukun, S.; Pius, J.; Kayode, O. In *A Stochastic Approach to Well Spacing Optimization of Oil Reservoirs*, Nigeria Annual International Conference and Exhibition, Abuja, Nigeria, Jul 30 - Aug 3, 2011; Society of Petroleum Engineers: Abuja, Nigeria, 2011.

55. Kim, J. G. Advanced Techniques for Oil Reservoir Simulation: Discrete Fracture Model and Parallel Implementation. Ph.D. Thesis, The University of Utah, December 1999.

56. Van Golf-Racht, T. D. *Fundamentals of Fractured Reservoir Engineering*; Elsevier Scientific Publishing Company: Amsterdam, The Netherlands, 1982.

57. Hyne, N. J. *Nontechnical Guide to Petroleum Geology, Exploration, Drilling, and Production*. PennWell Corporation: Tulsa, 2012.

58. Bjorlykke, K., *Sedimentology and Petroleum Geology*. Springer-Verlag: New York, 1989.

59. Warpinski, N.; Branagan, P.; Peterson, R.; Wolhart, S.; Uhl, J. In *Mapping Hydraulic Fracture Growth and Geometry Using Microseismic Events Detected by a Wireline Retrievable Accelerometer Array*, SPE Gas Technology Symposium, Calgary, Alberta, Canada, Mar 15-18, 1998; Society of Petroleum Engineers: Calgary, Alberta,

Canada, 1998.

60. Cinco-Ley, H.; Samaniego, V.; Dominguez, A. Transient pressure behavior for a well with a finite-conductivity vertical fracture. *SPEJ.* **1978,** *18* (04), 253-264.

61. Gidley, J. A Method for Correcting Dimensionless Fracture Conductivity for Non-Darcy Flow Effects. *SPE Prod. Eng.* **1991,** *6* (04), 391-394.

62. Panja, P.; Conner, T.; Deo, M. Grid Sensitivity Studies in Hydraulically Fractured Low Permeability Reservoirs. *J. Petrol. Sci. Eng.* **2013,** *112*, 78-87.

63. Lee, S.; Durlofsky, L.; Lough, M.; Chen, W. In *Finite Difference Simulation of Geologically Complex Reservoirs with Tensor Permeabilities*, SPE Reservoir Simulation Symposium, Dallas, Texas, USA, Jun 8-11, 1997; Society of Petroleum Engineers: Dallas, Texas, USA, 1997.

64. Oda, M. Permeability Tensor for Discontinuous Rock Masses. *Geotechnique.* **1985,** *35* (4), 483-495.

65. Warren, J.; Root, P. J. The Behavior of Naturally Fractured Reservoirs. *SPEJ.* **1963,** *3* (03), 245-255.

66. Kazemi, H.; Merrill Jr, L.; Porterfield, K.; Zeman, P. Numerical Simulation of Water-Oil Flow in Naturally Fractured Reservoirs. *SPEJ.* **1976,** *16* (06), 317-326.

67. Gilman, J. R.; Kazemi, H. Improvements in Simulation of Naturally Fractured Reservoirs. *SPEJ.* **1983,** *23* (04), 695-707.

68. Bourbiaux, B.; Granet, S.; Landereau, P.; Noetinger, B.; Sarda, S.; Sabathier, J. In *Scaling up Matrix-Fracture Transfers in Dual-Porosity Models: Theory and Application*, SPE Annual Technical Conference and Exhibition, Houston, Texas, USA, Oct 3-6, 1999; Society of Petroleum Engineers: Houston, Texas, USA, 1999.

69. Pirker, B.; Heinemann, Z. E. In *Method to Preliminary Estimation of the Reserves and Production Forecast for Dual Porosity Fractured Reservoirs*, Europec/EAGE Conference and Exhibition, Rome, Italy, Jun 9-12, 2008; Society of Petroleum Engineers: Rome, Italy, 2008.

70. Sarma, P.; Aziz, K. New Transfer Functions for Simulation of Naturally Fractured Reservoirs with Dual Porosity Models. *SPEJ.* **2006,** *11* (3), 328-340.

71. Sonier, F.; Eymard, R. In *A new Simulator for Naturally Fractured Reservoirs*, SPE Symposium on Reservoir Simulation, San Antonio, Texas, USA, Feb 1-4, 1987; Society of Petroleum Engineers: San Antonio, Texas, USA, 1987.

72. Gilman, J. R.; Kazemi, H. Improved Calculations for Viscous and Gravity Displacement in Matrix Blocks in Dual-Porosity Simulators. *JPT.* **1988,** *40* (01), 60-70.

73. Thomas, L. K.; Dixon, T. N.; Pierson, R. G. Fractured Reservoir Simulation. *SPEJ.* **1983,** *23* (01), 42-54.

74. Dean, R. H.; Lo, L. L. Simulations of Naturally Fractured Reservoirs. *SPE Res. Eng.* **1988,** *3* (02), 638-648.

75. Rossen, R.; Shen, E. Simulation of Gas/Oil Drainage and Water/Oil Imbibition in Naturally Fractured Reservoirs. *SPE Res. Eng.* **1989,** *4* (04), 464-470.

76. Dutra Jr, T.; Aziz, K. A New Double-Porosity Reservoir Model for Oil/Water Flow Problems. *SPE Res. Eng.* **1992,** *7* (04), 419-425.

77. Ladron De Guevara, J. E. T.; Galindo-Nava, A. In *Gravity Drainage and Oil Reinfiltration Modeling in Naturally Fractured Reservoir Simulation*, International Oil Conference and Exhibition in Mexico, Veracruz, Mexico, Jun 27-30, 2007; Society of Petroleum Engineers: Veracruz, Mexico, 2007.

78. Saidi, A. In *Simulation of Naturally Fractured Reservoirs*, SPE Reservoir Simulation Symposium, San Francisco, California, USA, Nov 15-18, 1983; Society of Petroleum Engineers: San Francisco, California, USA, 1983.

79. Fung, L. S. Simulation of Block-to-Block Processes in Naturally Fractured Reservoirs. *SPE Res. Eng.* **1991,** *6* (04), 477-484.

80. Rubin, B. In *Simulating Gravity Drainage and Reinfiltration with a Subdomain-Dual-Permeability Hybrid Fracture Model*, SPE Reservoir Simulation Symposium, Houston, Texas, USA, Feb 26-28, 2007; Society of Petroleum Engineers: Houston, Texas, USA, 2007.

81. Litvak, B.; Satter, A.; Etebar, S. In *An Analysis of Naturally Fractured Reservoir Performance Using a Novel Fractured Reservoir Simulator*, International Meeting on Petroleum Engineering, Tianjin, China, Nov 1-4, 1988; Society of Petroleum Engineers: Tianjin, China, 1988.

82. Wilson, C. R.; Witherspoon, P. A. Steady State Flow in Rigid Networks of Fractures. *Water Resour. Res.* **1974,** *10* (2), 328-335.

83. Noorishad, J.; Mehran, M. An Upstream Finite Element Method for Solution of Transient Transport Equation in Fractured Porous Media. *Water Resources Research.* **1982,** *18* (3), 588-596.

84. Baca, R.; Arnett, R.; Langford, D. Modelling Fluid Flow in Fractured-Porous Rock Masses by Finite-Element Techniques. *Int. J. Numer. Meth. Fl.* **1984,** *4* (4), 337-348.

85. Kim, J. G.; Deo, M. D. In *Comparison of the Performance of a Discrete Fracture Multiphase Model with Those Using Conventional Methods*, SPE symposium on reservoir simulation, Houston, Texas, USA, Feb 14-17, 1999; Society of Petroleum Engineers: Houston, Texas, USA, 1999; pp 359-371.

86. Kim, J. G.; Deo, M. D. Finite Element, Discrete-Fracture Model for Multiphase Flow in Porous Media. *AIChE.* **2000,** *46* (6), 1120-1130.

87. Yang, Y. K. Finite-Element, Multiphase Flow Simulation. Ph.D. Thesis, The University of Utah, August 2003.

88. Karimi-Fard, M.; Firoozabadi, A. In *Numerical Simulation of Water Injection in 2d Fractured Media Using Discrete-Fracture Model*, SPE annual technical conference and exhibition, New Orleans, Louisiana, Sept 30 - Oct 3, 2001; Society of Petroleum Engineers: New Orleans, Louisiana, 2001.

89. Fu, Y. Multiphase Control Volume Finite Element Simulations of Fractured Reservoirs. Ph.D. Thesis, The University of Utah, May 2007.

90. Monteagudo, J.; Firoozabadi, A. Control-Volume Method for Numerical Simulation of Two-Phase Immiscible Flow in Two-and Three-Dimensional Discrete-Fractured Media. *Water Resour. Res.* **2004,** *40* (7).

91. Monteagudo, J. E.; Firoozabadi, A. Control-Volume Model for Simulation of Water Injection in Fractured Media: Incorporating Matrix Heterogeneity and Reservoir Wettability Effects. *SPEJ.* **2007,** *12* (03), 355-366.

92. Huang, C.-K. Development of a General Thermal Oil Reservoir Simulator under a Modularized Framework. Ph.D. Thesis, The University of Utah, January 2009.

93. Gu, Z. A Geochemical Compositional Simulator. Ph.D. Thesis, The University of Utah, May 2010.

94. Aavatsmark, I. In *Multipoint Flux Approximation Methods for Quadrilateral Grids*, 9th International forum on reservoir simulation, Abu Dhabi, Dec 9-10, 2007.

95. Abou-Kassem, J. H.; Farouq-Ali, S.; Islam, M. R. *Petroleum Reservoir Simulations*; Gulf PublishingCompany: Houston, Texas, 2006.

96. ECLIPSE *Technical Description*; Schlumberger: 2006.

97. Kukreti, A. R.; Rajapaksa, Y. A Numerical Model for Simulating Two-Phase Flow through Porous Media. *Appl. Math. Model.* **1989**, *13*, 268–281.

98. Bergamaschi, L.; Mantica, S.; Manzini, G. A Mixed Finite Element--Finite Volume Formulation of the Black-Oil Model. *SIAM J. Sci. Comput.* **1998,** *20* (3), 970-997.

99. Cordazzo, J.; Maliska, C.; da Silva, A. F.; Hurtado, F. S. In *An Element Based Conservative Scheme Using Unstructured Grids for Reservoir Simulation*, 18th World Petroleum Congress, Johannesburg, South Africa, Sept 25-29, 2005; World Petroleum Congress: Johannesburg, South Africa, 2005.

101. Velasco Hurtado, F. S.; Maliska, C. R.; Carvalho da Silva, A. F.; Cordazzo, J. In *A*

Quadrilateral Element-Based Finite-Volume Formulation for the Simulation of Complex Reservoirs, Latin American & Caribbean Petroleum Engineering Conference, Buenos Aires, Argentina, Apr 15-18, 2007; Society of Petroleum Engineers: Buenos Aires, Argentina, 2007.

102. Chappelear, J. E.; Williamson, A. S. Representing Wells in Numerical Reservoir Simulation: Part 2-Implementation. *SPJ.* **1981,** *21* (03), 339-344.

103. Peaceman, D. W. Interpretation of Well-Block Pressures in Numerical Reservoir Simulation with Nonsquare Grid Blocks and Anisotropic Permeability. *SPEJ.* **1983,** *23* (03), 531-543.

104. Bear, J. *Dynamics of Fluids in Porous Media*; Dover: New York, 1988.